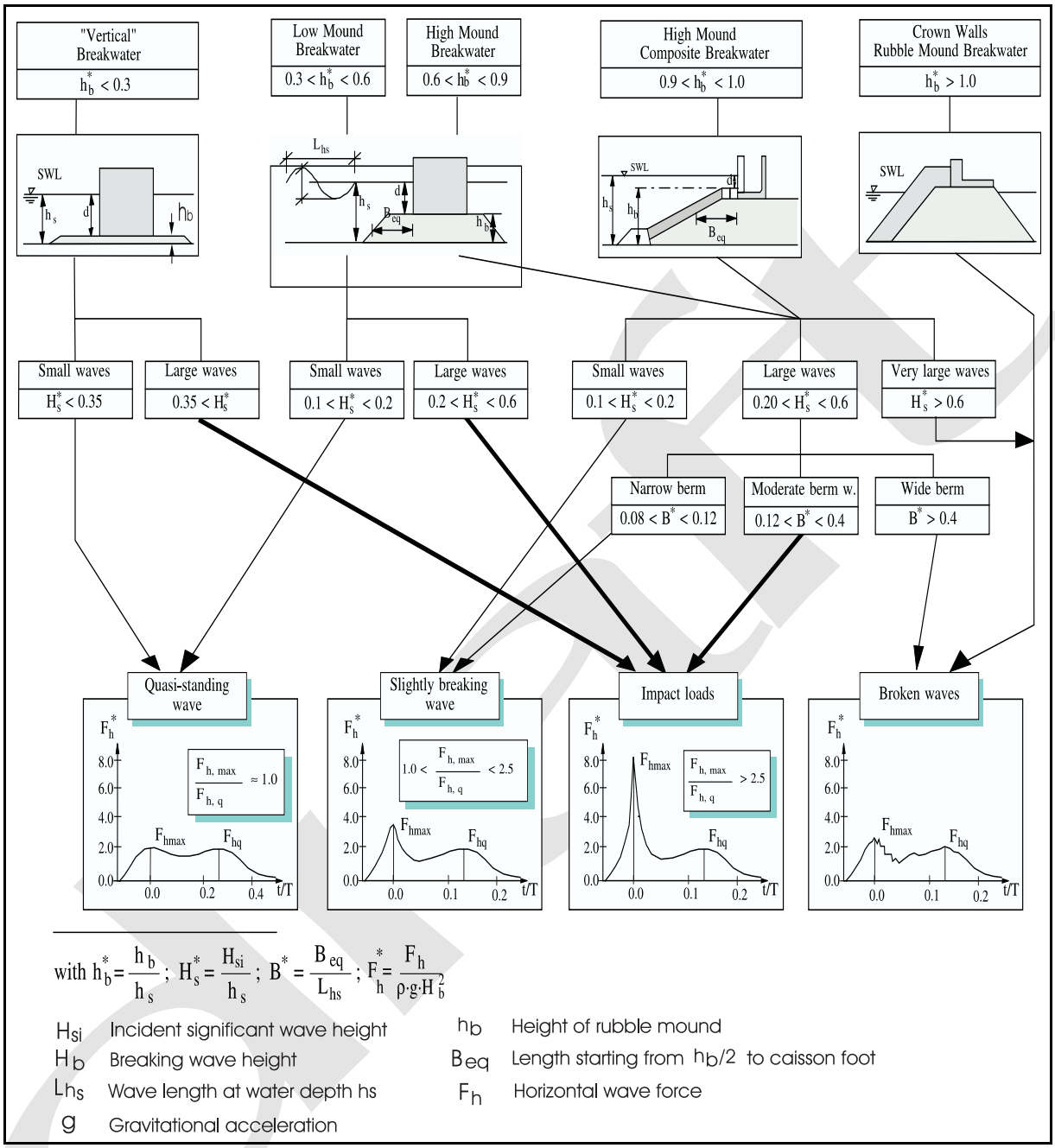

Figure VI-5-58. Identification of types of total horizontal wave loadings on vertical wall structure exposed to head-on long-crested irregular waves (Kortenhaus and Oumeraci 1998). Not valid if breaker zone is present in front of the structure

(b) Notice in the right-hand sketch of Figure VI-5-59 the resulting total hydrodynamic load when the wave trough is at the vertical wall is less than the hydrostatic loading if waves were not present and the water was at rest. For bulkheads and seawalls this may be a critical design loading because saturated backfill soils could cause the wall to fail in the seaward direction (see Figures VI-2-63 and VI-2-71). Therefore, water level is a crucial design parameter for calculating forces and moments on vertical walls.

(c) Wave overtopping of vertical walls provides a reduction in the total force and moment because the pressure distribution is truncated as shown schematically in Figure VI-5-60. Engineers should consider the

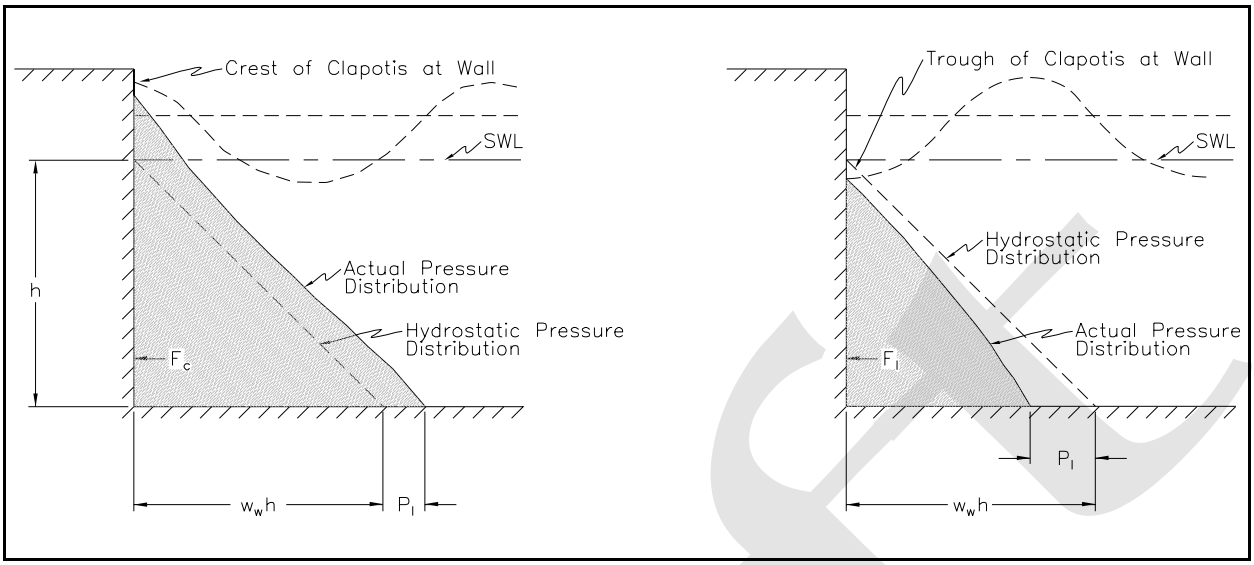

Figure VI-5-59. Pressure distributions for nonbreaking waves

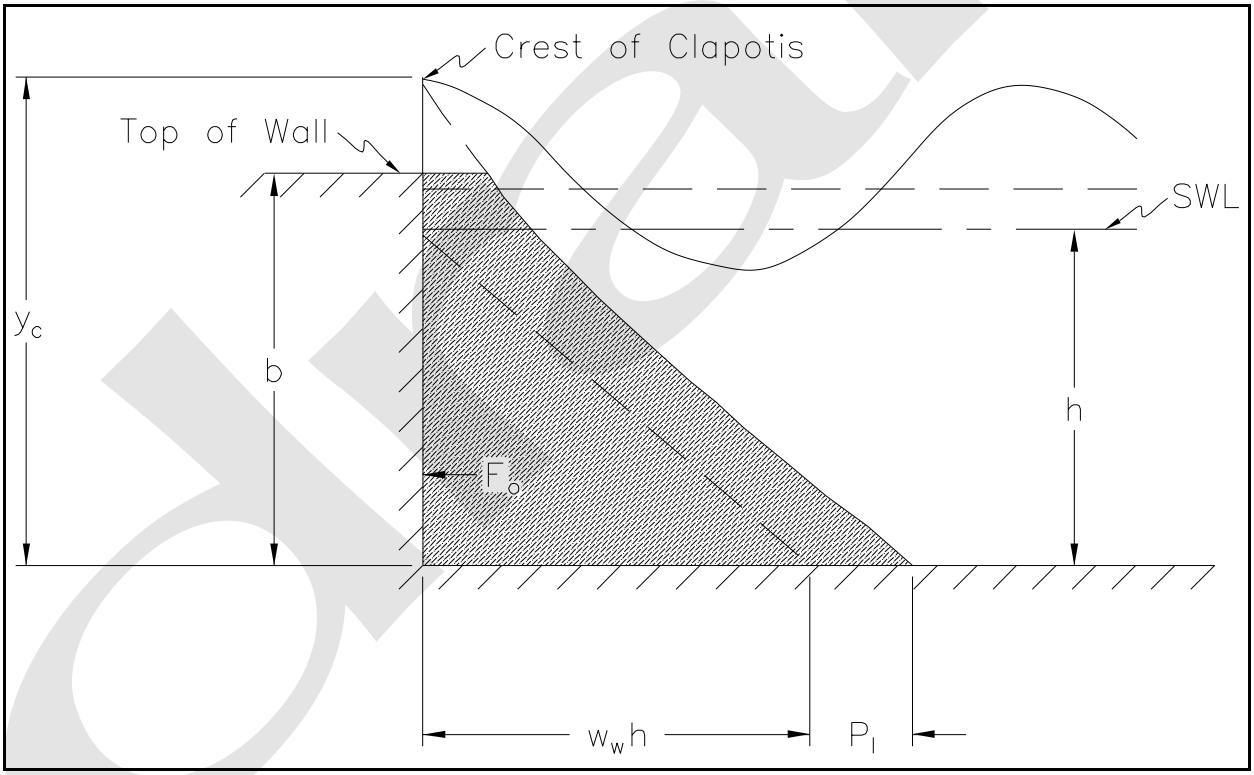

Figure VI-5-60. Pressure distributions on overtopped vertical wall

effect overtopping might have on land-based vertical structures by creating seaward pressure on the wall caused by saturated backfill or ponding water.

(d) This section provides formulae for estimating pressure distributions and corresponding forces and overturning moments on vertical walls due to nonbreaking and breaking waves. Most of the methodology is based on the method presented by Goda (1974) and extended by others to cover a variety of conditions. These formulae provide a unified design approach to estimating design loads on vertical walls and caissons.

(e) Important Note: All of the methods in this section calculate the pressure distribution and resulting forces and moments for only the wave portion of the hydrodynamic loading. The hydrostatic pressure distribution from the swl to the bottom is excluded (see Figure VI-5-59). For a caisson structure, the swl hydrostatic forces would exactly cancel; however, it will be necessary to include the effect of the swl hydrodynamic pressure for vertical walls tied into the shoreline or an embankment.

(f) The formulae given in the following tables are exclusively based on small-scale model tests. They are presented as follows:

Formula	Waves	Structure	Table
Sainflou formula	Standing	Impermeable vertical wall	VI-5-52
Goda formula	2-D oblique	Impermeable vertical wall	VI-5-53
Goda formula, modified by Takahashi, Tanimoto, and Shimosako 1994a	Provoked breaking	Impermeable vertical wall	VI-5-54
Goda formula forces and moments	Provoked breaking	Impermeable vertical wall	VI-5-55
Goda formula modifed by Tanimoto and Kimura 1985	2-D head-on	Impermeable inclined wall	VI-5-56
Goda formula modified by Takahashi and Hosoyamada 1994	2-D head-on	Impermeable sloping top	VI-5-57
Goda formula modified by Takahashi, Tanimoto, and Shimosako 1990	2-D head-on	Horizontal composite structure	VI-5-58
Goda formula modifed by Takahashi, Tanimoto, and Shimosako 1994b	3-D head-on	Vertical slit wall	VI-5-59

(g) Wave pressure distributions for breaking waves are estimated using Table VI-5-54, and the corresponding forces and moments are calculated from Table VI-5-55. Not included in this manual is the older breaking wave forces method of Minikin as detailed in the *Shore Protection Manual* (1984). As noted in the Shore Protection Manual the Minikin method can result in very high estimates of wave force, "as much as 15 to 18 times those calculated for nonbreaking waves." These estimates are too conservative in most cases and could result in costly structures.

(h) On the other hand, there may be rare circumstances where waves could break in just the right manner to create very high impulsive loads of short duration, and these cases may not be covered by the range of experiment parameters used to develop the guidance given in Table VI-5-54. In addition, scaled laboratory models do not correctly reproduce the force loading where pockets of air are trapped between the wave and wall as shown in Figure VI-5-57. For these reasons, it may be advisable to design vertical-front structures serving critical functions according to Minikin's method given in *Shore Protection Manual* (1984).

Table VI-5-52
The Sainflou Formula for Head-on, Fully Reflected, Standing Regular Waves (Sainflou 1928)

.

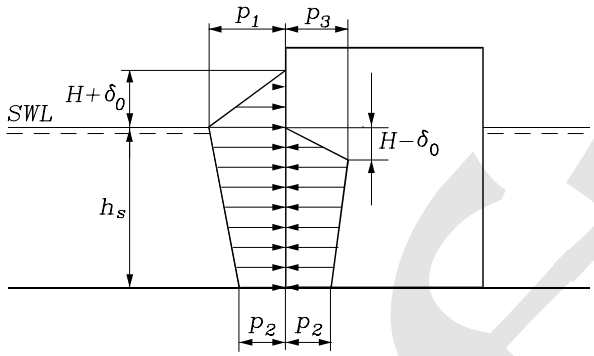

$$p_1 = (p_2 + \rho_w g h_s)\frac{H + \delta_o}{h_s + H + \delta_o} \qquad \text{(VI−5−143)}$$

$$p_2 = \frac{\rho_w g H}{\cosh(2\pi h_s / L)} \qquad \text{(VI−5−144)}$$

$$p_3 = \rho_w g (H - \delta_o) \qquad \text{(VI−5−145)}$$

$$\delta_o = \frac{\pi H^2}{L} \coth \frac{2\pi h_s}{L} \qquad \text{(VI−5−146)}$$

where H Wave height. In case of irregular waves, H should be taken as a characteristic wave height. In Japan $H_{1/3}$ is used, while in other countries $H_{1/10}$ might be used.

p_1 Wave pressure at the still water level, corresponding to wave crest

p_2 Wave pressure at the base of the vertical wall

p_3 Wave pressure at the still water level, corresponding to wave trough

δ_o Vertical shift in the wave crest and wave trough at the wall

ρ_w Water density

h_s Water depth at the foot of the structure

L Local wave length.

Remarks. The Sainflou formula for conditions under wave crest and wave trough were derived theoretically for the case of regular waves and a vertical wall. The formula cannot be applied in cases where wave breaking and/or overtopping takes place.

Table VI-5-53
Goda Formula for Irregular Waves (Goda 1974; Tanimoto et al. 1976)

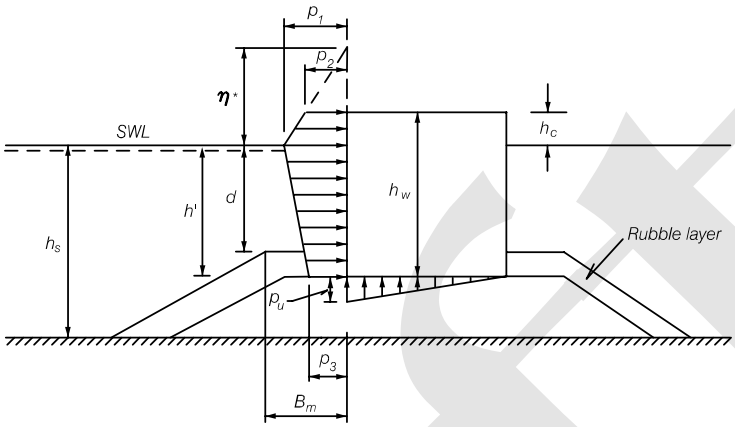

$$\eta^* = 0.75(1 + cos\beta)\,\lambda_1 H_{design} \qquad \text{(VI-5-147)}$$

$$p_1 = 0.5(1 + cos\beta)(\lambda_1\alpha_1 + \lambda_2\alpha_* cos^2\beta)\,\rho_w\, g\, H_{design} \qquad \text{(VI-5-148)}$$

$$p_2 = \begin{cases} \left(1 - \frac{h_c}{\eta^*}\right) p_1 & \text{for } \eta^* > h_c \\ 0 & \text{for } \eta^* \le h_c \end{cases} \qquad \text{(VI-5-149)}$$

$$p_3 = \alpha_3\, p_1 \qquad \text{(VI-5-150)}$$

$$p_u = 0.5(1 + cos\beta)\lambda_3\alpha_1\alpha_3\rho_w g\, H_{design} \qquad \text{(VI-5-151)}$$

where

β Angle of incidence of waves (angle between wave crest and front of structure)

H_{design} Design wave height defined as the highest wave in the design sea state at a location just in front of the breakwater. If seaward of a surf zone Goda (1985) recommends for practical design a value of 1.8 H_s to be used corresponding to the 0.15% exceedence value for Rayleigh distributed wave heights. This corresponds to $H_{1/250}$ (mean of the heights of the waves included in 1/250 of the total number of waves, counted in descending order of height from the highest wave). Goda's recommendation includes a safety factor in terms of positive bias as discussed in Table VI-5-55. If within the surf zone, H_{design} is taken as the highest of the random breaking waves at a distance $5H_s$ seaward of the structure.

$$\alpha_* = \alpha_2$$

$$\alpha_1 = 0.6 + 0.5\left[\frac{4\pi h_s/L}{sinh\,(4\pi h_s/L)}\right]^2$$

$$\alpha_2 = \text{the smallest of } \frac{h_b - d}{3h_b}\left(\frac{H_{design}}{d}\right)^2 \text{ and } \frac{2d}{H_{design}}$$

$$\alpha_3 = 1 - \frac{h_w - h_c}{h_s}\left[1 - \frac{1}{cosh\,(2\pi h_s/L)}\right]$$

L Wavelength at water depth h_b corresponding to that of the significant wave $T_s \simeq 1.1T_m$, where T_m is the average period.

h_b Water depth at a distance of $5H_s$ seaward of the breakwater front wall.

λ_1, λ_2 and λ_3 are modification factors depending on the structure type. For conventional vertical wall structures, $\lambda_1 = \lambda_2 = \lambda_3 = 1$. Values for other structure types are given in related tables.

Table VI-5-53. Continued

Uncertainty and bias of formulae: See Table VI-5-55.

Tested ranges:	water depth (cm)	wave height (cm)	wave period (s)	mound height (cm)
	35	7.1-31.2	2	0 & 15
	45	6.7-41.6	1.7	0 & 25
	45	7.6-32.8	1.3	0 & 25
	45	9.2-22.9	1	0 & 25

The formulae have been calibrated with the cases of 21 slidings and 13 nonslidings of the upright sections of the prototype breakwaters in Japan.

Table VI-5-54
Goda Formula Modified to Include Impulsive Forces from Head-on Breaking Waves (Takahashi, Tanimoto, and Shimosako 1994a)

The modification of Goda's formula concerns the formula for the pressure p_1 at the still water level (SWL). The coefficient α_* is modified as

$$\alpha_* = \text{largest of } \alpha_2 \text{ and } \alpha_I$$

$$\alpha_2 = \text{the smallest of } \frac{h_b - d}{3\,h_b}\left(\frac{H_{design}}{d}\right)^2 \text{ and } \frac{2d}{H_{design}}$$

$$\alpha_I = \alpha_{I0} \cdot \alpha_{I1}$$

$$\alpha_{I0} = \begin{cases} H_{design}/d & \text{for} \quad H_{design}/d \le 2 \\ 2.0 & \text{for} \quad H_{design}/d > 2 \end{cases}$$

$$\alpha_{I1} = \begin{cases} \frac{\cosh \delta_2}{\cosh \delta_1} & \delta_2 \le 0 \\ \frac{1}{\cosh \delta_1 \cdot (\cosh \delta_2)^{\frac{1}{2}}} & \delta_2 > 0 \end{cases}$$

$$\delta_1 = \begin{cases} 20 \cdot \delta_{11} & \text{for} \quad \delta_{11} \le 0 \\ 15 \cdot \delta_{11} & \text{for} \quad \delta_{11} > 0 \end{cases}$$

$$\delta_{11} = 0.93\left(\frac{B_m}{L} - 0.12\right) + 0.36\left(\frac{h_s - d}{h_s} - 0.6\right)$$

$$\delta_2 = \begin{cases} 4.9 \cdot \delta_{22} & \text{for} \quad \delta_{2\,2} \le 0 \\ 3 \cdot \delta_{22} & \text{for} \quad \delta_{22} > 0 \end{cases}$$

$$\delta_{22} = -0.36\left(\frac{B_m}{L} - 0.12\right) + 0.93\left(\frac{h_s - d}{h_s} - 0.6\right)$$

where H_{design}, L, d, h_s, h_b, B_m are given in the figure and text of Table VI-5-53.

Range of tested parameters:	Regular waves	
	bottom slope 0.01	h_s = 42 cm and 54 cm
	d = 7 – 39 cm	B_m = 2.5 – 200 cm
	H = 17.2 – 37.8 cm	T - 1.8 – 3 sec.

Table VI-5-55
Resulting Wave Induced Forces and Moments, and Related Uncertainties and Bias When Calculated From Wave Load Equations by Goda and Takahashi

Per running meter of the breakwater the wave induced horizontal force, F_H, the uplift force, F_U, and the reduced weight of the vertical structure due to buoyancy, F_G, can be calculated from equations by Goda and Takahashi as follows:

$$F_H = U_{F_H}\left[\frac{1}{2}(p_1+p_2)h_c+\frac{1}{2}(p_1+p_3)h'\right] \quad \text{(VI-5-152)}$$

$$F_U = U_{F_U}\cdot\frac{1}{2}p_u\cdot B \quad \text{(VI-5-153)}$$

$$F_G = \rho_c\cdot g\,B\cdot h_w-\rho_w\cdot g\,B\cdot h' \quad \text{(VI-5-154)}$$

where ρ_c Mass density of the structure

ρ_w Mass density of the water

U_{F_H} Stochastic variable signifying the bias and the uncertainty related to the horizontal force

U_{F_U} Stochastic variable signifying the bias and the uncertainty related to the uplift force

h' Submerged height of the wall from the toe to the still water level.

B Vertical structure width

The corresponding moments at the heel of the caisson breakwater are:

$$M_H = U_{M_H}\left[\frac{1}{6}(2p_1+p_3)h'^2+\right.$$
$$\left.+\frac{1}{2}(p_1+p_2)h'h_c+\frac{1}{6}(p_1+2p_2)h_c^2\right] \quad \text{(VI-5-155)}$$

$$M_U = U_{M_U}\cdot\frac{1}{3}p_u\cdot B^2 \quad \text{(VI-5-156)}$$

$$M_G = \frac{1}{2}B^2 g\left(\rho_c h_w-\rho_w h'\right) \quad \text{(VI-5-157)}$$

where U_{M_H} Stochastic variable signifying the bias and the uncertainty of the horizontal moment

U_{M_U} Stochastic variable signifying the bias and the uncertainty of the uplift moment.

Uncertainty and bias of the Goda formulae in Table VI-5-53. Based on reanalysis by Juhl and van der Meer (1992), Bruining (1994), and van der Meer, Juhl, and van Driel (1994) of various model tests performed at Danish Hydraulic Institute and Delft Hydraulics. The mean values and standard deviations of the stochastic variables U are given as

Uncertainty and bias of horizontal wave induced force, uplift force, horizontal moment and uplift moment (vertical composite type)

Stochastic variable	Mean value	no model tests		model test performed	
		Stand. dev.		Stand. dev.	
X_i	μ_{X_i}	σ_{X_i}	$\frac{\sigma_{X_i}}{\mu_{X_i}}$%	σ_{X_i}	$\frac{\sigma_{X_i}}{\mu_{X_i}}$%
U_{F_H}	0.90	0.25	0.22	0.05	0.055
U_{F_U}	0.77	0.25	0.32	0.05	0.065
U_{M_H}	0.81	0.40	0.49	0.10	0.12
U_{M_U}	0.72	0.37	0.51	0.10	0.14

Table VI-5-56
Wave Loads on Impermeable Inclined Walls (Tanimoto and Kimura 1985)

Tanimoto and Kimura (1985) performed model tests and demonstrated that the Goda formula can be applied by projection of the Goda wave pressures calculated for a vertical wall with the same height (crest level) as illustrated in the figure.

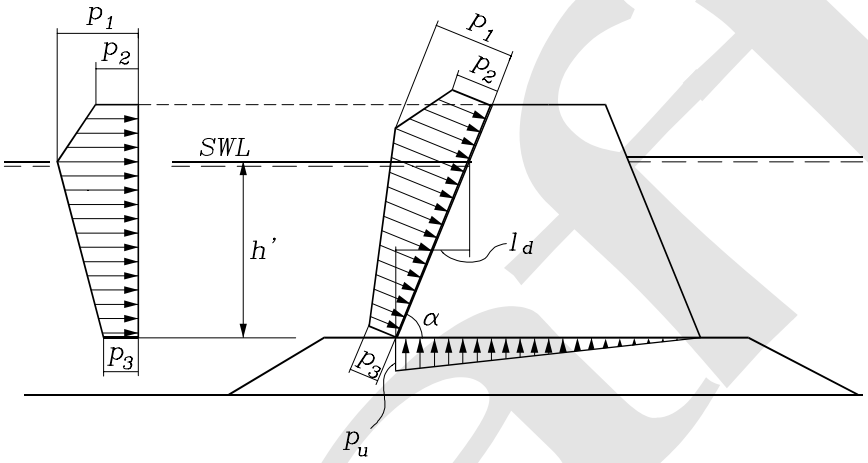

The wave induced uplift pressure on the base plate is reduced compared to the vertical face case. Consequently λ_3 for the calculation of p_u in the Goda formula is modified as

$$\lambda_3 = exp\left[-2.26(7.2\,\ell_d\,/L)^3\right] \qquad (\text{VI}-5-158)$$

where $\ell_d = h' \cot\alpha$ and L is the wavelength.

Eq VI-5-158 is valid for $\alpha \geq 70^\circ$ and $\ell_d < 0.1L$.

Table VI-5-57
Wave Loads on Sloping Top Structures (Takahashi and Hosoyamada 1994)

Tested cross sections

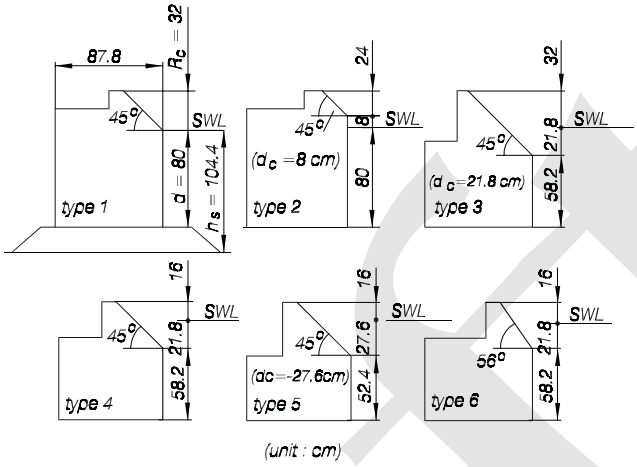

Pressure distribution

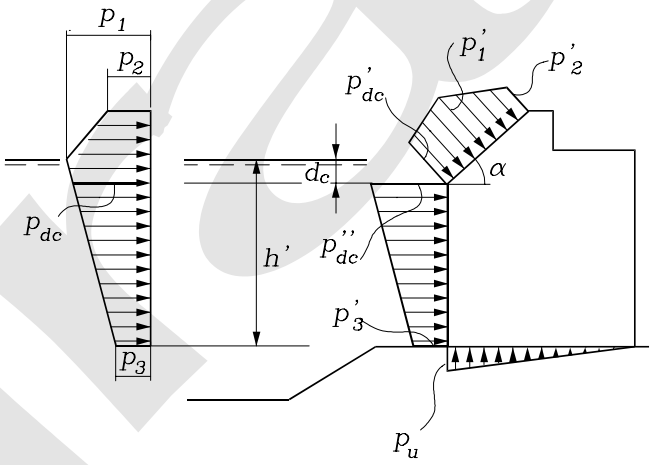

$$p'_1 = \lambda_{SL}\, p_1 \sin\alpha\ ,\ p'_2 = \lambda_{SL}\, p_2 \sin\alpha\ ,\ p'_{d_c} = \lambda_{SL}\, p_{dc} \sin\alpha$$

$$p''_{d_c} = \lambda_V\, p_{d_c}\ \ ,\ \ p'_3 = \lambda_V\, p_3 \qquad \text{(VI-5-159)}$$

where

$\lambda_{SL} = \frac{1}{\sin^2\alpha}\ min[1.0\ ,\ max(\sin^2\alpha\ ,\ 1 + 0.46\cos^2\alpha - 23\cos^2\alpha H/L)]$

$\lambda_V = min[1.0\ ,\ max(1.1.\ ,\ 1.1 + 11 d_c/L) - 5.0 H/L]$

$p_1,\ p_2,\ p_3,\ p_{dc}$ & p_u are calculated from the Goda formula (Table VI-5-55)

Table VI-5-58
Wave Loads on Vertical Walls Protected by a Rubble-Mound Structure (Takahashi, Tanimoto, and Shimosako 1990)

.

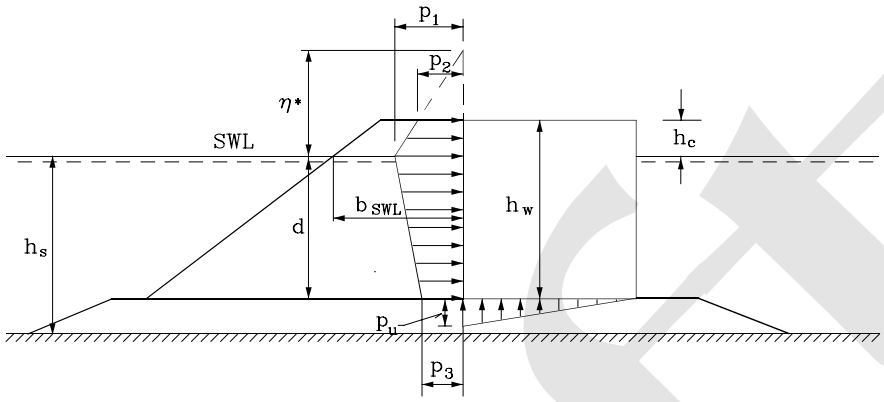

λ_1, λ_2 and λ_3 in the Goda formula are modified as:

$$\lambda_1 = \lambda_3 = \begin{cases} 1.0 & H_{design}/h_s < 0.3 \\ 1.2 - 0.67\,(H_{design}/h_s) & 0.3 \le H_{design}/h_s \le 0.6 \\ 0.8 & H_{design}/h_s > 0.6 \end{cases} \qquad \text{(VI}-5-160\text{)}$$

$$\lambda_2 = 0$$

Validity range: These values presume that the rubble consists of blocks of the complex types like Tetrapods and Dolosse. Also, the width of the block section at the top of the vertical wall should be no less than twice the height of a block. The front slope is approximately 1 : 1.5. The model tests cover the parameter intervals: $h_s/L_{1/3} = 0.07 - 0.11$ and $b_{SWL}/L_{1/3} = 0.046 - 0.068$.

Uncertainty and bias: From the test results the mean value, μ_{λ_1}, and the variational coefficient, $\frac{\sigma_{\lambda_1}}{\mu_{\lambda_1}}$, of λ_1 are estimated to be approximately

$$\mu_{\lambda_1} = \begin{cases} 0.90 & H_{design}/h_s < 0.4 \\ 0.90 - (H_{design}/h_s - 0.4) & 0.4 \le H_{design}/h_s \le 0.7 \\ 0.60 & 0.7 < H_{design}/h_s < 0.8 \end{cases} \qquad \text{(VI}-5-161\text{)}$$

and

$$\frac{\sigma_{\lambda_1}}{\mu_{\lambda_1}} = 5\% - 10\%$$

Table VI-5-59
Wave Pressures from Regular Head-on Waves on Caissons with Vertical Slit Front Face and Open Wave Chamber (Tanimoto, Takahashi, and Kitatani 1981; Takahashi, Shimosako, and Sakaki 1991)

Cross sections

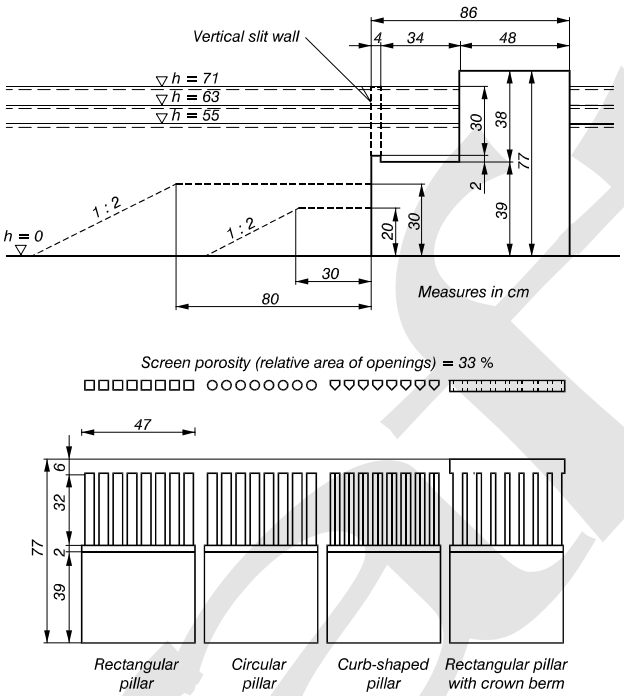

Tested wave range: Regular head-on waves
Incident wave height: 10-30 cm
Wave period: 1.5, 2.0, 2.5 s

Considered wave crest faces

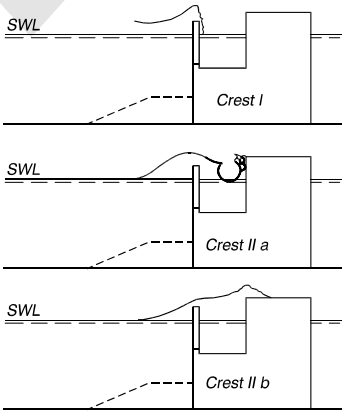

Table VI-5-59. Continued

Pressure distribution

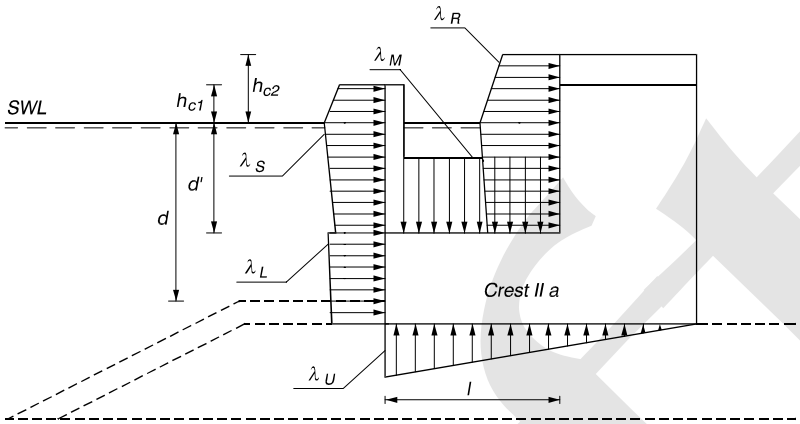

Pressure calculation: Use the Goda formulae with modified λ_1, λ_2 and λ_3 as given in the following table. For example, the wave pressure on the slit wall in the case of Crest-I is calculated by the Goda formulae with λ_1 and λ_2 replaced by λ_{S1} and λ_{S2}, respectively.

Modification factors for vertical slit wall caisson (From Takahashi, Tanimoto, and Shimasako 1994b).

		Crest-I	Crest-IIa	Crest-IIb
Slit wall	λ_{S1}	0.85	0.7	0.3
	λ_{S2}	0.4 ($\alpha^* \le 0.75$) $0.3/\alpha^*$ ($\alpha^* > 0.75$)	0	0
Impermeable part of front wall	λ_{L1}	1	0.75	0.65
	λ_{L2}	0.4 ($\alpha^* \le 0.5$) $0.2/\alpha^*$ $\alpha^* > 0.5$)	0	0
Wave chamber rear wall	λ_{R1}	0	$20l/3L'$ $l/L' \le 0.15$) 1.0 ($1/L' > 0.15$)	1.4 ($H/h \le 0.1$) 1.6 - $2H/h$ ($0.1 < H/h < 0.3$) 1.0 ($H/h \ge 0.3$)
	λ_{R2}	0	0.56 ($\alpha^* \le 25/28$) $0.5/\alpha^*$ ($\alpha^* > 25/28$)	0
Wave Chamber bottom slab	λ_{M1}	0	$20l/3L'$ ($l/L' \le 0.15$) 1.0 ($l/L' > 0.15$)	1.4 ($H/h \le 0.1$) 1.6 - $2H/h$ ($0.1 < H/h < 0.3$) 1.0 ($H/h \ge 0.3$)
	λ_{M2}	0	0	0
Uplift force	λ_{U3}	1	0.75	0.65

In the calculation of α^* for the rear wall, α_1 should be replaced by α_1' which is obtained with the parameters d', L' and B_M' instead of d, L and B_M respectively, where d' is the depth in the wave chamber, L' is the wavelength at water depth d, $B_M' = l - (d - d')$, and l is the width of the wave chamber including the thickness of the perforated vertical wall.

(2) Vertical wave barriers.

(a) A vertical wave barrier is a vertical partition that does not extend all the way to the bottom as illustrated by the definition sketch in Figure VI-5-61. Wave barriers reduce the transmitted wave height while allowing circulation to pass beneath the barrier. A useful application for vertical wave barriers is small harbor protection.

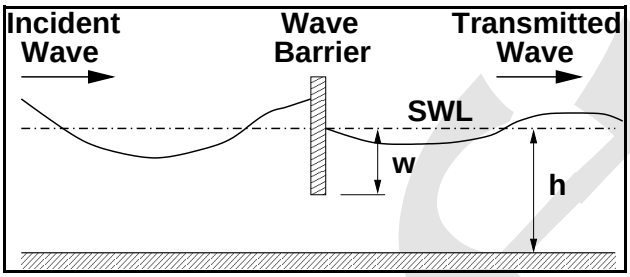

Figure VI-5-61. Wave barrier definition sketch

(b) Kriebel, Sollitt, and Gerken (1998) presented small- and large-scale laboratory measurements of forces on vertical wave barriers and found that existing methods for estimating wave forces on wave barriers overpredicted measured forces by about a factor of 2. They also presented an eigenvalue expansion method for calculating theoretical wave forces, and the predicted forces matched the experiment measurements within 10-20 percent. Both regular and irregular wave experiments were used in the analysis.

(c) Estimation of wave forces using the eigenvalue expansion method involves solving matrix equations for unknown coefficients under the physical constraints of no flow through the barrier and matching dynamic pressure in the gap beneath the barrier. However, this method must be programmed on a computer to obtain force estimates.

(d) An empirical equation for estimating forces on vertical wave barriers was developed for this manual based on the large-scale laboratory irregular wave measurements presented in Kriebel et al. (1998). Their experiments used solid vertical plates having penetration values of $w/h = 0.4$, 0.5, 0.6, and 0.7 placed in a 3-m water depth. Time series of total force on the plate were recorded, and significant force amplitudes per unit width of barrier were calculated from the zeroth-moment of the force spectra as

$$F_{mo} = \frac{1}{2}\left(4\sqrt{m_o}\right)\frac{1}{B} \tag{VI-5-162}$$

where m_o is the area beneath the measured force spectrum and B is the horizontal width of the barrier. The 1/2-factor arises because the force spectrum also includes forces directed seaward, which are approximately the same magnitude as the landward directed forces (Kriebel et al. 1998).

(e) The relative force measurements per unit width of barrier are shown in Figure VI-5-62. The significant force per unit width (F_{mo}) is nondimensionalized by the significant force per unit width (F_o) for a vertical wall extending over the entire depth, given by the equation

$$F_o = \rho g H_{mo} \frac{\sinh k_p h}{k_p \cosh k_p h} \tag{VI-5-163}$$

where

ρ = water density

g = gravity

H_{mo} = incident significant wave height

k_p = wave number associated with the spectral peak period, T_p

h = water depth at the barrier

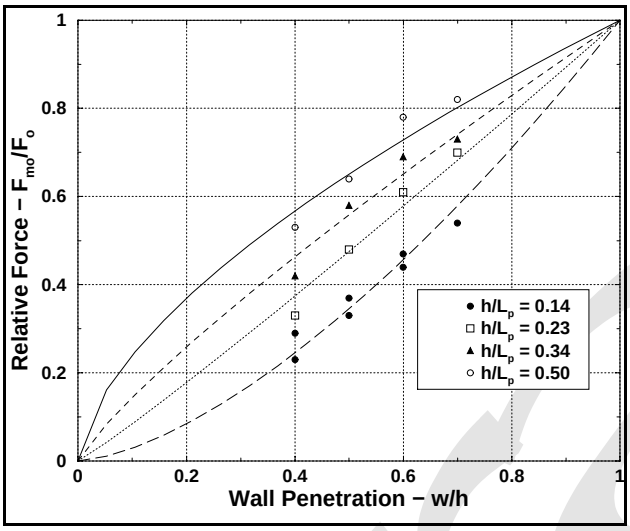

Figure VI-5-62. Best-fit to wave barrier force data

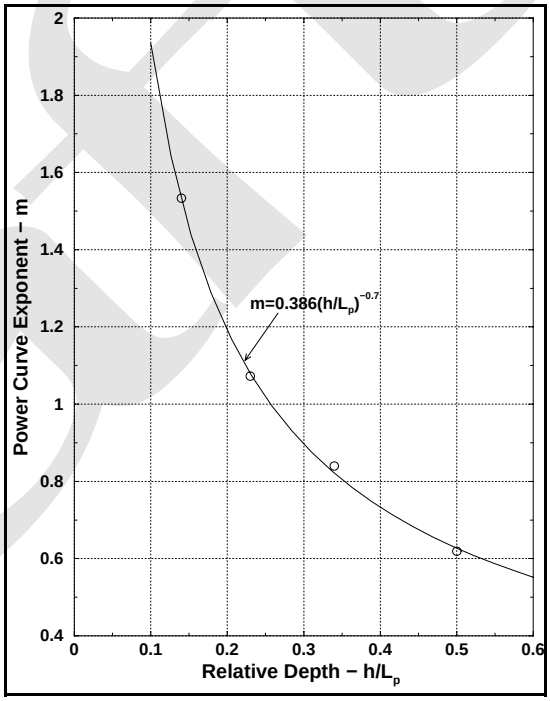

Figure VI-5-63. Power curve exponents

(f) The lines in Figure VI-5-62 are best-fit curves of the form $F_{mo}/F_o = (w/h)^m$. The exponents (m) are plotted in Figure VI-5-63 as a function of relative depth, h/L_p, along with a best-fit power curve.

(g) The resulting empirical predictive equation is then given by

$$F_{mo} = F_o \, (w/h)^{0.386\,(h/L_p)^{-0.7}} \qquad \text{(VI-5-164)}$$

where

F_{mo} = significant force per unit width of barrier

F_o = significant force per unit width of vertical wall (Equation VI-5-163)

w = barrier penetration depth

h = water depth

L_p = local wavelength associated with the peak spectral period, T_p

(h) A comparison of the measured force values versus estimates based on the empirical Equation VI-5-164 is shown in Figure VI-5-64.

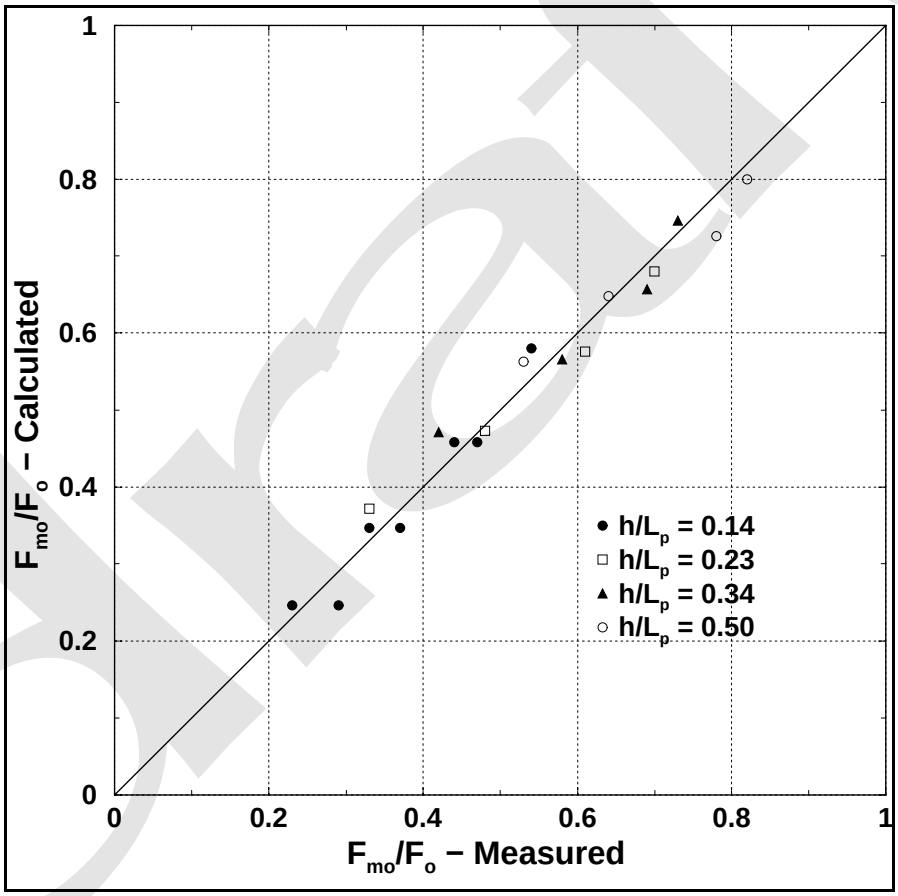

Figure VI-5-64. Comparison of Equation VI-5-139 to data used in empirical curve fits

(i) Use of Equation VI-5-164 should be limited to the range $0.4 < w/h < 0.7$ and $0.14 < h/L_p < 0.5$; however, estimates slightly outside the strict bound of the laboratory data are probably reasonable.

(j) The design force load on the vertical barrier should be the load corresponding to the design wave height, $H_{design} = 1.8\, H_s$ as recommended by Goda (1985). For Rayleigh distributed waves, $H_{design} = H_{1/250}$; and

by linear superposition, we can assume that force amplitudes will also be Rayleigh distributed. Thus, the design force load is determined as

$$F_{design} = 1.8\ F_{mo} \tag{VI-5-165}$$

(3) Structure length and alignment effects on wave height.

(a) Diffraction at the head of a structure creates variations in wave heights along the structure. For a semi-infinite, fully reflecting structure exposed to nonbreaking long-crested regular waves, Ito, Tanimoto, and Yamamoto (1972) calculated the ratio of the wave height along the structure, H, to the incident wave height, H_I, as

$$\frac{H}{H_I} = \sqrt{(C + S + 1)^2 + (C - S)^2} \tag{VI-5-166}$$

where

$$C = \int_0^u \cos(\frac{\pi}{2}t^2)dt \quad , \quad S = \int_0^u \sin(\frac{\pi}{2}t^2)dt \quad , \quad u = 2\sqrt{\frac{2x}{L}}\ \sin(\frac{\alpha}{2}) \tag{VI-5-167}$$

and x is the distance from the tip of the structure, L is the wavelength and α is the angle between the direction of wave propagation and the front alignment of the structure.

(b) Figure VI-5-65 shows an example of the wave height variation for regular head-on waves of period T = 10 s. Shown with the dotted line is the wave height variation calculated for nonbreaking long-crested irregular (random) waves (Bretschneider-Mitsuyasu spectrum, $T_{1/3}$ = 10 s). The smoothing effect of random seas is clearly seen. At some locations the wave height exceeds twice the incident wave height expected for infinitely long vertical wall structures.

(c) For short-length breakwaters, the diffraction from both ends of the structure influences the wave height variation (see Goda 1985). Also note that experiments indicate that the theoretical assumption of complete reflection of waves from smooth vertical walls appears not fulfilled, because reflection coefficients on the order of 0.95 have been measured. (However, the methods for measuring reflection are less than perfect, as well.) Oblique waves create wave height variations different from those created by head-on waves. Concave and convex corners also affect the wave height variation along the structure (see Part VI-5-4-e).

(4) Horizontal wave force reduction for nonbreaking waves.

(a) The effect of incident wave angle on the horizontal wave force exerted on a caisson is twofold. One effect is a force reduction, compared to head-on waves, due to the reduction of point pressure on the caisson, referred to as point-pressure force reduction. The second effect is a force reduction due to the fact that peak pressures do not occur simultaneously along the caisson, referred to as peak-delay force reduction. These two-force reduction effects will be present in short-crested waves because of spreading of the wave energy over a range of incident angles. Model test results Franco, van der Meer, and Franco (1996) with long-crested waves indicate that the point-pressure reduction can be estimated by the Goda formula.

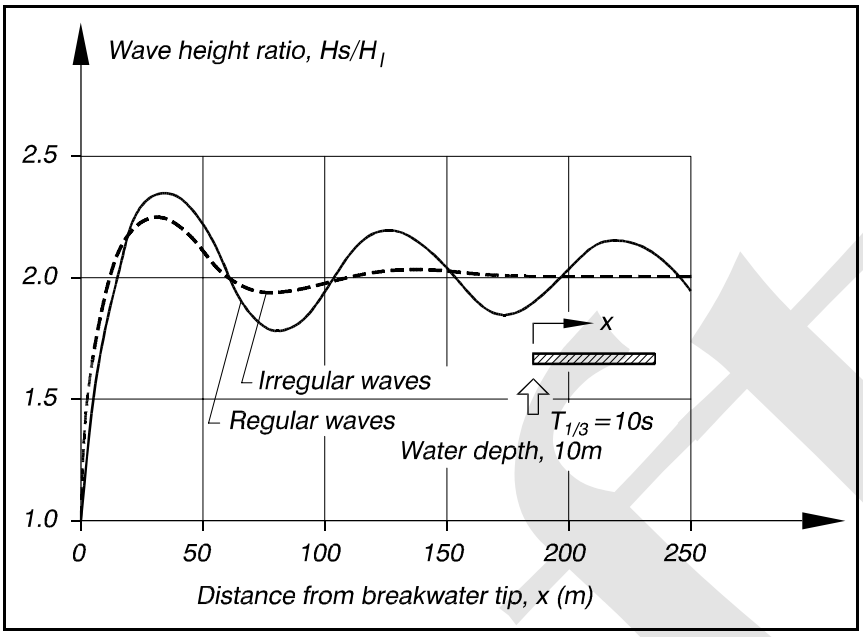

Figure VI-5-65. Variation of wave height along a semi-infinite, fully reflecting breakwater exposed to head-on, long-crested waves. (From Goda 1985)

(b) The peak-delay force reduction for oblique nonbreaking regular waves can be predicted by the Battjes formula (Battjes 1982)

$$r_F(L,\theta) = \frac{max.\ force,\ wave\ incident\ angle\ \theta}{max.\ force,\ head\text{-}on\ wave\ (\theta=0^o)} = \frac{\sin\left(\frac{\pi L_s}{L}\sin\theta\right)}{\frac{\pi L_s}{L}\sin\theta} \tag{VI-5-168}$$

where L and L_s are the wavelength and the structure length, respectively, and θ is the wave incident angle. Equation VI-5-168 is depicted in Figure VI-5-66. (In the figure β is used instead of θ.)

(c) The peak-delay force reduction for oblique nonbreaking long-crested irregular waves can be estimated by the formula (Burcharth and Liu 1998)

$$r_F(L_p,\theta) = \frac{characteristic\ wave\ force,\ wave\ incident\ angle\ \theta}{characteristic\ wave\ force,\ head\text{-}on\ wave\ (\theta=0^o)} = \left| \frac{\sin\left(\frac{\pi L_s}{L_p}\sin\theta\right)}{\frac{\pi L_s}{L_p}\sin\theta} \right| \tag{VI-5-169}$$

where L_p is the wavelength corresponding to the peak frequency. For example, the characteristic wave force can be chosen as F_{max}, $F_{1/250}$, $F_{1\ percent}$, $F_{10\ percent}$, etc.

(d) In order to investigate the uncertainty and bias of Equation VI-5-169, a real-time calculation of the wave force on a caisson by nonbreaking long-crested irregular waves was performed by Burcharth and Liu (1998). The result is given in Figure VI-5-67.

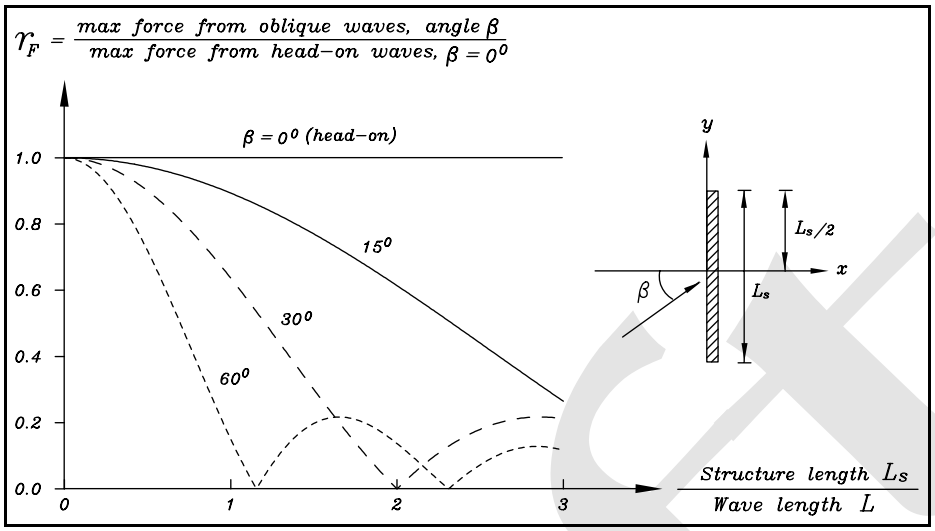

Figure VI-5-66. Peak-delay force reduction for oblique regular waves (Burcharth and Liu 1998)

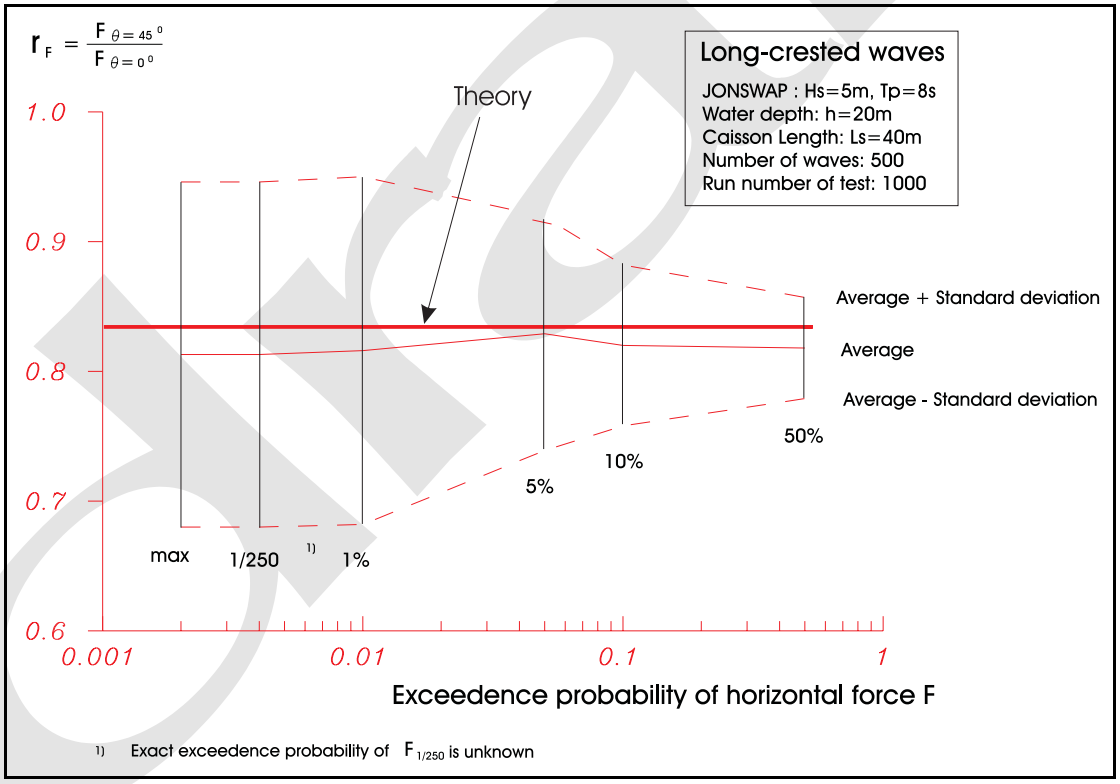

Figure VI-5-67. Numerical simulation of peak-delay reduction, long-crested waves. Example of uncertainty calculation for wave train with 500 waves (Burcharth and Liu 1998)

(e) Figure VI-5-67 shows that Equation VI-5-169 gives a close estimate of the mean value of the peak-delay reduction. However, a large variation of the peak-delay force reduction factor corresponding to a low exceedence probability, e.g., $F_{1/250}$, was observed.

(f) The peak-delay force reduction for oblique nonbreaking short-crested waves can be estimated by the formula (Burcharth and Liu 1998)

$$r_F(\sigma,\theta_m) = \frac{\textit{characteristic wave force, short-crested wave}}{\textit{characteristic wave force, head-on long-crested wave}} \approx \approx \left(\int_{-\pi}^{\pi} r_F(L_p,\theta)\ D(\sigma,\theta_m)\, d\theta \right)^{1/2} \tag{VI-5-170}$$

where $r_F(L_p,\theta)$ is given by Equation VI-5-169 and $D(\sigma,\theta_m)$ is the wave directional spreading function with the wave energy spreading angle σ and the mean wave incident direction θ_m. An example of Equation VI-5-170 is depicted in Figure VI-5-68.

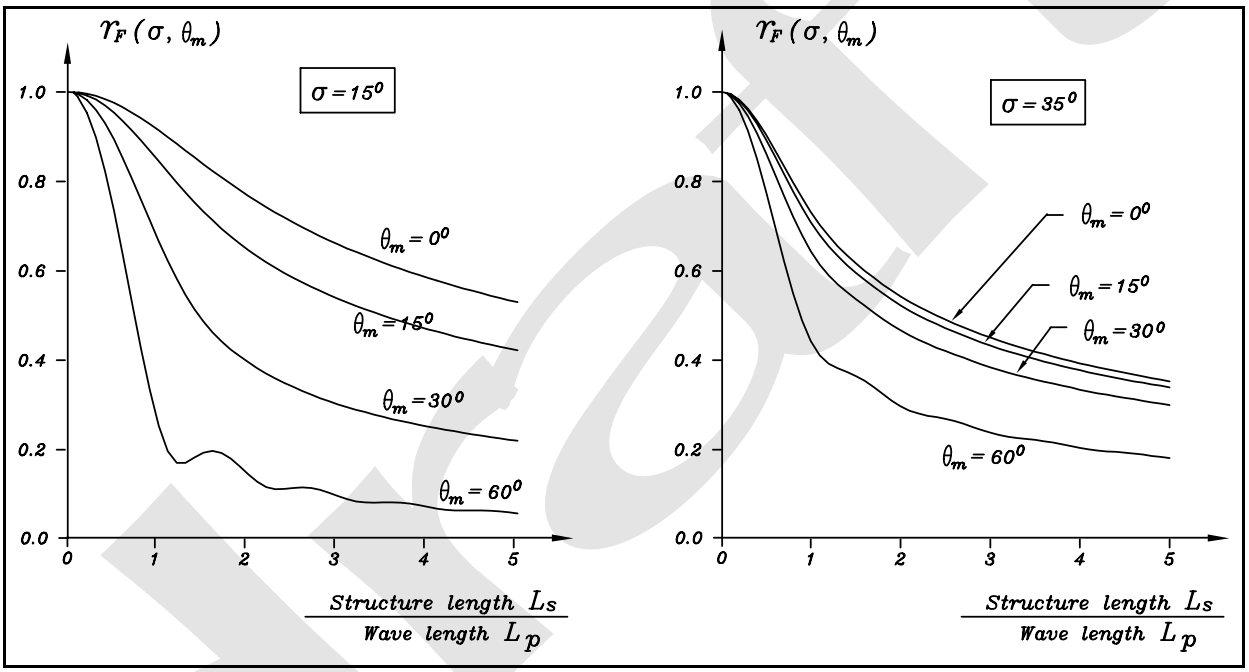

Figure VI-5-68. Example of peak-delay force reduction for short-crested waves (Burcharth and Liu 1998)

(5) Horizontal turning moment for nonbreaking waves.

(a) Oblique wave attack generates resultant wave forces acting eccentrically on the caisson front. The horizontal turning moment around the caisson center caused by oblique regular waves can be estimated by the formula (Burcharth 1998)

$$r_M = \frac{max.\ moment,\ wave\ incident\ angle\ \theta}{(head\text{-}on\ max.\ force)\ x\ (structure\ length)} =$$

$$= \frac{1}{2}\left| \frac{\cos\left(\frac{\pi\ L_s}{L}\sin\theta\right)}{\frac{\pi\ L_s}{L}\sin\theta} - \frac{\sin\left(\frac{\pi\ L_s}{L}\sin\theta\right)}{\left(\frac{\pi\ L_s}{L}\sin\theta\right)^2} \right| \qquad \text{(VI-5-171)}$$

Equation VI-5-171 is depicted in Figure VI-5-69. The maximum horizontally turning moment around caisson center under arbitrary wave incident angle is

$$M_{\max} = 0.22\ F_{\theta=0^o}\ L_s \qquad \text{(VI-5-172)}$$

where $F_{\theta=0}{}^o$ is the maximum head-on wave force.

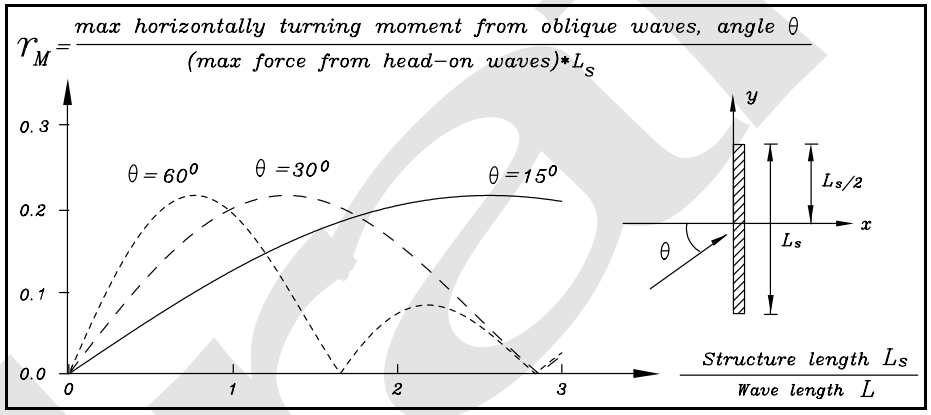

Figure VI-5-69. Nondimensional amplitude of horizontal turning moment around the center of the caisson exposed to oblique nonbreaking regular waves

(6) Horizontal wave force reduction for breaking waves.

(a) Short-crested waves break in a limited area and not simultaneously along the whole caisson, which results in an even larger force reduction in comparison with nonbreaking waves. Figure VI-5-70 shows an example of force reduction from model tests with short-crested, breaking, head-on waves, where the force reduction r_F is defined as

$$r_F = \frac{F_{1/250},\ short\text{-}crested\ wave,\ mean\ wave\ incident\ angle\ \theta_m}{F_{1/250},\ long\text{-}crested\ head\text{-}on\ wave} \qquad \text{(VI-5-173)}$$

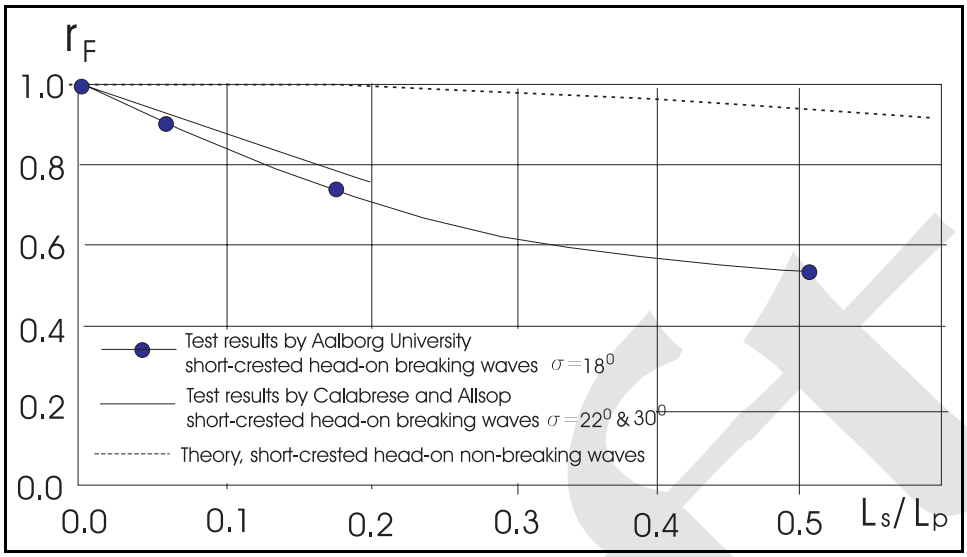

Figure VI-5-70. Example of force reduction from model tests with short-crested breaking waves (Burcharth 1998, Calabrese and Allsop 1997)

(7) Broken wave forces.

(a) Shore structures may be located where they are only subjected to broken waves under the most severe storm and tide condition. Detailed studies relating broken wave forces to incident wave parameters and beach slope are lacking; thus simplifying assumptions are used to estimate design loads. Critical designs should be confirmed with physical model tests.

(b) Model tests have shown approximately 78 percent of the breaking wave height (0.78 H_b) is above the still-water line when waves break on a sloping beach (Wiegel 1964). The broken wave is assumed to decay linearly from the breakpoint to the intersection of the swl with the beach slope, where the wave height is reduced to a height of $H_{swl} = 0.2\ H_b$ for beach slopes in the range $0.01 \le \tan\beta \le 0.1$ (Camfield 1991). The water mass in the broken wave is assumed to move shoreward with velocity equal to the breaking wave celery by linear theory, i.e., $C = (gh_b)^{1/2}$.

• Vertical wall seaward of the shoreline. Vertical walls situated seaward of the SWL/beach intersection are subjected to wave pressures composed of dynamic and hydrostatic pressures as illustrated in the sketch of Figure VI-5-71. The wave height at the wall, H_w, is determined by similar triangles to be

$$H_w = \left(0.2 + 0.58\ \frac{h_s}{h_b}\right) H_b \qquad \text{(VI-5-174)}$$

where h_s is the water depth at the wall, and h_b is the water depth at wave breaking.

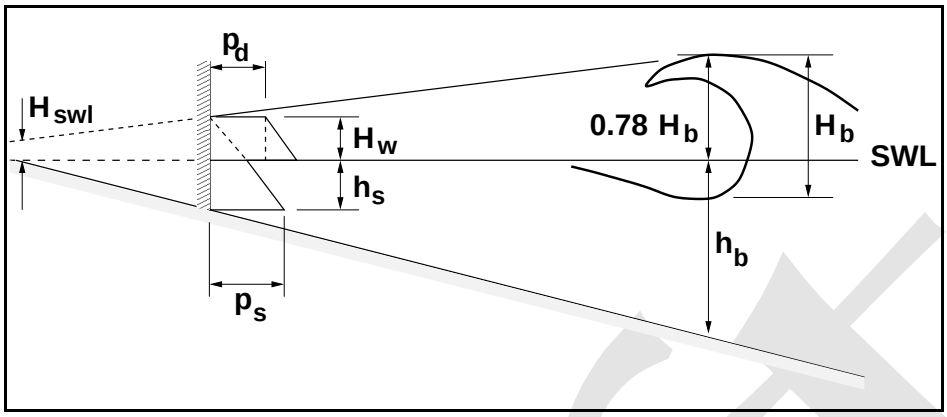

Figure VI-5-71. Broken wave forces on wall seaward of shoreline

- Above the swl, the dynamic component of the pressure is given as

$$p_d = \frac{1}{2}\rho C^2 = \frac{1}{2}\rho g h_b \tag{VI-5-175}$$

and the corresponding force per unit horizontal length of the wall is

$$R_d = p_d H_w = \frac{\rho g h_b H_w}{2} \tag{VI-5-176}$$

where ρ is the density of water. The overturning moment per unit horizontal length about the toe of the wall due to the dynamic pressure is given by

$$M_d = R_d \left(h_s + \frac{H_w}{2} \right) \tag{VI-5-177}$$

- The hydrostatic pressure varies from zero at a height H_w above the SWL to a maximum at the base of the wall given by

$$P_s = \rho g (h_s + H_w) \tag{VI-5-178}$$

- The hydrostatic force per unit horizontal width of the wall is calculated as

$$R_s = \frac{\rho g}{2}(h_s + H_w)^2 \tag{VI-5-179}$$

and the corresponding hydrostatic overturning moment per unit width is

$$M_s = R_s \left(\frac{h_s + H_w}{3} \right) = \frac{\rho g}{6} (h_s + H_w)^3 \quad \text{(VI-5-180)}$$

- The total force and moment per unit horizontal width of wall is the summation of dynamic and hydrostatic components, i.e.,

$$R_T = R_d + R_s \quad \text{(VI-5-181)}$$

$$M_T = M_d + M_s \quad \text{(VI-5-182)}$$

- Any backfilling with sand, soil or stone behind the wall will help resist the hydrodynamic forces and moments on the vertical wall.

- Vertical wall landward of the shoreline. Landward of the intersection of the SWL with the beach and in the absence of structures, the broken wave continues running up the beach slope until it reaches a maximum vertical runup height, R_a, that can be estimated using the procedures given in Part II-4-4, "Wave Runup on Beaches." If a vertical wall is located in the runup region, as shown in Figure VI-5-72, the surging runup will exert a force on the wall that is related to the height, H_w, of the surge at the wall.

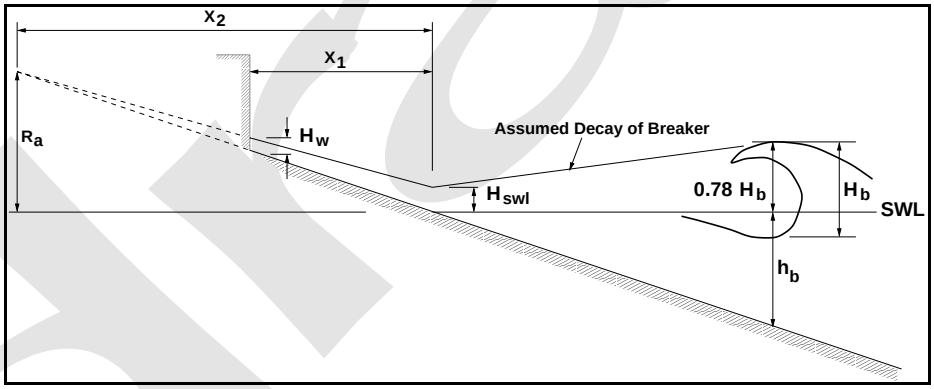

Figure VI-5-72. Broken wave forces on wall landwater of shoreline

- Camfield (1991) assumed a linear decrease in the runup surge over the distance X_2 shown in Figure VI-5-72 which yielded the following expression for surge height at the wall

$$H_w = H_{SWL} \left(1 - \frac{X_1}{X_2} \right) = 0.2 H_b \left(1 - \frac{X_1 \tan\beta}{R_a} \right) \quad \text{(VI-5-183)}$$

where $H_{SWL} \approx 0.2\ H_b$ and β is the beach slope angle. The force of the surge per unit horizontal width of the vertical wall was approximated by Camfield (1991) based on the work of Cross (1967) to be

$$F_{surge} \approx 4.5 \rho g H_w^2 \tag{VI-5-184}$$

or when combined with Equation VI-5-158

$$F_{surge} \approx 0.18 \rho g H_b^2 \left(1 - \frac{X_1 \tan\beta}{R_a} \right)^2 \tag{VI-5-185}$$

- This approximate method is intended for use on plane slopes in the range $0.01 \le \tan\beta \le 0.1$. The methodology does not apply to steeper slopes or composite slopes. No estimates are given for the pressure distribution or the resulting overturning moment on the vertical wall.

c. Wave-generated forces on concrete caps.

(a) Wave loads on concrete caps occur only if the runup reaches the wall. The load is very dependent, not only on the characteristics of the waves, but also on the geometry (including the porosity) of the seaward face of the structure.

(b) The wave forces on a monolithic superstructure exposed to irregular waves are of a stochastic nature. The pressure distributions and the related resultant forces at a given instant are schematized in Figure VI-5-73. Not included in the figure is the distribution of the effective stresses on the base plate.

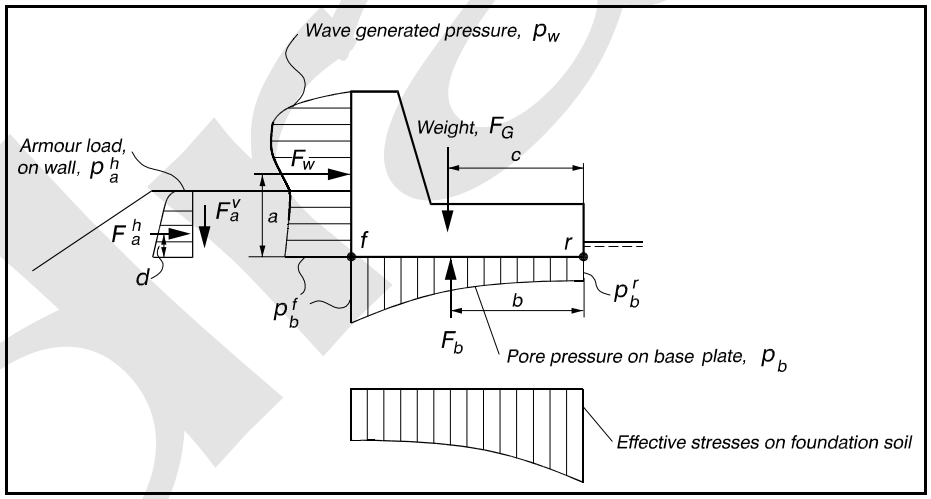

Figure VI-5-73. Illustration of forces on a superstructure

(c) The wave-generated pressure, p_w, acting perpendicular to the front of the wall is the pressure that would be recorded by pressure transducers mounted on the front face. The distribution of p_w is greatly affected by very large vertical velocities and accelerations which often occur. F_w is the instantaneous resultant of the wave generated pressures.

(d) The instantaneous uplift pressure, p_b, acting perpendicular to the base plate is equal to the pore pressure in the soil immediately under the plate. The resultant force is F_b. At the front corner (point f) the uplift pressure p_b^f, equals the pressure on the front wall. At the rear corner (point r) the uplift pressure, p_b^r,

equals the hydrostatic pressure at point *r*. The actual distribution of p_b between p_b^f and p_b^r depends on the wave-generated boundary pressure field and on the permeability and homogeneity of the soil. The distribution cannot be determined in normal wave flume scale tests because of strong scale effects related to porous flow. However, the corner pressures p_b^f and p_b^r can be measured or estimated, and in case of homogeneous and rather permeable soils and quasi-static conditions, a safe estimate on the most dangerous uplift can be found assuming a linear pressure distribution between a maximum value of p_b^f and a minimum value of p_b^r as shown in Figure VI-5-74a. If a blocking of the porous flow is introduced on the seaside of the base, the assumption of a linear distribution will be even safer as illustrated by Figure VI-5-74b. On the other hand a blockage under the rear end of the base plate might cause the linear assumption to be on the unsafe side as illustrated by Figure VI-5-74c. Note, that in case b and c the resultant of the base plate pressure is not vertical.

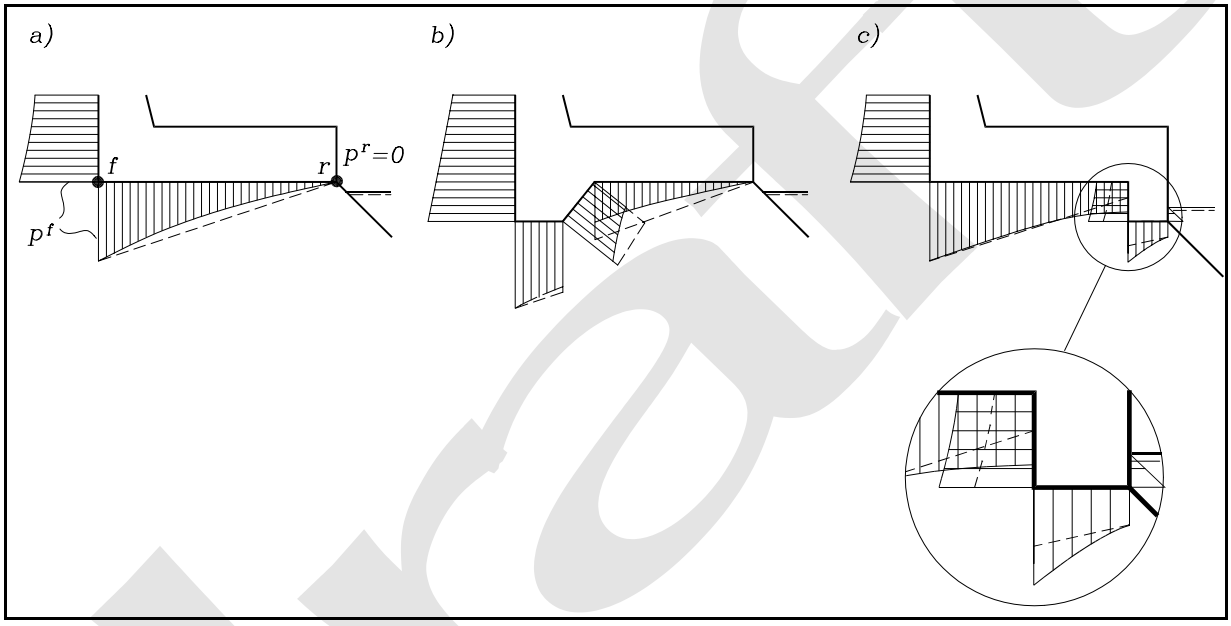

Figure VI-5-74. Illustration of comparison between base plate pore pressure distributions (under quasi-static porous flow conditions) and the approximated linear distribution

(e) Armor and filter stones resting against the front of the wave wall will introduce an armor load, p_a, on the front through the contact points. Both a normal soil mechanics load and a proportion of the dynamic wave loads on the armor contribute to p_a. The resultant force F_a is generally not perpendicular to the front wall due to friction between the soil and the wall, and must be split into the two orthogonal components F_a^h and F_a^v. In the case of high walls (low front berms) F_a is insignificant compared to the wave load, F_w.

(f) The load will in general be dynamic but is normally treated as quasi-static due to a rather smooth variation in time over a wave period. However, if wave breaking takes place directly on the wall face some short duration, but very large, slamming forces can occur, especially if the front face is almost vertical at the moment when the wave collides with the wall as shown in Figure VI-5-75. Such forces are also called impact or impulsive forces.

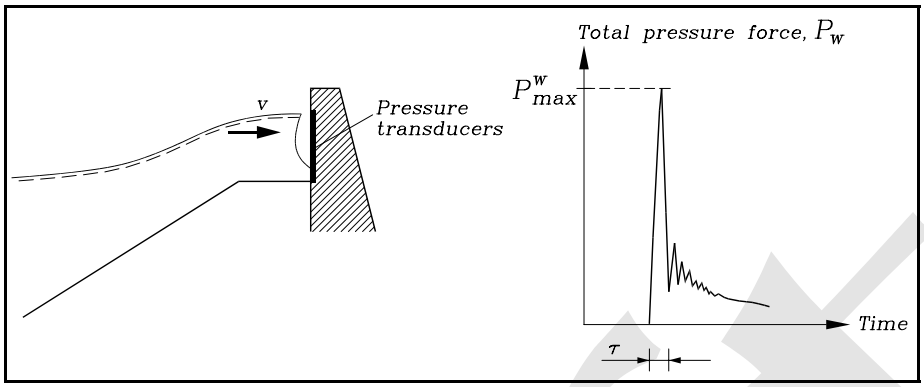

Figure VI-5-75. Impulsive pressure force caused by wave breaking on the wave wall

(g) Wave slamming on the wall can be avoided and the quasi-static wave loads reduced by increasing the crest level and/or the width of the front berm as shown by Figure VI-5-76. Wave slamming on the front of the wall will not occur in configurations c and d.

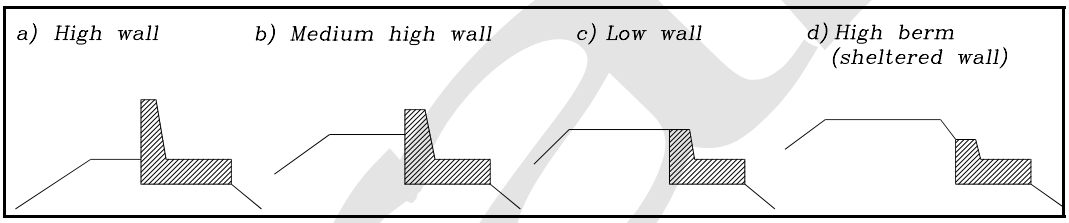

Figure VI-5-76. Typical crown wall configurations

(h) The wave loadings on a crown wall can be assessed only by physical model tests or by prototype recordings. However, no prototype results have been reported in the literature and most model test results are related to specific crown wall configurations.

(i) Table VI-5-60 shows an empirical formula for horizontal wave load given by Jensen (1984) and Bradbury et al. (1988). Table VI-5-61 shows empirical formulae for horizontal wave load, turning moment and uplift pressure presented by Pedersen (1996). The formulae are based on small scale model tests with head-on irregular waves. Predictions are compared to measurements in Figure VI-5-77.

Table VI-5-60
Horizontal Wave Force on Concrete Caps (Jensen 1984; Bradbury et al. 1988)

$$\frac{F_{h,0.1\%}}{\rho_w\, g\, h_w\, L_{op}} = \alpha + \beta \frac{H_s}{A_C} \qquad \text{(VI−5−186)}$$

where $F_{h,0.1\%}$ Horizontal wave force per running meter of the wall corresponding to 0.1% exceedence probability
ρ_w Mass density of water
h_w Crown wall height
L_{op} Deepwater wavelength corresponding to peak wave period
H_s Significant wave height in front of breakwater
A_c Vertical distance between MWL and the crest of the armor berm
α, β Fitted coefficient, see table

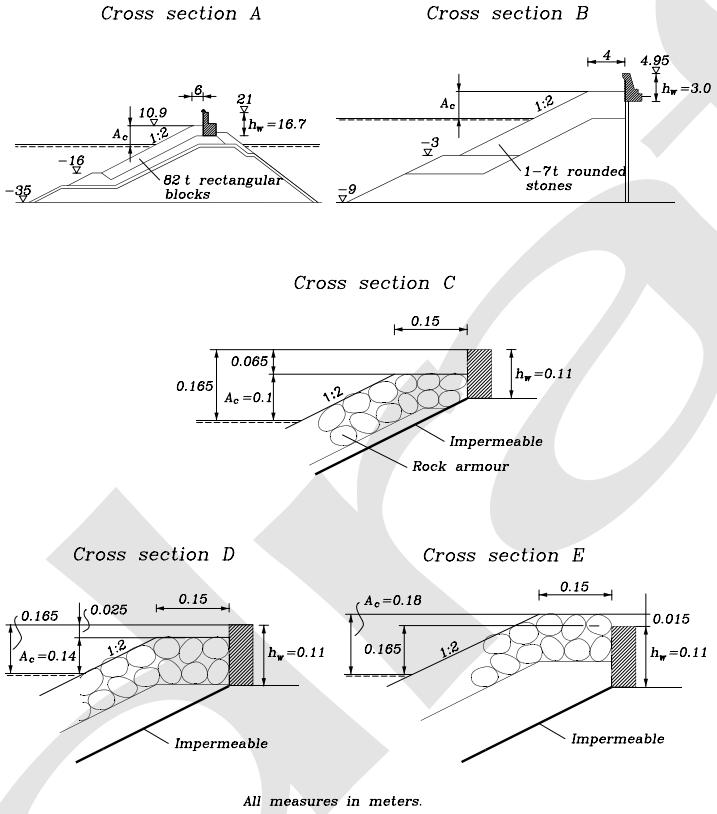

Cross section	Parameter ranges in tests			0.1% exceedence values of coefficients in Eq (VI-5-186)		Coefficient of variation	Reference
	A_c (m)	$s_{op} = \frac{H_s}{L_{op}}$	$\frac{H_s}{A_c}$	α	β		
A	5.6 - 10.6	0.016 - 0.036	0.76 - 2.5	−0.026	0.051	0.21	Jensen (1984)
B	1.5 - 3.0	0.05 - 0.011	0.82 - 2.4	−0.016	0.025	0.46	—
C	0.10	0.023 - 0.07	0.9 - 2.1	−0.038	0.043	0.19	Bradbury, et al. (1988)
D	0.14	0.04 - 0.05	1.43	-0.025	0.028		—
E	0.18	0.04 - 0.05	1.11	-0.088	0.011		—

Table VI-5-61
Horizontal Wave Force, Uplift Wave Pressure and Turning Moment on Concrete Caps (Pedersen 1996)

.

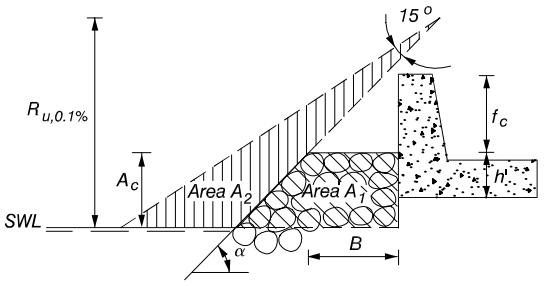

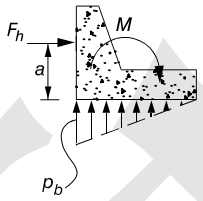

$$F_{h,0.1\%} = 0.21\sqrt{\frac{L_{om}}{B}}\left(1.6 p_m y_{eff} + A\frac{p_m}{2}h'\right) \qquad \text{(VI-5-187)}$$

$$M_{0.1\%} = a \times F_{h,0.1\%} = 0.55(h' + y_{eff})F_{h,0.1\%} \qquad \text{(VI-5-188)}$$

$$p_{b,0.1\%} = 1.00\ A\ p_m \qquad \text{(VI-5-189)}$$

where

$F_{h,0.1\%}$ Horizontal wave force per running meter of the wall corresponding to 0.1% exceedence probability

$M_{0.1\%}$ Wave generated turning moment per running meter of the wall corresponding to 0.1% exceedence probability

$p_{b,0.1\%}$ Wave uplift pressure corresponding to 0.1% exceedence probability

L_{om} Deepwater wavelength corresponding to mean wave period

B Berm width of armor layer in front of the wall

p_m $p_m = \rho_w g(R_{u,0.1\%} - A_c)$

$R_{u,0.1\%}$ Wave runup corresponding to 0.1% exceedence probability

$$R_{u,0.1\%} = \begin{cases} 1.12 H_s \zeta_m & \zeta_m \le 1.5 \\ 1.34 H_s \zeta_m^{0.55} & \zeta_m > 1.5 \end{cases}$$

$$\zeta_m = \tan\alpha / \sqrt{H_s / L_{om}}$$

α Slope angle of armor layer

A_c Vertical distance between MWL and the crest of the armor berm

A $A = \min\{A_2/A_1, 1\}$, where A_1 and A_2 are areas shown in the figure

y_{eff} $y_{eff} = \min\{y/2, f_c\}$

$$y = \begin{cases} \frac{R_{u,0.1\%} - A_c}{\sin\alpha}\frac{\sin 15^0}{\cos(\alpha - 15^0)} & y > 0 \\ 0 & y \le 0 \end{cases}$$

h' Height of the wall protected by the armor layer

f_c Height of the wall not protected by the armor layer

Uncertainty of the formulae

factor in the formulae	0.21	1.6	0.55	1.00
standard deviation σ	0.02	0.10	0.07	0.30

Tested range: See Table VI-5-12

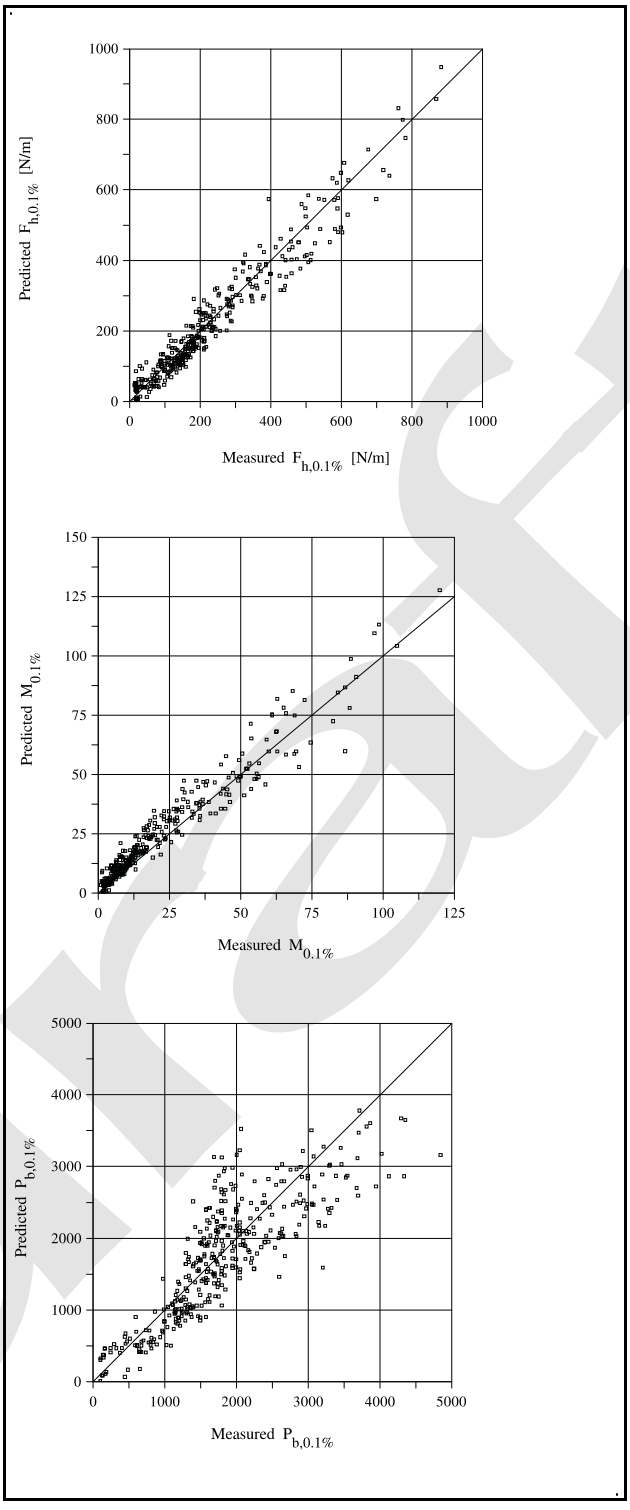

Figure VI-5-77. Comparison of predictions to measurements using the methods in Table VI-5-61 (from Pedersen 1996)

d. Stability of concrete caps and caissons against sliding and overturning.

(1) Stability against sliding between the caisson base and the rubble foundation requires

$$(F_G - F_U)\ \mu \geq F_H \tag{VI-5-190}$$

where

μ = friction coefficient for the base plate against the rubble stones

F_G = buoyancy-reduced weight of the caisson

F_U = wave induced uplift force

F_H = wave induced horizontal force

(2) Overturning can take place only when the heel pressure under the caisson is less than the bearing capacity of the foundation. If the caisson is placed on rubble stones and sand it is unlikely that overturning will occur. Instead there will be soil mechanics failure. Overturning is a realistic failure mode only if the caisson is placed on rock or on very strong clay, in which case breakage of the caisson is likely to occur.

(3) Stability against overturning is maintained if

$$M_{FG} \geq M_{FU} + M_{FH} \tag{VI-5-191}$$

where

M_{FG} = stabilizing moment around the heel by buoyancy-reduced weight of the caisson

M_{FU} = antistabilizing moment by wave induced uplift force

M_{FH} = antistabilizing moment by wave induced horizontal force

(4) The value of the friction coefficient μ has been investigated in models and in prototype studies. For a plane concrete slab resting on quarried rubble stones, Takayama (1992) found as an average a static friction coefficient of $\mu = 0.636$ and a coefficient of variation of 0.15. Table VI-5-62 taken from Stückrath (1996), presented experimental test results of friction coefficients conducted in Japan.

(5) French tests (Cété-Laboratoire Régional Norde-Pas de Calais 1990) give a somewhat lower friction coefficient as shown in Table VI -5-63.

(6) Morihira, Kihara, and Horikawa[1] investigated the dynamic friction coefficient between caissons with different bottom patterns and rubble foundation with different levelling as shown in Table VI-5-64.

[1] Personal Communication, 1998, M. Marihira, T. Kihara, and H. Horikawa. "On the Friction Coefficients Between Concrete Block Sea Walls and Rubble-Mound Foundations."

Table VI-5-62
Experimental Test Results of Friction Coefficient Conducted in Japan (taken from Stückrath 1996)

No.	Stone type	Stone size (mm)	Condition of mound	μ	Average of μ
1	Crushed stone	30	Screeded surface	0.460-0.801	-
2	Rubble stone	120	Not screeded	0.564-0.679	0.624
3	Rubble stone	50	Surface smoothed with smaller stone	0.45-0.69	-
4	Rubble stone	30-80	Screeded	0.77-0.89	0.82
5	Cobble stone	30-50	Not screeded	0.69-0.75	0.70
6	Crushed stone	20-30	Not screeded	0.607-0.790	0.725
7	Crushed stone	10-50	Not screeded	0.486-0.591	0.540
8	Crushed stone	13-30	Not uniform	0.41-0.56	-

Table VI-5-63
Experimental Test Results of Friction Coefficient (Cété-Laboratoire Régional Norde-Pas de Calais 1990)

Vertical Load (tonne)	Normal Stress (tonne/m^2)	Horizontal Force (tonne)		Friction Coefficient μ	
		Smooth	Corrugated	Smooth	Corrugated
Natural Sea Gravel 20-80 mm					
24.1	10.5	12.6	13.7	0.53	0.58
18.4	8	10.3	11.3	0.56	0.62
Crushed Gravel 0-80 mm					
24.1	10.5		10.4		0.43
18.4	8		8.6		0.47

e. Waves at structure convex and concave corners. Many projects have coastal structures featuring concave or convex bends or sharp corners corresponding to structure realignment. Usually, the location and curvature of corners are determined by functional design factors, such as harbor layout or proposed channel alignment, or by site considerations, such as bathymetry. Regardless of the functional design motivation, structure bends and corners must meet or exceed the same design criteria as the rest of the structure. The orientation of bends and corners relative to the incident waves may cause changes in the local wave characteristics due to refraction, reflection, and focussing effects. Changes in wave heights could affect armor stability on the corner section, and local crest elevation may have to be heightened to prevent increased overtopping. Convex corners and bends are defined as having an outward bulge facing the waves, whereas concave corners and bends have a bulge away from the waves. Figure VI-5-78 illustrates convex and concave configurations for vertical-wall structures. Similar definitions are used for sloping-front structures.

Table VI-5-64
Dynamic Friction Coefficient Between Caisson Bottom and Rubble-Mound (Morihira, Kihara, and Harikawa, personal communication 1998)

Levelling method for rubble mound

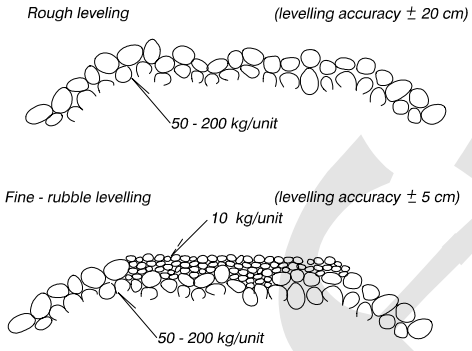

Bottom pattern of caissons

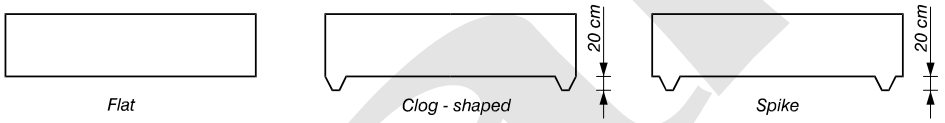

Table of Dynamic friction coefficients

Levelling	Bottom pattern	μ_{max}	$\overline{\mu_{max}}$	μ_{const}	μ			
					S=5 cm	S=10 cm	S=20 cm	S=30 cm
rough	flat	0.75	0.70	0.70	0.53	0.59	0.65	0.70
		0.73	0.70	0.70	0.70	0.70	0.70	0.70
	clog-shaped	1.19	1.13	1.16	0.76	0.91	0.98	1.08
		1.11	1.02	1.01	0.76	0.90	1.01	1.00
	spike	0.85	0.79	0.80	0.62	0.80	0.80	0.80
		0.97	0.81	0.84	0.70	0.70	0.83	0.95
	clog-shaped with foot protection	1.45	1.36	>1.4	1.11	1.30	1.41	
		1.34	1.19	>1.3	0.94	1.09	1.28	
fine	flat	0.68	0.63	0.65	0.63	0.64	0.64	0.55
		0.70	0.60	0.60	0.59	0.60	0.60	0.60
	clog-shaped	1.18	1.08	1.08	0.95	1.03	1.08	1.08
		1.15	1.01	1.06	0.90	0.94	0.97	1.04
	spike	0.87	0.78	0.82	0.72	0.72	0.75	0.82
		1.04	0.87	0.82	0.78	0.95	1.01	0.85

μ_{max} dynamic friction coefficient corresponding to maximum tensile load
$\overline{\mu_{max}}$ dynamic friction coefficient corresponding to the average of the peak tensile loads
μ_{const} dynamic friction coefficient corresponding to constant tensile load
μ dynamic friction coefficient corresponding to caisson displacement S
S caisson displacement

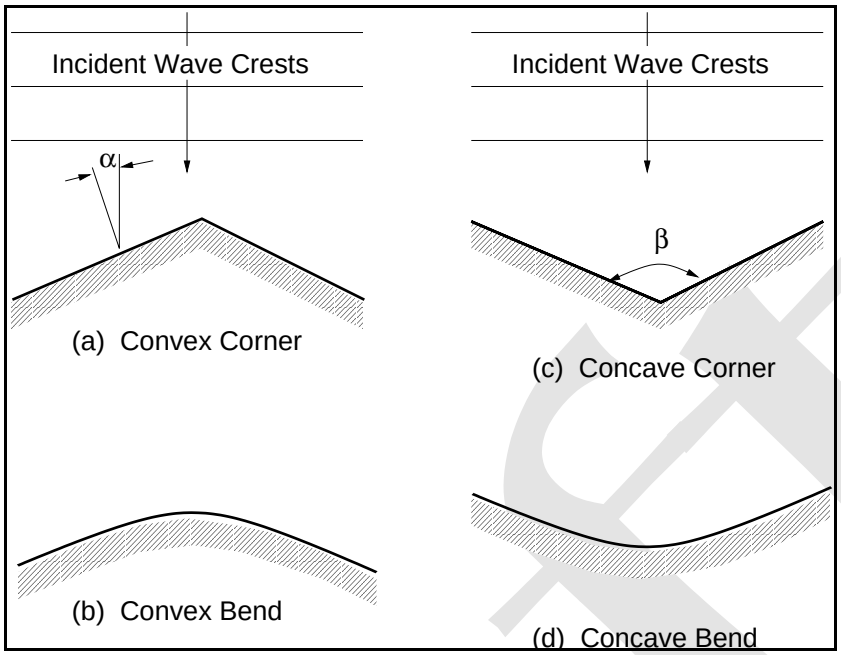

Figure VI-5-78. Convex and concave corners and bends at vertical walls

(1) Waves at convex corners.

(a) Vertical structures with convex corners. Waves approaching vertical walls with sharp convex corners such as depicted in Figure VI-5-78a will be almost perfectly reflected if the wall is impervious. This results in a diamond-like wave pattern of incident and reflected waves with the wave crests and troughs at the wall appearing to move along the wall. The maximum wave height at the wall depends on the incident wave height, H_i, angle of wave approach, α, and wave nonlinearity.

- Perroud (1957) performed laboratory tests of solitary waves obliquely reflected by a vertical wall. He observed "normal reflection" with the angle of reflection nearly the same as the incident wave angle for cases where the incident wave angle, α (defined in Figure VI-5-78), was less than about 45 deg. This is the same result given by linear wave theory for oblique reflection. The reflected wave height was just slightly less than the incident wave height for small incident angles, and it decreased as angle of incidence increased. This is contrary to linear wave theory. The maximum wave height at the wall was about twice the incident wave height up to $\alpha = 45$ deg, similar to linear wave theory for oblique reflection.

- For wave incident angles between about 45 deg and 70 deg Perroud observed a phenomenon referred to as "Mach reflection" in acoustics. Mach reflection of water waves is a nonlinear effect characterized by the presence of a reflected wave and a "Mach" wave with its crest propagating perpendicular to the vertical wall. The reflected wave height is significantly less than the incident wave height, and the angle of the reflected wave becomes less than the incident wave angle. The Mach reflection wave grows in length as it moves along the wall, and the maximum wave height, known as the "Mach stem" occurs at the wall.

- Figure VI-5-79 presents Perroud's (1957) averaged results for solitary waves obliquely reflected by a vertical wall. The upper plot shows the wave height at the wall in terms of the incident wave height for increasing angle of wave incidence. The ratio of reflected to incident wave height is

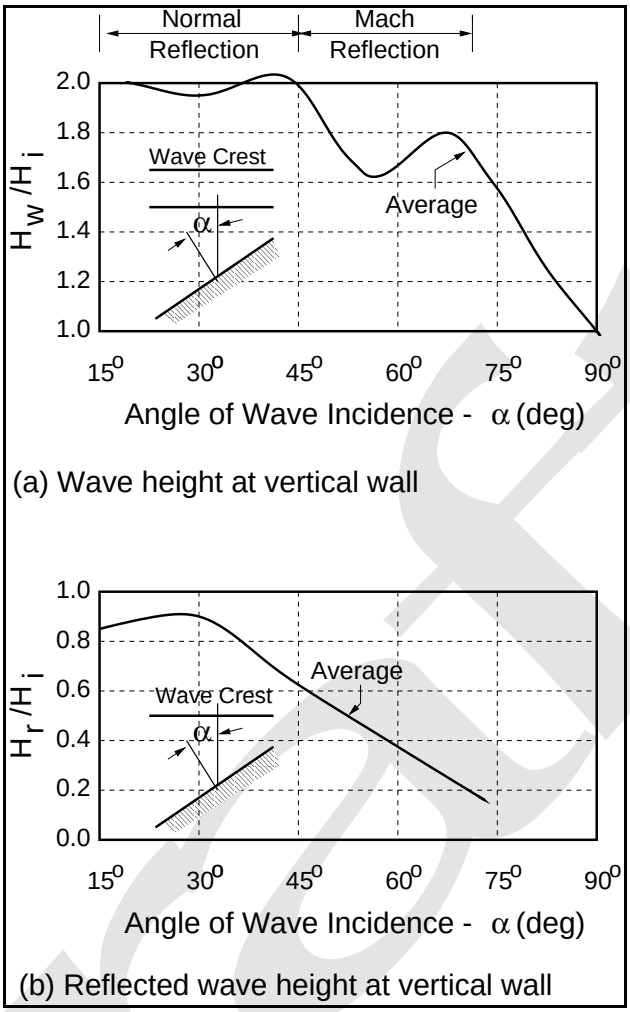

Figure VI-5-79. Mach reflection at a vertical wall (after Wiegel 1964)

shown in the lower plot. These plots are also given by Wiegel (1964) along with additional plots showing the decrease in reflected wave angle for Mach reflection and the increasing length of the Mach reflection wave with distance along the wall. (Note: In Wiegel (1964) the plots are given in terms of a differently defined angle of wave incidence i which is related to α via ($i = 90^o - \alpha$).)

- The speed of the Mach stem, C_M, was given as (Camfield 1990)

$$C_M = \frac{C}{\sin\alpha} \tag{VI-5-192}$$

where C is the incident wave celerity.

- For angles of incidence greater than 70 deg from normal, Perroud observed that the wave crest bends so it is perpendicular to the vertical wall, and no discernible reflected wave appears. The wave height at the wall decreases with continuing increase in angle of incidence as indicated in Figure VI-5-79a.

- Keep in mind that the experimental results were obtained for Mach reflection of solitary waves. This implies that the results represent the shallow-water limiting case. The Mach reflection effect will decrease for smaller amplitude waves in deeper water.

- Vertical walls with bends rather than sharp corners (Figure VI-5-78b) produce somewhat more complicated wave reflection patterns. Along the structure bend, the local angle of wave incidence varies, as does the reflected wave angle. Consequently, accurate estimates of maximum wave height along the vertical bend are best accomplished using laboratory tests or capable numerical wave models. Estimates from Figure VI-5-79 using the local angle of wave incidence should provide a reasonable approximation for mild bends. Vertical walls with very short radii bends are analogous to the seaward portion of large diameter vertical cylinders, and wave estimation techniques used in the offshore engineering field should be appropriate.

(b) Sloping structures with convex corners. The majority of coastal structures have impermeable or rubble-mound sloping fronts. Convex corners and bends for sloping-front structures are defined the same as illustrated in Figure VI-5-78 for vertical walls. Sharp corners are more likely on smooth, impermeable slopes whereas rubble-mound structures will have more rounded bends. Chen (1961) conducted experiments with solitary waves approaching smooth, impermeable slopes at oblique angles. For steep slopes the resulting wave behavior was similar to vertical walls with the onset of Mach reflection at larger angles of wave incidence. As the wall slope decreased, a large horizontal eddy formed over the slope. Further decreasing of the structure slope led to wave breaking along the slope. Generally, the onset of wave breaking depends on structure slope, incident wave angle, and the ratio of wave height to water depth (H/h). Chen's experiments used only one value of H/h so this relationship was not quantified. Rubble-mound structures with convex corners and bends may have armor stability problems for short-radius bends. In this case the bend is similar to the head section of a breakwater or jetty structure. Sakaiyama and Kajima (1997) conducted model tests of armor stability at convex bends in a structure protecting a manmade island. They found that armor stability increased as the bend radius increased. In many cases, armor stability at bends and corners is confirmed with physical model tests before construction begins. For short-radius bends an alternative is to use armor stability guidance developed for head sections. Increasing the bend radius will increase armor stability, but the tradeoff is greater quantities of construction materials.

(2) Waves at concave corners.

(a) Vertical structures with concave corners. Goda (1985) provided a simple formula for estimating the increased wave height at the apex of a concave corner of angle β formed by two impermeable vertical walls as illustrated by Figure VI-5-78c. A horizontal bottom is assumed. Provided the walls are sufficiently long, the wave height is estimated as

$$\frac{H_c}{H_i} = \frac{2\pi}{\beta} \tag{VI-5-193}$$

where H_c is the wave height in the corner, H_i is the incident wave height, and the angle β is expressed in radians. For $\beta = \pi$ the corner becomes a straight wall, and $H_c / H_i = 2$. However, as β becomes small, H_c increases to unreasonable values, and steepness-limited wave breaking will occur. Therefore, estimates of maximum waves at concave corners using Equation VI-5-193 should never be greater than the steepness-limited wave at that location. Goda stated the formula is also applicable to random waves. The wave height varies greatly along the walls due to interference between incident and reflected waves. For certain combinations of wall angle β and incident wave angle, the wave height at some position along the wave may be greater than at the corner apex (Goda 1985). Goda also described a more involved procedure for

estimating wave heights associated with directionally spread irregular waves. Perfectly reflecting vertical structures with concave bends (see Figure VI-5-78d) will have higher wave heights than straight walls with normal wave incidence. Wave height will depend on the radius of curvature, with greater heights expected for smaller radius bends. No simple formulas are available to estimate wave heights at concave bends; but a conservative estimate can be made by approximating the bend as a corner formed by two straight walls, and then applying Equation VI-5-193. Alternately, wave heights could be determined using an appropriate numerical model.

(b) Sloping structures with concave corners. There do not appear to be any simple, reliable engineering procedures for estimating wave height variations at sloping structures with concave corners or bends. For steep-sloped, impermeable structures, the previously described method for vertical walls will provide a conservative estimate. For milder slopes, the engineer should expect wave runup on the slope to be higher than would occur on straight structures because of the convergence of the incident wave crests. Generally, milder structure slopes, longer radii of curvature, and increased structure porosity will all contribute to a decrease in wave runup on the slope. Critical bends and corners should be tested in a physical model. If available, appropriate numerical models could also be used.

f. Uplift forces. The fluid induced force on a structure/object in the vertical (z-coordinate) direction is typically referred to as the "uplift" force (or "lift" force). The uplift force derives from various physical reasons depending on whether the structure is submerged or above water.

(1) Submerged or partially submerged structure.

(a) In the case of submerged or partially submerged structures in nonmoving fluids (i.e., a horizontal cylinderical object such as a timber cross-bracing in a pier or an outfall pipe), there is a buoyancy force which is equal to the volume of the fluid displaced by the structure/object times the specific weight of the fluid. This buoyancy force acts through the center of gravity of the displaced fluid volume in a vertically upward direction. The point through which the buoyant force acts is referred to as the center of buoyancy. The equation for this force component is given (Fox and McDonald 1985) as the integration over the volume of displaced fluid, i.e.,

$$F_B = \int_V (\rho_w g)\, dV \tag{VI-5-194}$$

where

F_B = buoyancy force (positive upwards)

ρ_w = density of water

g = acceleration of gravity

V = volume of displaced fluid

(b) For example, the buoyancy force acting on a fully submerged 1-m-diameter sphere is

$$F_B = \gamma_w \left(\frac{\pi D^3}{6}\right) = (10.1\ kN/m^3)\ (0.524\ m^3) = 5.29\ kN$$

where D is the sphere diameter and γ_w is the specific weight of salt water. The buoyancy force is directly countered by the gravitational force (weight) acting on the object. A net upward force occurs if the density of the submerged body is less than the water in which it is submerged.

(c) Additional vertically directed forces on the submerged or partially submerged solid body in the case of a moving fluid are due to the integration of the vertical component of pressure forces over the surface of the structure while neglecting elevation changes (Fox and McDonald 1985), i.e.,

$$F_L = -\int_S p_s \, (d\vec{A} \cdot \vec{n}_z) \tag{VI-5-195}$$

where

F_L = lift force (positive upwards)

p_s = pressure on solid body surface due to moving fluid (does not include hydrostatic pressure difference due to elevation changes over the surface

$d\vec{A}$ = differential surface area element of solid body with direction outward normal to surface

$\vec{n}_z$ = normal unit vectory in the positive z-direction (upwards)

(d) In the case of steady flow in the horizontal x-direction, an uplift force (often referred to as a lift force) develops when the flow field around the solid body has streamlines that are closer together above the body than below it (i.e., the "Bernoulli effect") creating a lower pressure above than below the solid body. This uplift force is analogous to the aerodynamic lift force that keeps an airplane aloft. Pipelines or outfalls lying on the seabed are examples of objects that could experience an uplift force due to the distortion of streamlines created by the protrusion of the pipeline/outfall in the flow field. Where the structure/object is only partially submerged and there is no flow over the top of the structure/object, the lift force will be acting vertically downward (i.e., negative lift force) due to the compression of streamlines (and hence lower pressure) under the structure/object.

(e) Uplift force computations on solid objects can be made via potential flow theory for simple geometry cases where there is low velocity flow (i.e., no flow separation). For the more typical design situation of turbulent flow over a solid body with flow separation, vortex shedding, and possibly a complex boundary imposed flow field, experimental laboratory measurements must be relied on to evaluate the uplift force. For steady flow situations, empirical uplift force coefficients (lift coefficients) are a function of the flow Reynold's number, "roughness" of the solid body, and the boundary imposed flow field around the body.

(f) When the fluid is unsteady, (e.g., oscillatory wave motion) the time-varying uplift force is estimated in the same manner as for steady flow only the computation becomes even more intractable due to the unsteady nature of the flow. In oscillatory flow over a solid body, vortices are shed with frequency and phase shifting that is dependent on the Keulegan-Carpenter number. For this situation uplift force computations and determination of empirical uplift force coefficients for the solid bodies in the flow are based on experimental laboratory measurements, often combined with numerical calculations.

(g) Oscillatory flow empirical uplift force coefficients are a function of the Keulegan-Carpenter number of the flow, the Reynolds number, "roughness of the structure/object, and boundary imposed flow field (e.g., Sarpkaya and Isaacson 1981). Where vortex shedding occurs at or near the natural frequency of the object

in the flow, a large amplitude dynamic response, called vortex-induced vibration, may occur, causing much larger forces than predicted by the static approach previously discussed.

(h) Uplift forces induced by both steady and oscillatory currents need to be considered where the characteristic width of structure to wavelength ratio is small (e.g., $D/L < 0.2$ in the case of circular cylinders of diameter, D). The equation for calculation of lift force in this situation is simplified as given in the following equation (Fox and McDonald 1985, Rouse 1950; and Sarpkaya and Isaacson 1981):

$$F_L = C_L A_n \gamma_w \left(\frac{u^2}{2g} \right) \tag{VI-5-196}$$

where

C_L = empirical lift coefficient

A_n = projected area of solid body normal to the flow direction

γ_w = specific weight of water

g = gravitational acceleration

u = magnitude of flow velocity (lift will be perpendicular to flow direction)

(i) In the case of both steady and oscillatory currents, the velocity components of the currents must be added vectorially to provide the velocity to utilize in the previous equation.

(j) When the size of the solid structure/object is large enough to modify the incident wave field by wave diffraction and/or wave scattering, Equation VI-5-196 cannot be used to determine lift forces. For large structures, transverse and inline forces must be computed using diffraction theory (Wiegel 1964, Sarpkaya and Isaacson 1981). Typically, diffraction theory is implemented using numerical models that determine the pressure on the solid body surface and then integrate over the surface to determine the total force.

(2) Emergent structures.

(a) In the situation where the structure/object is above water (i.e., a horizontal structural member) and subjected to oscillatory wave action, intermittant approximately vertical directed impact forces occur when the level of the water reaches the structure/object. The uplift force on a structure/object in this scenerio cannot be theoretically derived due to the complex fluid structure interaction. Instead, engineers must rely on laboratory measurements or empirical impact force (“slamming”) coefficients derived from laboratory testing. The uplift force for this situation is approximated as

$$F_U = C_U A_z \gamma_w \left(\frac{w^2}{2g} \right) \tag{VI-5-197}$$

where

C_U = laboratory derived slamming coefficient

A_z = projected area of solid body in the horizontal plane

w = vertical component of flow velocity at level of object

(b) A slamming coefficient approach to calculation of this type of uplift force is utilized primarily for slender members (for which the Morrison equation is utilized for the inline force computation). The wave theory utilized to calculate the vertical velocity at the level of the structure may depend on what level of approximation is desired and/or whether a monochromatic wave theory or irregular (linear) wave theory is utilized for the computation. A particular problem in evaluation of Equation VI-5-197 is estimating the velocity field at the structure. For even the most simple calculations an assumption that the structure does not influence the wave flow field must be made. Most uplift impact (slamming) force coefficients are derived from experimental laboratory measurements. Sarpkaya and Isaacson (1981) discussed experimental results for rigidly mounted horizontal circular cylinders subject to slamming forces, and they noted laboratory measured slamming force coefficients (C_U) ranging from 4.1 to 6.4.

(c) Typical coastal structures on which uplift forces may need to be calculated that do not fit into any of the previous catagories are caisson or monolithic concrete type breakwaters. These structures have additional complications with regard to calculation of uplift forces because they are situated on permeable foundations of rock or sand making theoretical calculations for the uplift forces very difficult. In this situation, empirical or semiempirical formula (based on laboratory testing) are utilized to provide preliminary design calculations. Typically, design conditions will not be the same as tested in past laboratory tests; therefore, uplift forces may need to be determined by testing the design in a physical model.

(d) Goda (1985) provided empirical formulae with which to make simple (uplift) dynamic component wave force calculations on the base of composite foundation vertical caisson (or monolithic concrete) breakwaters. The dynamic component of uplift force is assumed to be triangular over the base of the structure. The empirical formulae utilized are based on a limited number of laboratory tests and should only be utilized for preliminary calculations. Variables not in the empirical guidance but very important to the pressure distribution under the structure base are foundation permeability and structure width. High permeability and narrow structure widths could lead to uplift forces considerably in excess of Goda's (1985) empirical guidance.

(e) Uplift forces on docks and piers are also of concern to coastal engineers although limited information exists for the computation of forces on these types of structures. When the wave crest height exceeds the underside level of the pier or dock, the structure will be subjected to uplift forces in both transverse directions. The computation of uplift force in this situation is difficult due to the modification of the flow field by the structure and the nonlinear boundary conditions at the water surface that must be accommodated. Typically, laboratory experiments augmented by numerical modeling must be utilized to evaluate these types of uplift forces. French (1969) measured (in a laboratory experiment) transverse (positive and negative uplift) forces due to a solitary wave moving perpendicular to a pier and found that negative uplift forces often exceeded the positive uplift forces for the situations addressed. Lee and Lai (1986) utilized a numerical model to calculate wave uplift forces on a pier; and they noted that under certain conditions of bottom slope and solitary wave height to water depth combinations, positive uplift pressures can be larger than those calculated utilizing hydrostatic pressure for the given depth of immersion. In the situation where a vertical wall abuts the platform and wave reflection takes place (e.g., a dock structure), the positive uplift appears to be significantly increased while the negative uplift is reduced compared to the pier (i.e., no wave reflection) case.

(f) Bea et al. (1999) examined wave forces on the decks of offshore platforms in the Gulf of Mexico. They summarized results from a performance study of platforms that had been subjected to hurricane wave loadings on their lower decks. Modification to guidelines of the American petroleum industry were discussed

and validated. Bea et al. provides up-to-date references related to wave forces on decks of offshore platforms that may be useful for similar calculations for docks and piers.

VI-5-5. Foundation Loads

a. Introduction.

(1) This section assumes the reader has a general knowledge about soil mechanics and foundation design because only limited basic information is given with emphasis on coastal structure foundations. The soil parameter values and empirical expressions given in this section are sutiable for feasibility studies and preliminary design calculations prior to any direct soil parameter measurements being performed in the field or laboratory. The same applies for final design calculations in small projects where specific geotechnical investigations cannot be performed. In general, calculations for detailed design should be based on specific analysis of the local soil mechanics conditions. Moreover, the most relevant and accurate methods of analysis should be applied.

(2) The main objective of this section is to present two important geotechnical aspects related to the design and geotechnical stability of breakwaters, dikes and seawalls:

(a) Assurance of safety against failure in soils contained within structures, rubble-mound structures, and in foundation soils.

(b) Assurance of limited (acceptable) deformations in soils contained within structures, rubble-mound structures, and in the foundation soil during structure lifetime.

(3) Related to these two aspects are the geotechnical failure modes illustrated in Part VI-2-4:

(a) Slip surface and zone failures, causing displacement of the structure and/or the subsoil.

For rubble-mound structures and dikes see Figures VI-2-25, VI-2-41, and VI-2-51.
For monolithic structures see Figures VI-2-54, VI-2-55, VI-2-64, and VI-2-66.
For tied wall structures see Figures VI-2-69, VI-2-70, VI-2-71, and VI-2-72.

(b) Excess settlement due to consolidation of subsoil and rubble foundation, causing lowering of the crest of the structure as shown in Figures VI-2-42 and VI-2-53.

(4) Slip surface and zone failures are the result of insufficient soil bearing capacity caused by unforseen external loadings and/or degradation of soil strength. Such failures generally lead to pronounced settlement and damage or collapse of the structure. Potential for such failure makes it important to implement proper safety factors in the design.

(5) Excess settlement due to consolidation is caused by misjudgment of subsoil characteristics and, in the case of larger rubble-mound structures, the core materials. If evenly distributed, the settlement lowers the crest level, which causes an increase in overtopping and might reduce structure functionality. Differential settlements can cause damage to the structure itself, for example breakage of concrete superstructures, cracking of long concrete caissons, or creating weaknesses in the armor layer.

(6) A significant difference between geotechnical stability of coastal structures and common land based structures is the presence of wave action on the structure and its foundation. Another difference is the wave-induced pore pressure variation which will be present in wave exposed porous structures and seabed soils. The wave load introduces stress variations in the soils that can lead to degradation in soil strength due to pore

pressure build-up. The designer has to show that at any stage throughout the structure lifetime the soil stresses should not exceed the soil strength. This calls for prediction of short and long-term stress and strength development in the soils. Distinction is made between cases with gradually varying wave forces caused by nonbreaking waves and cases with short-duration impulsive wave forces due to waves breaking directly on the structure. The first case is referred to as cyclic loading, the second case is dynamic loading, which includes dynamic amplication.

(7) This section is organized into the following sections containing basic information about the soil and related hydromechanic processes:

Part/Chapter/Section Heading	Section Topic
VI-5-5-b. Soil and Rock Properties	Basic definitions and related typical parameter values. Deformation characteristics of soils are discussed as well.
VI-5-5-c. Strength Parameters	Soil parameter definitions and typical soil strength values.
VI-5-5-d. Hydraulic Gradients and Flow Forces in Soils.	Includes the Forchheimer equation and estimates on wave induced internal set-up and pore pressure gradients in breakwater cores.
VI-5-5-e. Cyclic loading of soils.	Discussion of drainage conditions, transmission of wave loads to the foundation soil, and degradation of soil strength and generation of residual pore pressure when exposed to wave induced cyclic loading.
VI-5-5-f. Dynamic Loading of Soils Under Monolithic Structures.	Evaluation of dynamic amplification of foundation forces and deformations caused by impulsive wave forces.
VI-5-5-g. Slip Surface and Zone Failures.	Stability of slopes, bearing capacity of quarry rock foundations and subsoils. Stability of soil retaining structures is not discussed.
VI-5-5-h. Settlement.	Short discussion of immediate and consolidation settlement.

b. Soil and rock properties.

(1) Grain sizes. Table VI-5-65 gives the fractional limits according to International Standards Organization (IS), and Comité Européen de Normalisation (CEN).

Table VI-5-65
Fractional Limits of Grain Sizes According to ISO/CEN

Main Group	Grain Size, mm	Sub-Groups	Grain Size, mm
Boulders	> 200		
Cobbles	60 - 200		
Gravel	2 - 60	Coarse Medium Fine	20 - 60 6 - 20 2 - 6
Sand	0.06 - 2.0	Coarse Medium Fine	0.6 - 2.0 0.2 - 0.6 0.06 - 0.2
Silt	0.002 - 0.06	Coarse Medium Fine	0.02 - 0.06 0.006 - 0.02 0.002 - 0.006
Clay	< 0.002		

(2) Bulk density. The bulk density is defined by the relation

$$\rho = m/V \tag{VI-5-198}$$

where m is total mass and V is total volume. Typical bulk densities are given in Table VI-5-66.

Table VI-5-66
Typical Bulk Density Values

Soil Type	Bulk Density, ρ (tonne/m^3)	
	Water-Saturated	Above Water Table
Peat	1.0 - 1.1	(often water-saturated)
Dy and gyttja	1.2 - 1.4	(often water-saturated)
Clay and silt	1.4 - 2.0	(often water-saturated)
Sand and gravel	2.0 - 2.3	1.6 - 2.0
Till	2.1 - 2.4	1.8 - 2.3
Rock fill	1.9 - 2.2	1.4 - 1.9

The unit weight is given by

$$\gamma = \rho g = \rho(9.81\ kN/m^3)$$

(3) Volume of voids. The volume of voids is either expressed in terms of

$$\text{porosity}\quad n = V_p/V \qquad \text{or} \qquad \text{void ratio}\quad e = V_p/V_s \tag{VI-5-199}$$

where V is the total volume and V_p and V_s are the volume of voids and solids, respectively.

(a) The porosity of coarse-grained soils is strongly dependent on the grain size distribution, the shape of the grains, and the compaction. Typical values of e and n for granular soils are given in Table VI-5-67.

Table VI-5-67
Typical values of void ratio *e* and porosity *n* for granular soils.

Material	Void Ratio		Porosity	
	e_{min}	e_{max}	n_{min}	n_{max}
Uniform spheres	0.35	0.92	0.26	0.48
Uniform sand	0.40	1.00	0.29	0.50
Sand	0.50	0.80	0.33	0.44
Silty sand	0.30	0.90	0.23	0.47
Uniform silt	0.40	1.1	0.29	0.52

(b) For cohesive soils the range of e (and n) is much larger than for granular soils. For clays e can range between 0.2 and 25.

(4) Relative density. The relative density is defined as

$$D_r = \frac{e_{\max} - e}{e_{\max} - e_{\min}} 100\% \quad \text{(VI-5-200)}$$

where

e_{min} = void ratio of soil in most dense condition

e_{max} = void ratio of soil in loosest condition

e = in-place void ratio

Table VI-5-68 provides a density characterization of granular soils on the basis of D_r.

Table VI-5-68
Density Characterization of Granular Soils

Relative Density D_r (percent)	Descriptive Term
0 - 15	very loose
15 - 35	loose
35 - 65	medium
65 - 85	dense
85 - 100	very dense

(5) Plasticity index. The plasticity index I_p relates to cohesive soils and indicates the magnitude of water content range over which the soil remains plastic. The plasticity index is given by

$$I_p = w_l - w_p \quad \text{(VI-5-201)}$$

where w is the water content, i.e., the ratio of weight of water to the weight of solids in a soil element, and subscripts l and p refer to liquid and plastic limits, respectively.

(6) Total and effective stresses. The total stresses on a section through a soil element can be decomposed into a normal stress σ, and a shear stress τ as illustrated by Figure VI-5-80.

(a) Because the soil is a three-phase medium consisting of solids and voids filled with water and/or gas it is seen that the total normal force is the sum of the contact forces between the grains and the pore pressure, u. In terms of stresses (force per unit area) we define

$$\sigma = \sigma' + u \quad \text{(VI-5-202)}$$

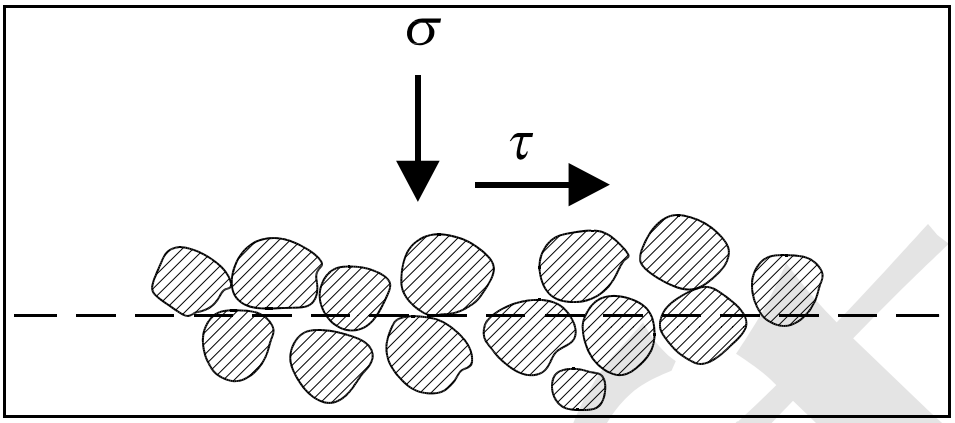

Figure VI-5-80. Total stresses in a soil element

where σ is total stress, σ' is effective stress and u the pore pressure. Because of the small area of the contact points it can be assumed that u is acting over the whole unit area of the section.

(b) Water and gas cannot resist shear stress so the total shear stress, τ, is set equal to the effective shear stress, τ', i.e., the stress carried by the grains,

$$\tau = \tau' \tag{VI-5-203}$$

(c) It follows from Equation VI-5-202 and Equation VI-5-203 that the ability of the soil to resist failure depends on the strength of the grain skeleton, which in turn depends on the effective stresses. This means that under constant normal stress, an increase in the pore pressure will lower the soil strength. For coastal structures changes in pore pressure are normally caused by changes in seawater level and by wave action.

(7) Geostatic stress. The geostatic stress is the stress caused by the weight of the soil when the ground surface is horizontal and the nature of the soil has only slight variation in the horizontal directions. For homogeneous soil the vertical geostatic stress is given by

$$\begin{aligned} \sigma_v &= z\,\gamma \quad , \quad \text{based on total stress} \\ \sigma_v' &= z\,\gamma' \quad , \quad \text{based on effective stress} \end{aligned} \tag{VI-5-204}$$

where z is the depth, and γ and γ' are the total and the submerged unit weights of the soil, respectively. In other words, σ_v and σ'_v vary linearly with depth.

(8) Stresses within soil deposits. The coefficient of lateral stress, K, is the ratio of horizontal to vertical effective stress, i.e.,

$$K = \frac{\sigma_h - u}{\sigma_v - u} = \frac{\sigma_h'}{\sigma_v'} \tag{VI-5-205}$$

K_o is the coefficient of lateral stress at rest. For sand deposits created by sedimentation values of K_o are typically in the range 0.4 - 0.5.

(9) Stresses due to externally applied surface loads. Although soil is an elastic plastic material, the theory of elasticity is often used to compute stresses from externally applied loads. (Examples are settlement calculations and verification of deformation amplification by dynamic loading.) Furthermore, most of the useful solutions from this theory assume that the soil is homogeneous and isotropic. Soil seldom, if ever, fulfills these assumptions. However, the engineer has little choice but to use the results from the elasticity theory together with engineering judgement. The assumption of elastic behavior is rather good if the applied stresses are low compared to stresses at failure. Diagrams for estimation of stresses induced by uniform loading on circular areas, rectangular areas and strip areas are given in most geotechnical textbooks, see for example Hansbo (1994) and Lambe and Whitman (1979).

(10) Overconsolidation ratio. A soil element that is at equilibrium under the maximum stress it has ever experienced is normally consolidated, whereas a soil at equilibrium under a stress less than the maximum stress to which it was once consolidated is termed overconsolidated. The ratio between the maximum past pressure and the actual pressure is the overconsolidation ratio (OCR). A value of OCR = 1 corresponds to normally consolidated clay where the soil tries to reduce volume (contract) when loaded further, whereas $OCR > 1$ corresponds to overconsolidated clay which tends to increase volume (dilate) under applied loads.

(11) Deformation moduli. Although soils generally exhibit plastic deformations during failure, the theory of elasticity is still widely used (for example relating soil response to dynamic loadings and stress distributions under static loads). Assuming soil behaves as an elastic material, the deformation characteristics can be expressed in terms of the moduli given in Table VI-5-69.

(a) Typical values of Poisson's ratio, v, for conditions after initial loading are given in Table VI-5-70. Exact determination of v is of less importance, because practical engineering solutions are generally not sensitive to v.

(b) The nonlinear deformation characteristics of soil makes it necessary to use secant values of the deformation moduli, as shown in Figure VI-5-81 which illustrates results from shear and compression tests. Uniaxial and confined compression tests exhibit a similar reaction. Secant values relate to stress levels being some fraction of the maximum (failure) stress. Distinction is made between initial loading where relative large deformations occur, and repeated (cyclic) loading where permanent deformations decrease and eventually disappear.

(c) Young modulus for sand varies with the void ratio, strength and shape of the grains, the stress history and the loading rate. Table VI-5-71 gives some example values of the secant Young's modulus corresponding to quasi-static loadings of 50 percent of the peak deviator stress and 101.3 kN/m^2 (1 atm) confining stress (Lambe and Whitman 1979).

(d) Young's modulus for clay varies with stress level, level of consolidation, and rate of strain. Table VI-5-72 provides typical values given by Richardson and Whitman (1964) corresponding to quasi-static loadings.

(e) It follows from Figure VI-5-81 that the deformation moduli depend on the strain level and the type of loading.

(f) Typical values of shear modulus G, bulk modulus K and oedometer modulus M for quartz sand is given in Table VI-5-73 corresponding to initial loading ($\sigma' \leq 300$ kN/m^2) and subsequent unloading and reloading (mean $\sigma' = 100$ kN/m^2).

Table VI-5-69
Deformation Moduli for Elastic Material

Young's modulus

$$E = \frac{\sigma_1}{\varepsilon_1}$$

Poisson' ratio

$$\nu = -\frac{\varepsilon_2}{\varepsilon_1}$$

Shear modulus

$$G = \frac{\tau}{\gamma} = \frac{E}{2(1+\nu)}$$

Bulk modulus

$$K = \frac{\sigma}{\varepsilon_{vol}} = \frac{2G(1+\nu)}{3(1-2\nu)}$$

ε_{vol} is volumetric strain, i.e. the relative change in volume V

Constrained modulus
(Oedometer modulus)

$$M = \frac{\sigma_1}{\varepsilon_1} = \frac{2G(1-\nu)}{1-2\nu}$$

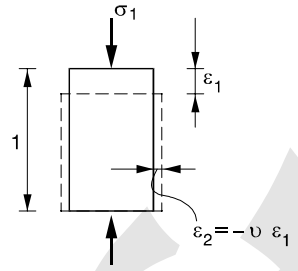

Uniaxial loading of elastic cylinder

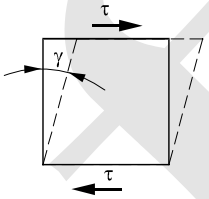

Shear applied to elastic cube

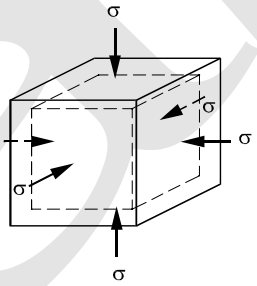

Isotropic compression of elastic cube

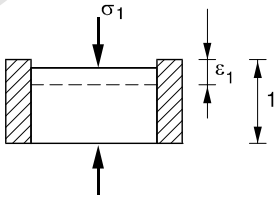

Confined compression

Table VI-5-70
Typical Values of Poisson's Ratio, *v*

Soil	v
Dry Sand	0.35
Partially saturated sand and clay	0.4
Saturated sand and clay	0.5

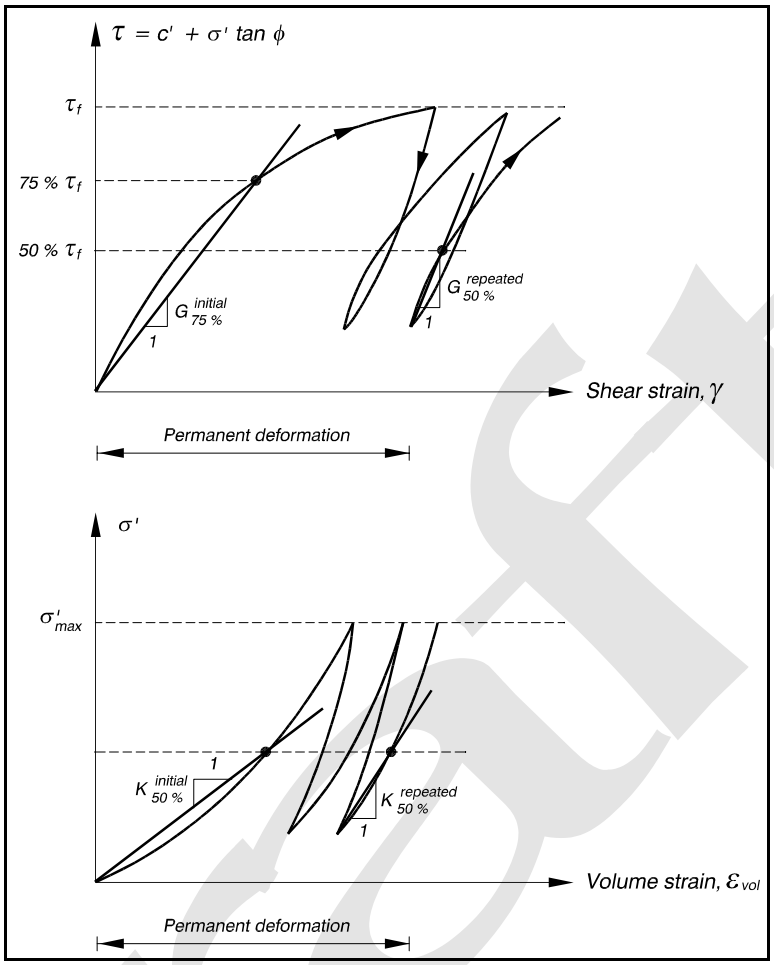

Figure VI-5-81. Illustration of shear modulus *G* and bulk modulus *K* for granular soils exposed to initial and repeated (cyclic) loadings

Table VI-5-71
Example Values of Secant Young's Modulus *E* in MN/m^2 for Sand

Material	Loading	Packing Density	
		Loose	Dense
Angular	Initial	15	35
	Repeated	120	200
Rounded	Initial	50	100
	Repeated	190	500

Table VI-5-72
Typical Values of Secant Young's Modulus, *E*, for Clay

Level of Consolidation	Strain Rate	E/σ Safety Level 3[1]	E/σ Safety Level 1.5
Normal	1 percent / 1 min.	250	160
	1 percent / 500 min.	120	60
Over	1 percent / 1 min.	450	200
	1 percent / 500 min.	250	140

[1] Deviator stress equal to 33 percent of peak deviator stress.

Table VI-5-73
Typical Secant Values of Deformation-Moduli *G*, *K* and *M* for Quasi-Static Loaded Quartz Sand (Centre for Civil Engineering Research and Codes (CUR) 1995)

Parameter	Initial Loading	Repeated Loading
G (MN/m^2)	4 - 40	20 - 400
K (MN/m^2)	10 - 100	50 - 1000
M (MN/m^2)	15 - 150	80 - 500

Note: Higher values valid for dense sand, lower values valid for very loose sand.

(g) The shear modulus G is independent of drained or undrained conditions, and the value of G for clays is dependent on the type of clay (plasticity index), the type of loading, the stress level, and the *OCR*. Figure VI-5-82 shows the range of G over the static undrained shear strength, c_u, as a function of the shear strain for some saturated clays (not further characterized).

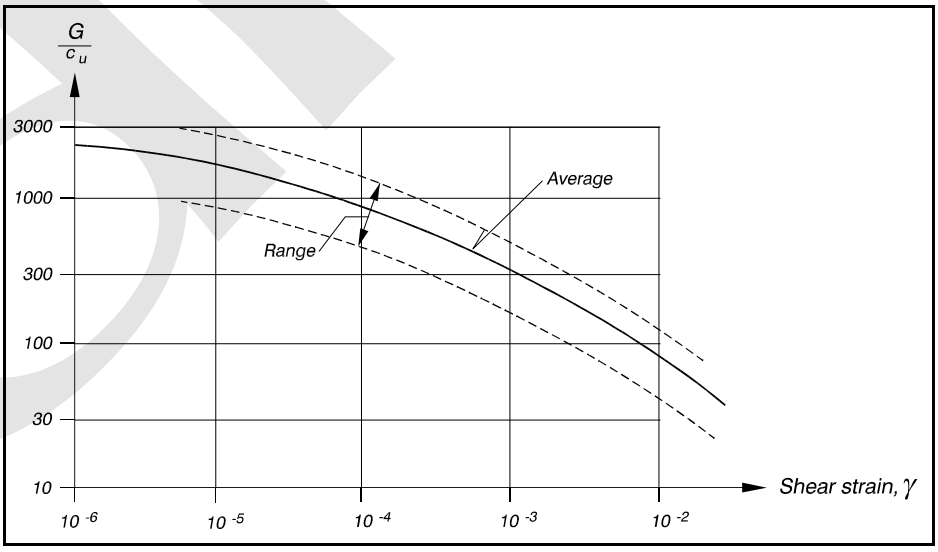

Figure VI-5-82. In-situ secant values of shear modulus *G* for quasi static loaded saturated clays (after Seed and Idriss 1970)

(h) The significant influence of *OCR* and cyclic loading on *G* is shown in Figure VI-5-83 which presents results for Norwegian Drammen clay with plasticity index I_p of 27 percent and a clay content of 45-55 percent. These results were based on stress controlled DSS tests and resonant column tests. In Figure VI-5-83 the parameter σ_u^{DSS} is the undrained static DSS shear strength for two hours of loading to failure. The stress τ_{cy} is the shear stress amplitude in the symmetric cyclic loading. *N* is number of load cycles.

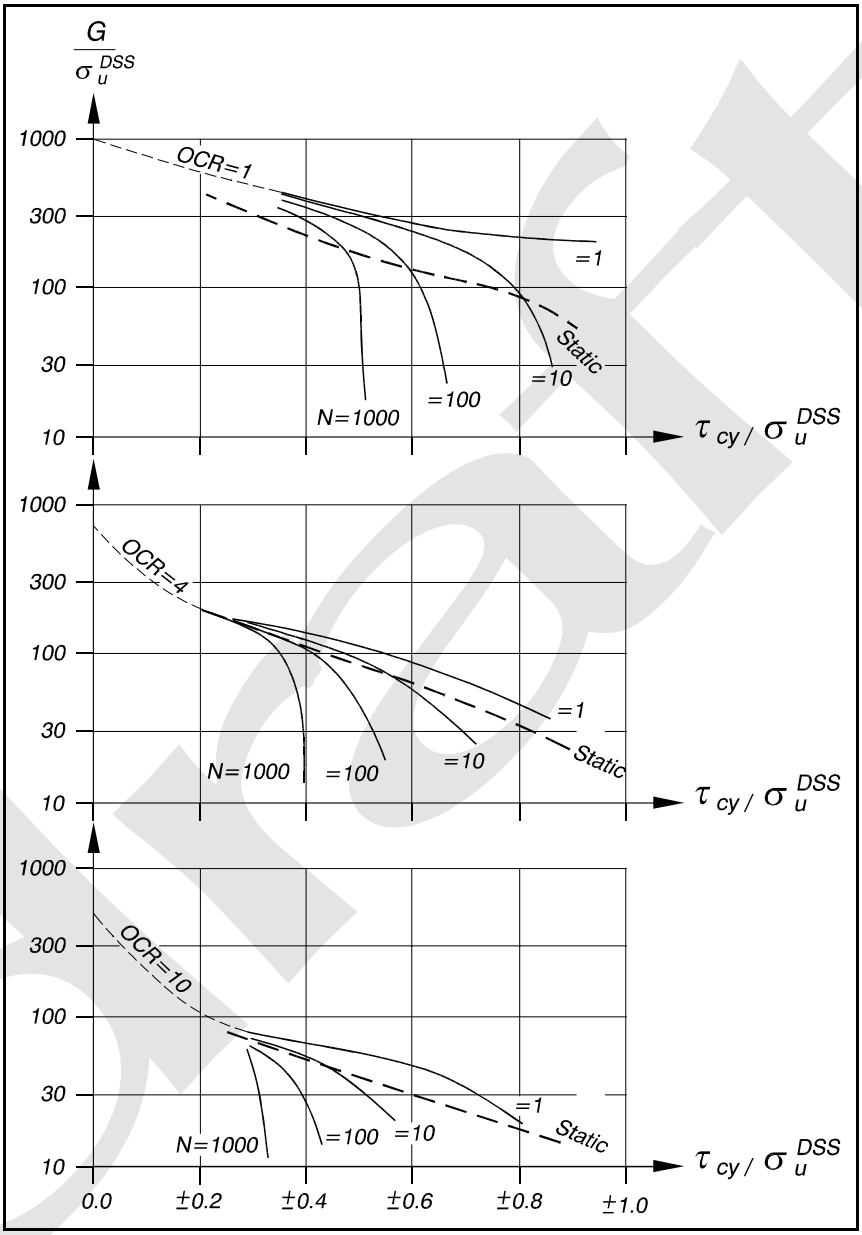

Figure VI-5-83. Static and secant cyclic shear modulus, *G*, for Drammen clay (Andersen, Kleven, and Heien 1988)

(i) The shear modulus *G* is an important parameter in soil response to dynamic loadings that might be caused by waves and earthquakes. In quasi-static loading tests, such as simple shear and triaxial tests, the lower limit for strain measurements is approximately 10^{-3}, whereas in bender element and resonant column tests strains down to 10^{-6} can be recorded. Thus in practice, the maximum value G_{max} which can be identified corresponds to a shear strain of approximately 10^{-6}. Formulae for G_{max} are given as follows:

- Sand (Hardin and Black 1968)

$$G_{\max} = \begin{cases} \dfrac{6908(2.17-e)^2}{1+e}\sqrt{p'} & \text{round-grained} \\ \dfrac{3230(2.97-e)^2}{1+e}\sqrt{p'} & \text{angular-grained} \end{cases} \quad \text{(VI-5-206)}$$

- Gravel (Seed et al. 1986). They found G_{max} values approximately 2.5 times larger than for sand.

- Clay (Hardin and Drnevich 1972)

$$G_{\max} = \frac{3230(2.97-e)^2}{1+e}\,(OCR)^K\,\sqrt{p'} \quad \text{(VI-5-207)}$$

where

e = void ratio

p' = mean effective stress, $1/3(\sigma_1' + \sigma_2' + \sigma_3')$ to be inserted in kN/m^2 to obtain G_{max} in kN/m^2

OCR = overconsolidation ratio

K = constant dependent on the plasticity index

Plasticity Index (percent)	0	20	40	60	80	≥ 100
K	0	0.18	0.30	0.41	0.48	0.50

Hardin (1978) proposed for both granular and cohesive soils that

$$G_{\max} = \frac{625}{0.3+0.7e^2}\,(OCR)^K\,\sqrt{p_a\,p'} \quad \text{(VI-5-208)}$$

where p_a is atmospheric pressure (101.3 kN/m^2). The ratio between G and G_{max} as function of the shear strain for sand and gravel is given in Figure VI-5-84.

(12) Damping ratio. The damping ratio D signifies the decrease in the displacement amplitude z_n of the oscillations and is defined by

$$D = \frac{\delta}{2\pi} = \frac{1}{2\pi}\ln\left(\frac{z_n}{z_n+1}\right) \quad \text{(VI-5-209)}$$

where δ is the logarithmic decrement. Figure VI-5-85 shows damping ratios for sands and clays.

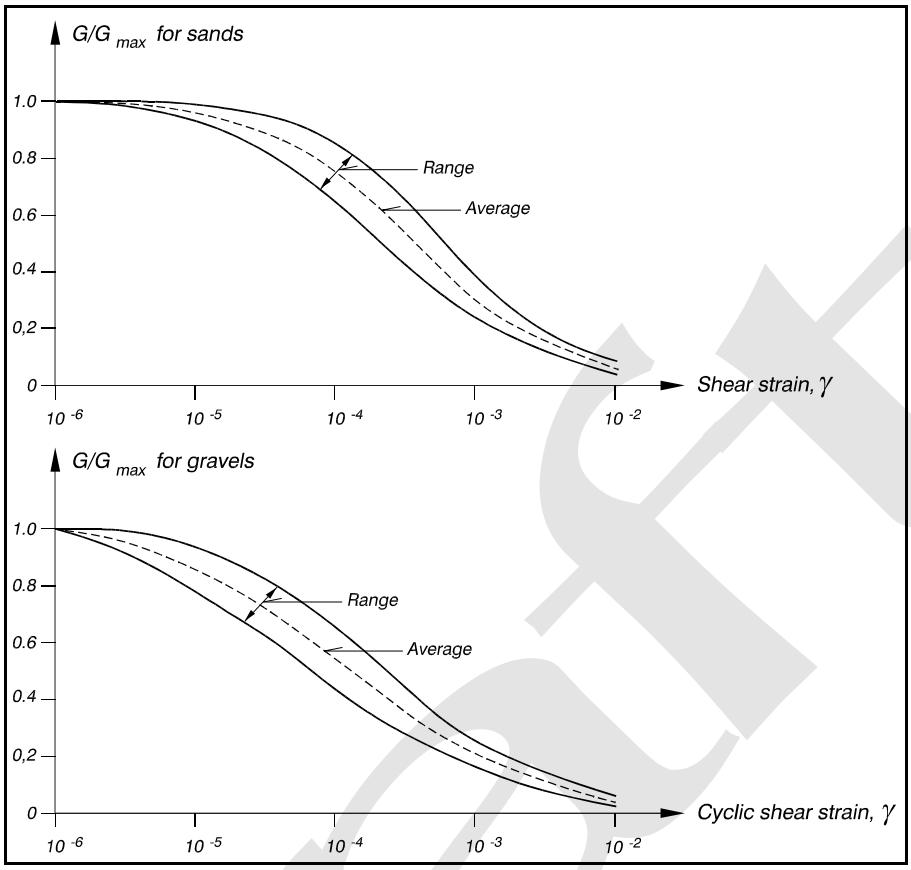

Figure VI-5-84. Values of G/G_{max} for sands and gravels (after Seed et al. 1986)

c. Strength parameters.

(1) Mohr-Coulomb failure criterion.

(a) The strength parameters of soil and rock fill constitute the basis for analysis of soil bearing capacity and wall pressures. Failure occurs when shear stresses reach an upper limit represented by the envelope to the Mohr failure circles, as shown in Figure VI-5-86.

(b) The Mohr envelope is generally curved for drained conditions. Figure VI-5-87 shows two commonly applied straight-line approximations to curved envelopes found from drained triaxial tests. Figure VI-5-87 demonstrates that the straight-line approximation is good only in the vicinity of the σ'_f-value for which the tangent to the circle is constructed. The approximation in Figure VI-5-87a is given by the Mohr-Coulomb equation

$$\tau_f = c' + \sigma'_f \tan \varphi'_t \qquad \text{(VI-5-210)}$$

where c' is the cohesion intercept, φ_t' is the effective tangent angle of friction, and σ_f' is the effective stress at failure as specified by Equation VI-5-204.

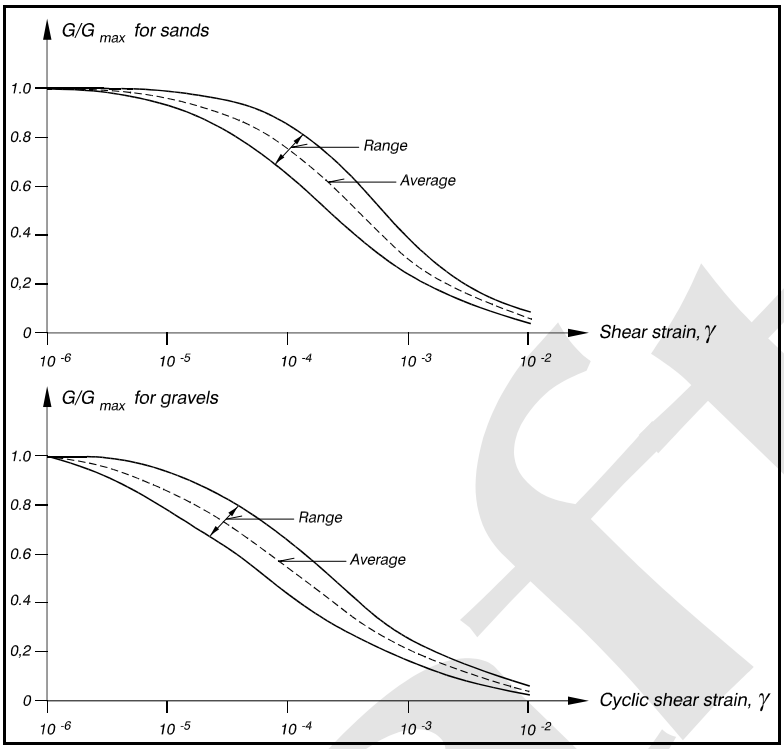

Figure VI-5-85. Damping ratios for sands and saturated clays (Seed and Idriss 1970)

(2) Noncohesive soils.

(a) The failure criterion approximation shown in Figure VI-5-87b corresponding to the equation

$$\tau_f = \sigma_f' \tan \varphi_s' \tag{VI-5-211}$$

where φ_s' is the effective secant angle of friction, has been applied to granular soils ever since the early studies by Coulomb. The equation is accurate only for relatively small values of σ_f'. However, for well graded quartz sand the limit for reasonable accuracy may be as high as 1,000 kN/m^2. In general the equation should be applied only to a limited stress range around the σ_f' value corresponding to φ_s'. Otherwise, for very high stress ranges the strength of a granular soil or rockfill can only be satisfactorily represented by Equation VI-5-210, or a curved Mohr envelope. Another way to represent the nonlinear strength relation is to treat $\tan \varphi'$ as a variable that depends on the confining pressure as indicated in Figure VI-5-87, which shows that φ' is a function of the actual effective stress level.

(b) The angle of friction φ' in granular materials depends on the grain-size distribution, size and shape of the grains, and on the porosity. Well graded materials exhibit higher friction than uniformly graded materials. Sharp edged angular grains give higher friction than rounded grains, and the friction angle will be higher in densely packed than it is in loose soils.

(c) Typical angles of friction for granular soils like quartz sand and quarried granite rock fill are given in Table VI-5-74 and Figure VI-5-88.

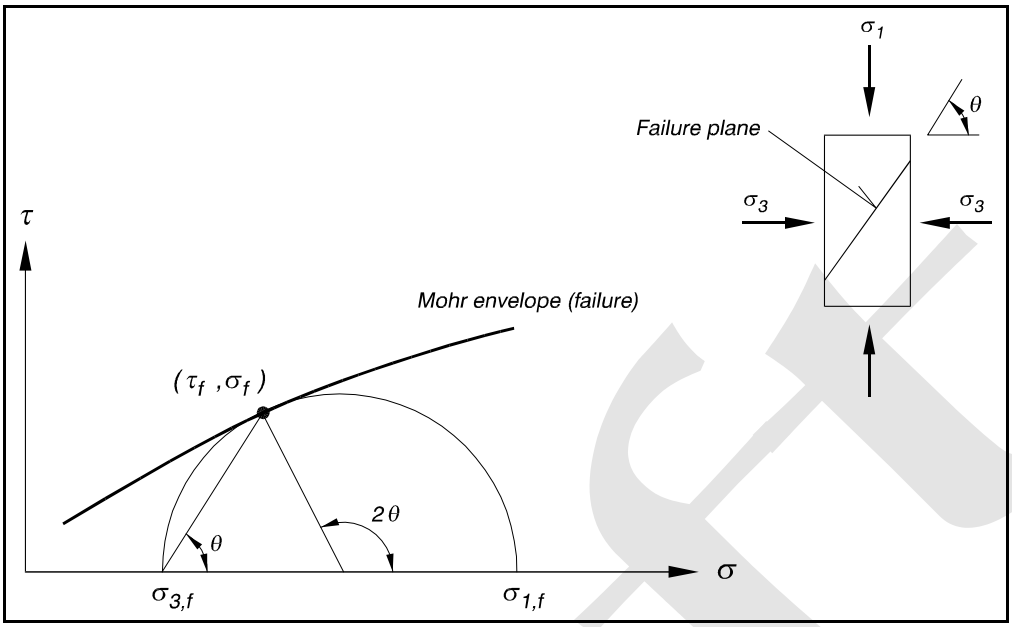

Figure VI-5-86. Mohr envelope for stresses of failure

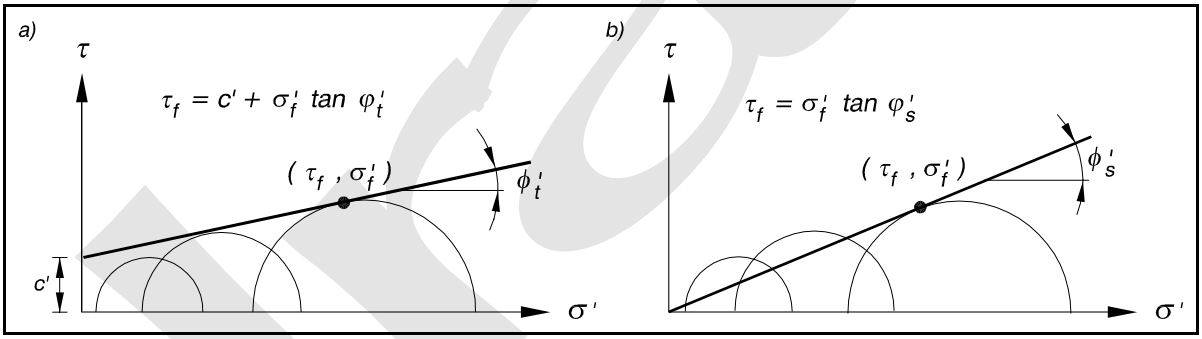

Figure VI-5-87. Illustration of straight-line approximations to curved Mohr envelopes corresponding to drained conditions: (a) Tangent formulation, (b) Secant formulation

Table VI-5-74
Typical Values of Triaxial Test Friction Angle φ_s for Quartz Sand

Relative Density	Friction Angle from Triaxal Tests φ_s (degrees)
Very loose	-
Loose	29 - 35
Medium	33 - 38
Dense	37 - 43
Very dense	-

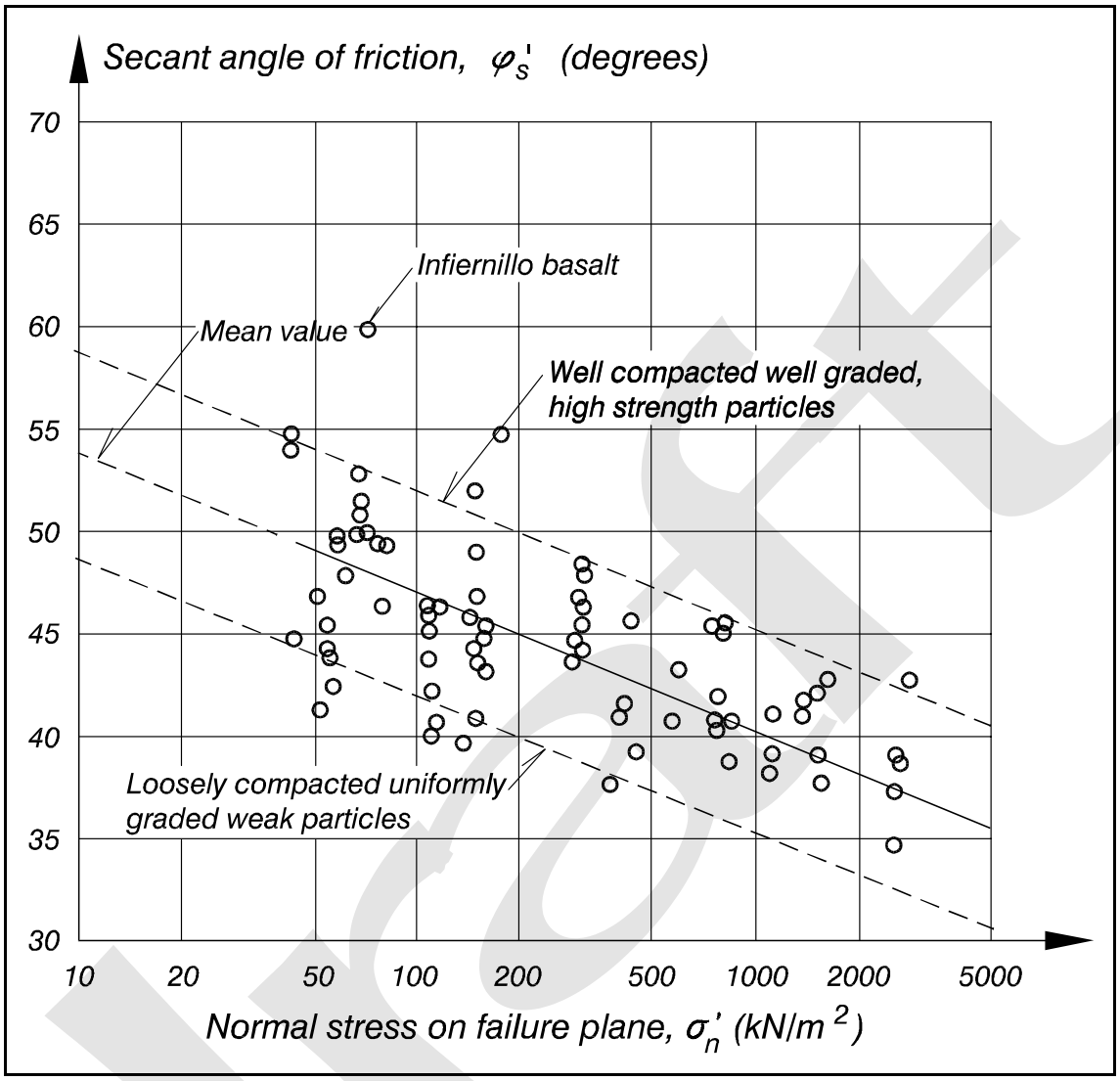

Figure VI-5-88. Angle of friction in rock fill of different grading and porosity with maximum diameter in the range 70-200 mm (After Leps 1970 and Kjærnsli, Valstad, and Høeg 1992)

(d) Steenfelt and Foged (1994) reported secant angles of friction $\varphi_s' = 45^o - 62.2^o$ at normal stress on failure plane $\sigma_n' = 77 - 273$ kN/m^2 for Hyperite crushed stone of mass density 3.1 tonne/m^3, $d_{50} = 15 - 16$ mm and $d_{max} = 64$ mm. This compares well with the Infiernillo basalt data in Figure VI-5-88.

(3) Dilatancy.

(a) Shearing of frictional soils under drained conditions generally involves volume changes in terms of dilation or contraction. A crude visualization of dilatancy in plane strain is shown in Figure VI-5-89.

(b) The volume changes associated with stress as it increases toward maximum strength (see φ_s' in Equation VI-5-211) depend on the effective stress level and the initial density, which is given by porosity n or void ratio e. The volume changes are quantified by the angle of dilation, ψ, defined by

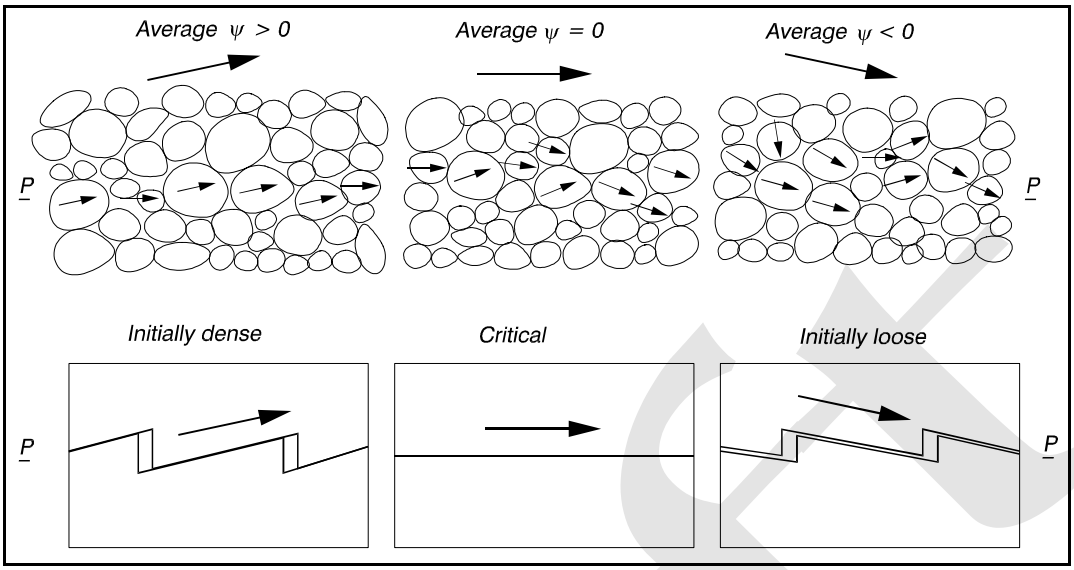

Figure VI-5-89. Crude visualization of dilatancy and angle of dilation ψ (Bolton 1979)

$$\sin\psi = -\frac{\dot{\varepsilon}_1 + \dot{\varepsilon}_3}{\dot{\varepsilon}_1 - \dot{\varepsilon}_3} = \frac{\dot{\varepsilon}_{vol}}{\dot{\varepsilon}_{vol} - 2\dot{\varepsilon}_1} \tag{VI-5-212}$$

where $\dot{\varepsilon}_1$, and $\dot{\varepsilon}_3$ are strain rates in principal stress directions 1 and 3, and $\dot{\varepsilon}_{vol}$ is the volume strain rate. The strain rates can be found from triaxial tests.

(c) The angle of friction corresponding to the critical (also called ultimate) condition where the soil strains without volume changes (see Figure VI-5-89) is denoted the critical angle of friction, φ'_{crit}. The parameter φ'_{crit} appears to be a material constant because it depends on the mineralogy, grading and shape of the grains for the soil in question, but seems independent on the relative density or porosity. Typical values of φ'_{crit} are given in Table VI-5-75.

(d) An average value of φ'_{crit} for sand is 32 deg. For quarried rockfill a somewhat higher value is found. Steenfelt (1992) stated that a simple bench test for φ'_{crit}, offering an accuracy of about 1°, is the angle of repose of a loosely tipped heap of dry material subjected to excavation at the foot.

The contribution of dilation to the strength of the material is suggested as follows by Bolton (1986)

$$\varphi'_{max} - \varphi'_{crit} = 0.8\ \psi_{max} = \begin{cases} 5^o I_r & plane\ strain \\ 3^o I_r & triaxial\ strain \end{cases} \tag{VI-5-213}$$

where

$$I_R = D_r(A - \ln p') - 1 \tag{VI-5-214}$$

and

Table VI-5-75
Critical Value of Angle of Friction, φ'_{crit} (Steenfelt 1992)

Material	d_{50} (mm)	d_{max} (mm)	φ'_{crit} (deg)
Quartz sand, dry and saturated	0.17	-	27.5 - 32
	0.24	-	29 - 33.3
	0.52 - 0.55	-	33.5
	0.88	-	31.9
Rock fill, quarried granitic gneiss	-	9.5 - 80	39.1

$\varphi'_{max} = \varphi'_s$ for triaxial strain, as given by Equation VI-5-211

D_r = relative density

p' = mean effective stress, $1/3(\sigma_1' + \sigma_2' + \sigma_3')$ in kN/m

A = material constant, 10 for quartz and feldspar, and 8 for limestone

Typical values of ψ_{max} for quartz granular materials are given in Table VI-5-76.

Table VI-5-76
Typical Values of ψ_{max} for Quartz Sand and Quarried Granitic Gneiss

Relative Density	Angle of Dilation, ψ_{max} (deg)
Loose	-2 to +3
Medium	+3 to +8
Dense	+8 to +13

(4) Cohesive soils.

(a) The shear strength of cohesive soils like clay and organic mineral soils is due to both friction (between coarser grains and between aggregates formed by clay particles) and cohesion within the material (sorption forces). The shear strength of clay normally refers to the static shear strength from undrained strain controlled tests with a monotonic load increase lasting 1-3 hours to failure. This so-called undrained shear strength, c_u and the related failure envelope are illustrated in Figure VI-5-90.

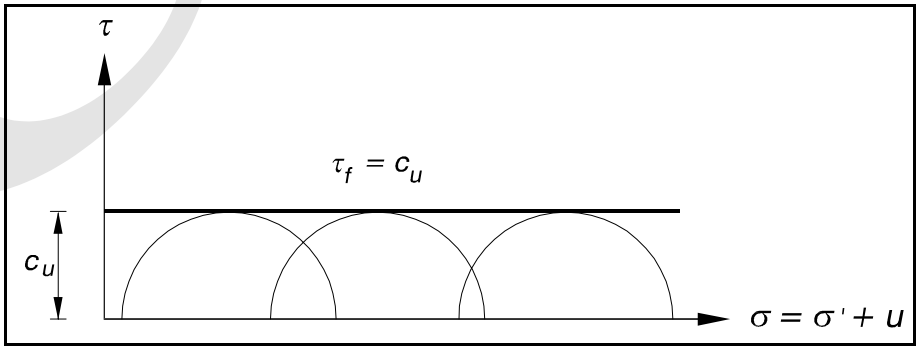

Figure VI-5-90. Failure criterion for a water-saturated clay in undrained condition defined from Mohr envelope

(b) For a specific clay with a given stress history, c_u depends solely on the initial effective stress conditions before the loading. Thus, the increase in σ in Figure VI-5-90 is equal to the increase in the pore pressure, u. In addition, the c_u-value and the deformation characteristics depend on the overconsolidation ratio, *OCR*, defined in Part VI-5-5-b, as well as on the rate and number of loadings, as discussed in Part VI-5-5-e on cyclic loading. Failure analysis related to cohesive soils in undrained conditions is performed on the basis of total stresses, σ, as opposed to analysis of noncohesive soils which is based on effective stresses, σ'.

(c) The relative density of cohesive types of soils cannot be determined, and for this reason these soils are usually classified according to shear strength properties (see Table VI-5-77).

Table VI-5-77
Classification of Clay According to Undrained Shear Strength, c_u

Descriptive Term	c_u (kN/m^2) (Hansbo 1994)	c_u (kN/m^2) (Tomlinson 1980)
Very soft	< 20	< 25
Soft	20 - 40	25 - 50
Firm	40 - 75	50 - 100
Stiff	75 - 150	100 - 200
Very stiff	> 150	> 200

(d) It should be noted that development of large shear stresses often involves soil deformations which might be damaging to the function of the structure. This is true especially for normally consolidated clay. For such cases the failure criterion must be defined as a strain level instead of the stress level, $c_{u.}$

(e) Cohesive soils are also classified according to their sensitivity to loss of strength when disturbed. The sensitivity, S_t, is defined as the ratio between the undrained shear strength of a specimen in undisturbed and in remoulded states. S_t is important for the estimation of shear strength reduction in case of disturbance due to activities such as piling and excavation. Fall-cone tests can be used to determine values of S_t. Soils are termed slightly sensitive when $S_t < 8$, moderately sensitive when $8 \le S_t \le 30$, and highly sensitive when $S_t > 30$. The last range includes quick clays for which $S_t \ge 50$.

d. Hydraulic gradient and flow forces in soils.

(1) Hydraulic gradient.

(a) If the seawater level and the groundwater level are horizontal and not moving, the pore water will be in static equilibrium corresponding to the hydrostatic pressure distribution and constant head, h. Any deviation from this stage causes a change in h, and generates a flow governed by the hydraulic gradient i, which is given by

$$i = \frac{\Delta h}{\Delta l} \qquad \text{(VI-5-215)}$$

where Δh is the difference in hydraulic head over the distance Δl. The hydraulic head is defined as

$$h = z + \frac{u}{\gamma_w} \tag{VI-5-216}$$

where z is a vertical coordinate, u is the pore pressure, and $\gamma_w = \rho_w g$ is the unit weight of the water (ρ_w is the mass density of water and g is gravity).

(b) A flow force of $i\gamma_w$ will act on the grains in the direction of the hydraulic gradient, i. The effective unit weight, γ_s', of a saturated soil can then be defined as

$$\gamma_s' = \gamma - \gamma_w \pm i\gamma_w \tag{VI-5-217}$$

where γ = unit weight of dry soil, the plus sign is used for vertical downward flow, and the minus sign is used for vertical upward flow. For an upward flow, if $i = (\gamma - \gamma_w) / \gamma_w$, then $\gamma_s' = 0$, corresponding to a total loss of soil bearing capacity, referred to as the limit stage of fluidization or liquifaction. The flow forces in the soil have to be included in the work or force balance equations for the failure limit states, either by including the flow force $i\gamma_w$ on all internal parts of the soil elements, or by including the pore pressures along the boundaries of the soil elements.

(c) The bulk flow velocity v introduced by i may be calculated by the one-dimensional extended Forchheimer equation

$$i = Av + B|v|v + C\frac{\delta v}{\delta t} \tag{VI-5-218}$$

where the coefficients A, B and C depend on the soil and water characteristics, i.e., grain size and shape, gradation, porosity, viscosity and the Reynolds number. The last term in Equation VI-5-218 can be neglected because it has only minor influence for wave-induced flow in cores, subsoils and rubble foundations related to coastal structures.

(d) Figure VI-5-91 illustrates the variation of A and B in Equation VI-5-218. Table VI-5-78 presents expressions of A and B as well as related flow coefficients found from experiments as listed in Burcharth and Anderson (1995). Considerable scatter in the flow coefficients is observed.

(2) Permeability.

(a) For $R_e < 1$, Equation VI-5-219 in Table VI-5-78 is most often presented as the Darcy equation

$$v = ki \tag{VI-5-220}$$

where k is a dimensional quality referred to as the permeability coefficient. Comparing the first term in Equation VI-5-219 with Equation VI-5-220 gives

$$k = \frac{n^3}{\alpha(1-n)^2}\,\frac{gd^2}{\nu} \tag{VI-5-221}$$

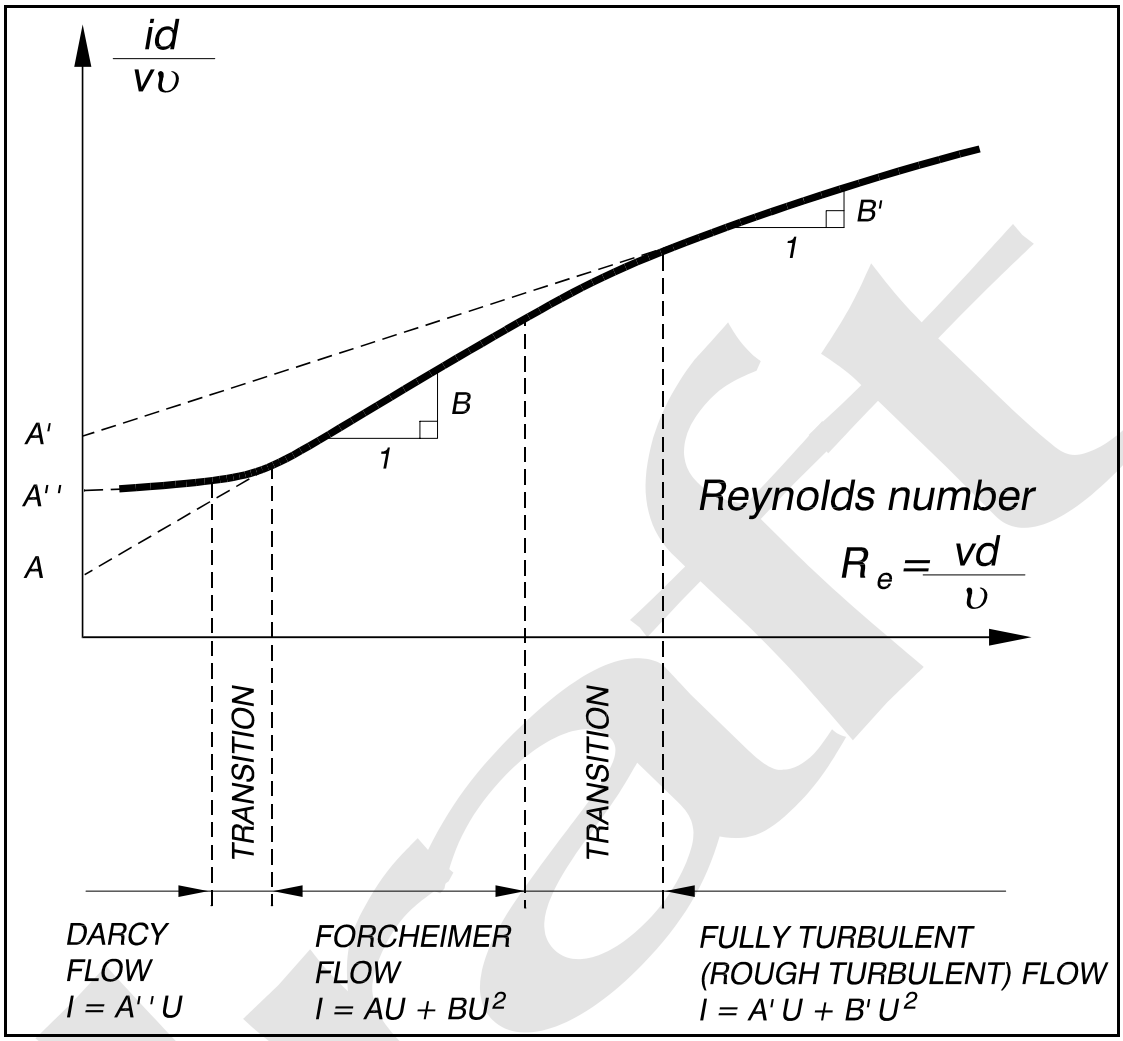

Figure VI-5-91. Representation of flow regimes for stationary porous flow based on a Forchheimer equation formulation (Burcharth and Anderson 1995)

(b) Equation VI-5-221 can be applied for fine materials like clay, silt, and fine sand ($d \leq 0.2$ mm) whereas for coarser material the nonlinear Equation VI-5-219 must be applied. It should be noted that α (and thereby k) depends on the Reynolds number and the soil gradation.

(c) Typical values of k are given in Table VI-5-79 for rather uniform sands. Order of magnitude values of k for stone materials are given in Table VI-5-80.

(3) Wave-induced internal setup. Wave action on a pervious slope causes a fluctuating internal water table (phreatic surface) and a setup as indicated in the figure in Table VI-5-81. The reason for the setup is that inflow dominates outflow due to larger surface area and longer duration. The setup increases if the shore side of the structure is impermeable, e.g., a rubble revetment built in front of a clay cliff.

(b) The setup can be estimated by a method (Barends 1988) presented in Table VI-5-81. The method is based on a linearization of the Forchheimer equation, where the permeability k for sands can be estimated from Table VI-5-79. For quarry-run materials, where linearization is less suitable, Equation VI-5-219 should be used. Order of magnitude values are given in Table VI-5-80.

Table VI-5-78
One-Dimensional Porous Flow Equation

One-dimensional steady porous flow equation and related coefficients. Burcharth and Anderson (1995).

$$i = \alpha \frac{(1-n)^2}{n^3} \frac{\nu}{gd^2} v + \beta \frac{1-n}{n^3} \frac{1}{gd} v^2 \qquad \text{(VI-5-219)}$$

where n Porosity
d Characteristic grain diameter, e.g. d_{50}
ν Kinematic viscosity ($1.3.10^{-6}$ m^2/s for water at 10^oC)
g Gravitational constant
v Bulk flow velocity

Typical values of α and β in Eqn. VI-5-219 for uniform sand and quarried rock materials

$$\frac{d_{85}}{d_{15}} = 1.3 - 1.9$$

Flow range	$\boldsymbol{Re = \frac{dv}{\nu}}$	$\boldsymbol{\alpha}$	$\boldsymbol{\beta}$
Darcy	< 1	300 - 400	0
Forchheimer	10 - 150	300	3.0 - 3.6
Fully turbulent	1,000 - 12,000	1,000 - 10,000	3.6 - 2.4[1]

[1] Smallest values of β correspond to largest R_e.

Table VI-5-79
Typical Values of Permeability, *k*, for Fine Materials

Material	Packing	*k* (m/s)
Coarse sand	loose	10^{-2}
	dense	10^{-3}
Medium sand	loose	10^{-3}
	dense	10^{-4}
Fine sand	loose	10^{-4}
	dense	10^{-5}
Silty sand	-	10^{-6}
Sandy clay	-	10^{-7}

(c) Besides storage of water due to internal setup of the phreatic level, also some storage due to compressibility of the soil rock skeleton and water-air mix can occur. However, for conventional structures such elastic storage will be insignificant compared to the phreatic setup storage.

(4) Pore pressure gradients in sloping rubble-mound structures.

(a) The horizontal wave-induced pressure gradient in the core of a rubble-mound breakwater can be estimated by the method of Burcharth, Liu, and Troch (1999) as presented in Table VI-5-82. The method is mainly based on pore pressure recordings from a prototype and large and small scale model tests.

Table VI-5-80
Typical Values of Permeability, *k*, for Stone Materials

Gradation Diameter Range (mm)	*k* (m/s)
100 - 300	0.3
10 - 80	0.1

(b) Equation VI-5-222 is valid only for rather permeable core materials ($d_{50} \geq 50$ mm) and for normal breakwater cross sections with open rear side, i.e., no excess pressure. Additionally, Equation VI-5-222 holds for the region between swl and level $SWL + 2H_s$, i.e., $0 \leq y \leq 2H_s$. In each point within this region the larger pressure gradients will be of the same order of magnitude as the horizontal gradient.

e. Cyclic loading of soils.

An essential part of the design of monolithic coastal structures is to ensure that the foundation soil or rubble base has sufficient capacity to carry both the static gravity loads and the wave-induced loads with an adequate safety margin and without excessive deformations. The bearing capacity under combined static and cyclic loads may be significantly smaller than under purely static loads. The strength of soils exposed to cyclic loading is influenced not only by the stress level and the stress variations but also by the soil drainage capability. Pore pressure build-up and related loss of strength might take place in rather impervious soils where the time scale of drainage or consolidation is larger than the time scale of the load cycles. The following sections discuss evaluation of drainage conditions under cyclic loading, approximation of wave-induced irregular loading in terms of equivalent cyclic loading, and estimation of strength and deformation of soils exposed to cyclic loading.

(1) Time scale of drainage and consolidation.

(a) In saturated soil, the immediate effect of a load-induced stress increment will be a similar increase in the total stress σ and the pore pressure u (see Equation VI-5-202), i.e., the loading will be carried solely by the pore water. The soil skeleton will not carry the extra load until it has rearranged itself. This can happen only if some pore water is squeezed out, due to the very small compressibility of the water compared to that of the skeleton. In permeable materials such as stone blankets this happens immediately, while in clay it can be a very slow process. The related decrease in volume is termed consolidation.

(b) The degree of consolidation is defined as

$$U = \frac{s_t}{s_\infty} \tag{VI-5-223}$$

where s_t is the settlement (decrease in layer thickness) at time t, and s_∞ is the final settlement reached when the soil skeleton is fully carrying the load. For coastal structures the dominating live load is caused by wave loading that varies in time. The time scale of consolidation has to be compared to the time scale of the loading to estimate U and thereby the effective stress in the soil.

(c) For the one-dimensional case Terzaghi showed that U in terms of average degree of consolidation is a function of the dimensionless time factor (Terzaghi and Peck 1944)

$$T_c = \frac{k\ M}{\gamma_w\ H^2}\ t = \frac{C_V}{H^2}\ t \tag{VI-5-224}$$

Table VI-5-81
Wave Induced Set-up in Sloping Rubble Mound Structures (Barends 1988)

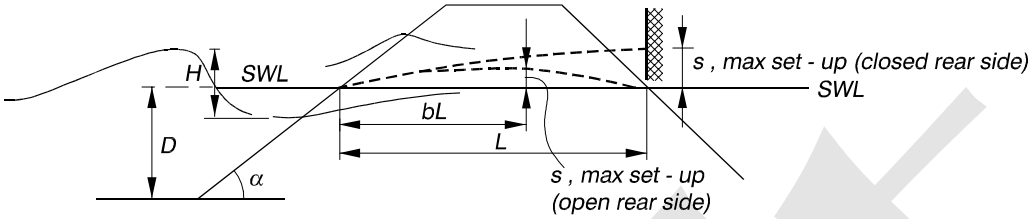

$$s/D = \sqrt{(1 + \xi\ F)} - 1 \qquad \text{for large waves, i.e. } H \leq D$$

$$s/H = \sqrt{(1 + \xi\ F)} - 1 \qquad \text{for small waves, i.e. } H \ll D$$

where $\xi = 0.1cH^2/(n\lambda\ D\ \tan\alpha)$
H = Height of incoming wave
n = Porosity of structure
c = Infiltration factor > 1. The magnitude is uncertain (Barends 1988) used $c \simeq 1.3$ to make calculations fit to conventional scale model test results
$\lambda = 0.5\sqrt{c\ k\ DT\ /n}$
α = Slope angle
k = Average permeability
T = Wave period
F = Function dependent on rear side conditions (open or closed) as given in diagram. The parameter b in the diagram defines position of maximum setup in the open case.

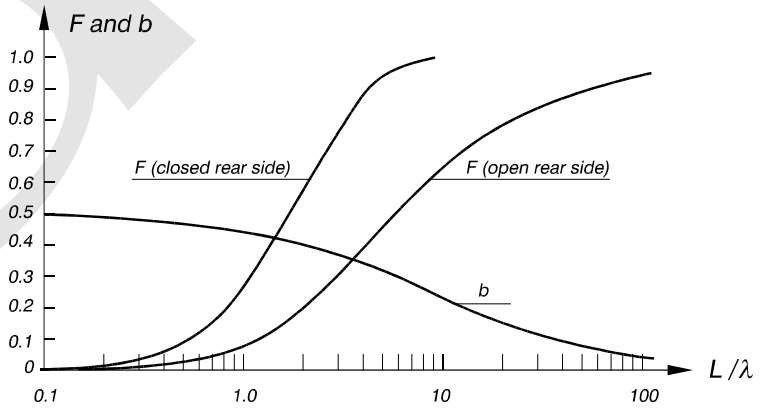

Table VI-5-82
Horizontal Wave Induced Pore Pressure Gradients in the Core of Rubble-Mound Breakwaters (Burcharth, Liu, and Troch 1999)

.

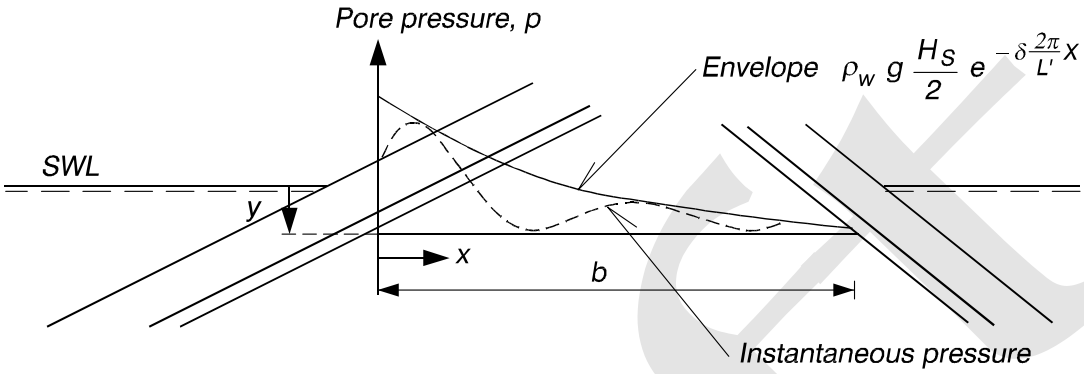

The horizontal pressure gradient

$$I_x = \frac{1}{\rho_w g} \frac{d_p}{dx}$$

$$= -\frac{\pi H_s}{L'} e^{-\delta \frac{2\pi}{L'} x} \left[\delta \cos\left(\frac{2\pi}{L'} x + \frac{2\pi}{T_p} t\right) + \sin\left(\frac{2\pi}{L'} x + \frac{2\pi}{t_p} t\right) \right] \qquad \text{(VI-5-222)}$$

where
- H_s Significant height of incoming waves
- δ $0.014 \frac{n^{0.5} L_p{}^2}{H_s b}$, damping coefficient
- n Porosity
- L_p Wavelength corresponding to peak of spectrum
- b Width of core at the level of interest
- L' $L_p/\sqrt{1.4}$, wave length in core valid for $h/L_p < 0.5$ (where h is the water depth)
- x Horizontal coordinate, $x = o$ at the seaward core boundary
- T_p Period corresponding to peak of the wave spectrum
- t Time
- ρ_w Mass density of water

where

C_V = coefficient of consolidation (= kM/γ_w)

k = permeability (see Table VI-5-79)

M = oedometer modulus

γ_w = unit weight of water

t = time

H = drainage distance, which is equal to layer thickness for one side drainage, and equal to half the layer thickness for double side drainage.

(d) Full consolidation (i.e., U=100 percent) is in principle never reached. Consolidation of U=99 percent corresponds to T_c-≈ 2, whereas U=95 percent corresponds to $T_c \approx 1.2$. The necessary time for almost 100 percent consolidation is approximated in practice as

$$t_{U(100\%)} = \frac{2\gamma_w H^2}{k\ M} \qquad \text{(VI-5-225)}$$

(e) By comparing t_U with the rise time of the wave-induced load, t_{rise}, it is possible to classify the wave loading and to estimate whether drained, partially drained or undrained conditions will be present. This criterion is given in Table VI-5-83.

Table VI-5-83
Classification of Loading and Soil Conditions

$\frac{t_{rise}}{t_{U(100\%)}}$	Type of Loading	Soil Condition
>> 1	Quasi-stationary	Completely drained
~ 1	Nonstationary	Partially drained
<< 1	Nonstationary	Undrained

(f) Typical wave loadings from nonbreaking waves on coastal structures have periods in the range $T \approx 2(t_{rise})$ = 3-20 sec. Using the $t_{U(100\ percent)}$ values in Table VI-5-84, if follows from Table VI-5-83 that sand subsoil under virgin loading should generally be regarded as undrained, except for coarse sand which in some cases might be regarded as partially drained. Under subsequent wave loadings fine sand should still be regarded as undrained, whereas medium sand typically might be regarded as partially drained, and coarse sand would be considered drained.

(g) Very short duration impulsive loadings from waves breaking on structures have load rise times on the order of t_{rise} = 0.01 - 0.05 s (see Figure VI-5-101); and in this case all soils, including quarry-rock rubble foundations, have to be regarded as undrained.

(2) Wave load transmission to monolithic structure foundations.

(a) Wave loads transmitted to the foundation soil/rubble by monolithic structures, such as caissons and superstructure parapet walls, depend on the period of the wave load as well as the mass of the structure and the deformation characteristics of the soil/rubble.

Example 5-2. Calculation of $t_{U(100\ percent)}$ for quartz sand.

The elastic plastic component of M for initial loading corresponding to mean normal effective stress $\sigma' \leq 300$ kPa is found to be

$$M = \begin{cases} 15 \quad MPa & \text{loose sand} \\ 150 \quad MPa & \text{dense sand} \end{cases}$$

The elastic component of M found by unloading and reloading at $\sigma' = 100$ kPa is found to be

$$M = \begin{cases} 80 \quad MPa & \text{loose sand} \\ 500 \quad MPa & \text{dense sand} \end{cases}$$

The drainage distance H is given as 5 m. Using these typical M-values together with the k-values given in Table VI-5-79, Equation VI-5-225 gives the consolidation times presented in Table VI-5-84.

Table VI-5-84
Example of Consolidation Times for Sand

Material	Packing	$t_{U(100\ percent)}$ (s)	
		Initial Deformation	Elastic Deformation
Coarse sand	Loose	3	0.6
	Dense	3	1
Medium sand	Loose	30	6
	Dense	30	10
Fine sand	Loose	300	60
	Dense	300	100

(b) The natural period $T_{n,s}$ of typical monolithic structures would normally be in the range 0.2 - 2 sec. If the period of the loading, T, is close to $T_{n,s}$ then dynamic amplification occurs resulting in increased loading of the foundation. Design wave loading can be separated into pulsating loads from nonbreaking waves and impulsive loads from waves breaking on the structure (see Figure VI-5-57). The pulsating loads have periods corresponding to the wave period, i.e., normally in the range 5-20 sec, which is much larger than $T_{n,s}$. Consequently, such low frequency loading is assumed to be transmitted to the foundation with unchanged frequency.

(c) Figure VI-5-92 illustrates how the resultant foundation load force of a wave-loaded caisson changes size, direction, and position during the wave cycle. The variation of the force resultant can be given by fully correlated time series of a tilting moment and a horizontal force. Figure VI-5-92 also illustrates the wave-induced stress variations in two soil elements (shown as hatched boxes).

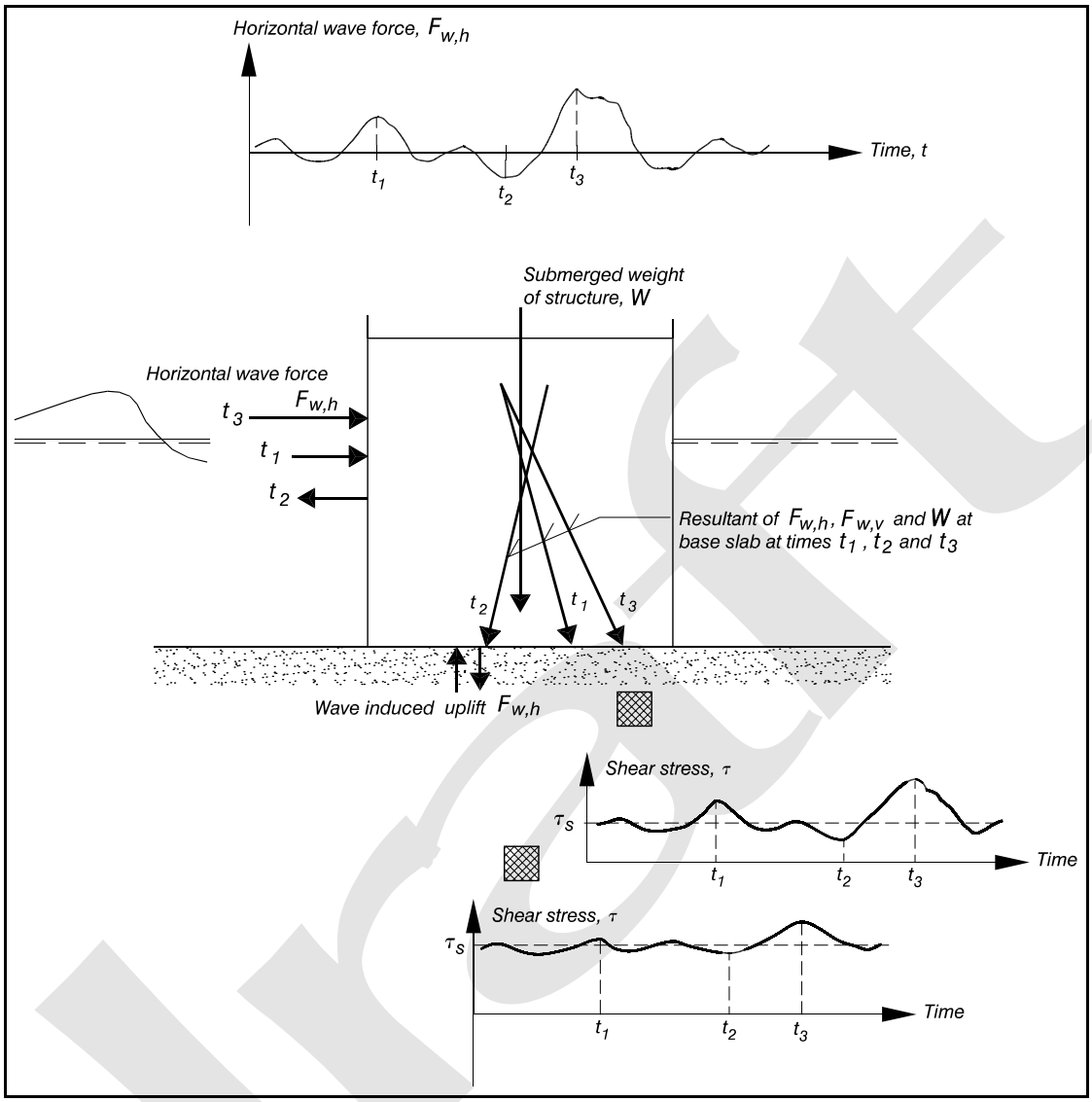

Figure VI-5-92. Illustration of wave induced forces on caisson foundation and related stress variations in the subsoil

(d) The initial shear stress τ_i prior to the installation of the structure is assumed to act under drained conditions, and the soil is assumed fully consolidated under this stress. $\Delta\tau_s$ is the change in the average shear stress due to the submerged weight of the structure. Depending on the type of soil, $\Delta\tau_s$ will initially act under undrained conditions, but as the soil consolidates, this shear stress will also be applied under drained conditions. In the case of rubble-mound foundations the consolidation will be instantaneous. For sand foundations drainage will occur rapidly, as indicated by Table VI-5-84, and it is reasonable to assume that the soil will consolidate before the structure experiences design wave loading. In addition, it is unlikely that pore pressures will accumulate from one storm to the next. For clays, consolidation occurs much more slowly, varying from months for silty-sandy very stiff clays to many years for soft clays. The amount of settlement and the corresponding increase in effective stresses, is calculated by ordinary consolidation theory the same as for structures on dry land.

(e) The effective static shear stress before wave loading is given by

$$\tau_s = \tau_i + \Delta\tau_s \qquad \text{(VI-5-226)}$$

(f) The initial shear stress, τ_i, is determined by the submerged weight of the soil as $\tau_i = 0.5\ (1 - K_o)\ p_o'$, where K_o is the coefficient of earth pressure at rest, and p_o' is the vertical effective overburden pressure. $\Delta\tau_s$ can be estimated from Newmark's influence diagrams, assuming homogeneous, isotropic and elastic soil (e.g., see Hansbo 1994 and Lambe and Whitman 1979). This is usually a good approximation if the soil is not close to failure. A rough rule of thumb is a load spreading of 1 (horizontal) to 2 (vertical).

(g) The behavior of the soil when exposed to the cyclic loading can be studied in triaxial tests or direct simple shear (DSS) tests. The irregular wave loading F_W during the design storm might be approximated by equivalent cyclic wave loadings, causing cyclic shear stress variations with amplitude τ_{cy} as given in Figure VI-5-93. However, it is more correct if the real stress variations in the subsoil, as illustrated in Figure VI-5-92, are approximated by an equivalent cyclic variation. The stress τ_{cy} should be determined by finite element analysis.

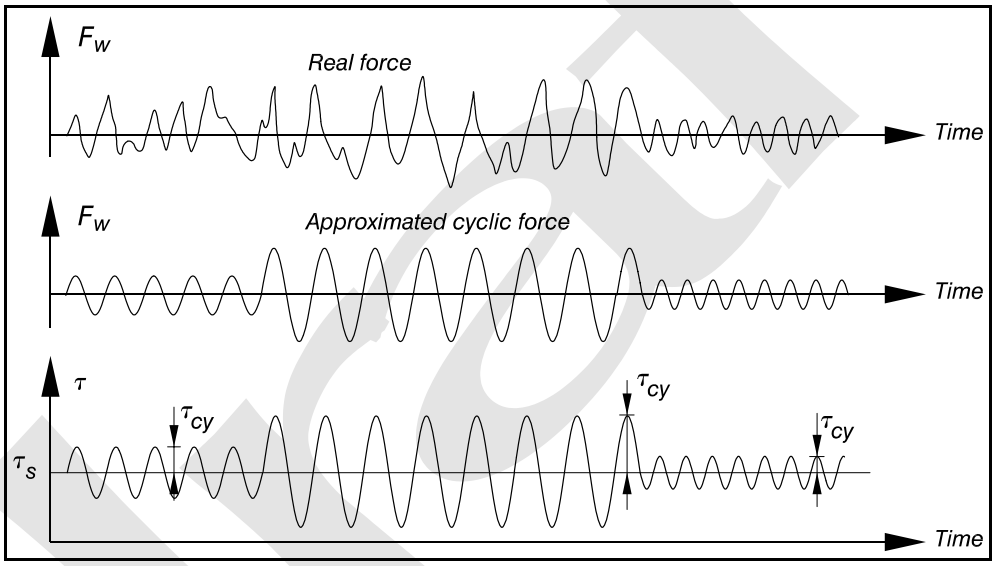

Figure VI-5-93. Illustration of approximate cyclic wave loading and related cyclic shear stress variation in a subsoil element during a storm sequence

(h) The criterion for determination of the equivalent cyclic stress in terms of τ_{cy} and number of cycles $N_{eqv,}$ is that the approximation gives the same effect as the actual load history. Procedures to determine N_{eqv} were presented by Andersen (1981, 1983). For sands, N_{eqv} may be computed by accumulating the permanent pore pressure generated during the cyclic load history, taking into account that drainage is likely to occur during the design storm. Calculation of the pore pressure accumulation can be performed using pore pressure diagrams established from cyclic stress-controlled laboratory tests. The dissipation of the permanent pore pressure due to both drainage towards free boundaries and grain redistribution can be determined by finite element analysis or, for idealized situations, by closed-form solutions. In principle, the cyclic shear strength of clays could also be computed by accumulating the permanent pore pressure. However, measurements in clays are more difficult to acquire than in sands. In addition, short-term drainage will not take place in clays; consequently, it is preferable to use the shear strain as a measure of the cyclic strength for clays. Moreover, for situations where the cyclic shear moduli under undrained conditions are of primary interest, the shear strain will also be a more direct parameter than the pore pressure.

(i) The stress conditions in the soil beneath structures subjected to combinations of static and cyclic loads are very complex even though the irregular loadings are approximated by equivalent cyclic loadings. Advanced finite element numerical modeling is the obvious tool for calculation of stress and strain development provided the model is carefully verified against documented test cases. As an alternative, a practical approximate method is presented by Andersen (1991) and Andersen and Høeg (1991). This method is based on the stress path philosophy in which laboratory tests are performed to simulate the stress conditions in few typical soil elements along potential failure surfaces as illustrated in Figure VI-5-94. The elements follow various stress paths which might be approximated to triaxial or direct simple shear (DSS) types of loading corresponding to various conditions of average stresses, τ_s and cyclic shear stresses, τ_{cy}. Additionally, the number of cycles to failure, N_f, and the shear strains are determined in the tests.

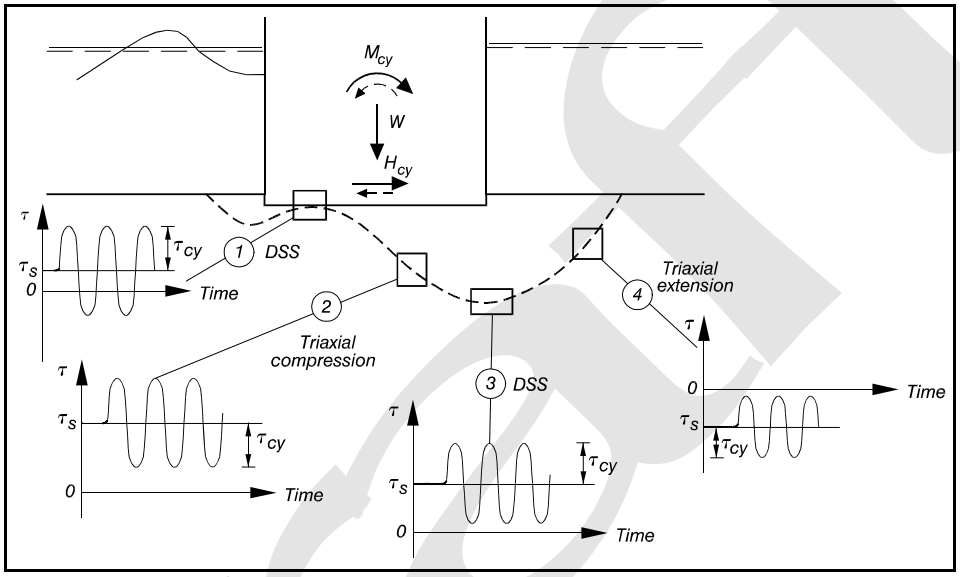

Figure VI-5-94. Simplified stress conditions for some elements along a potential failure surface (Andersen 1991)

(3) Noncohesive soil exposed to wave-induced cyclic loadings.

(a) For noncohesive soils, cyclic stress variations can either lead to strengthening of the soil or to soil weakening and eventual liquefaction due to pore pressure build-up. The outcome depends on soil permeability, average shear stress τ_s , wave-induced shear stress variations, and soil compaction. Pore pressure build-up does not happen in coarse materials like gravel and rubble foundation materials because of almost instant drainage. Consequently, only sand-sized noncohesive soils will be considered in the following discussion.

(b) Cyclic loading of soil specimens can be performed in undrained triaxial tests using a cell height-to-width ratio of one and lubricated cap and base, thus assuring uniform stress-strain conditions in the sample (Rowe and Barden 1964; Bishop and Green 1965; and Jacobsen 1967). From such tests the phenomena depicted in Figure VI-5-95 can be observed.

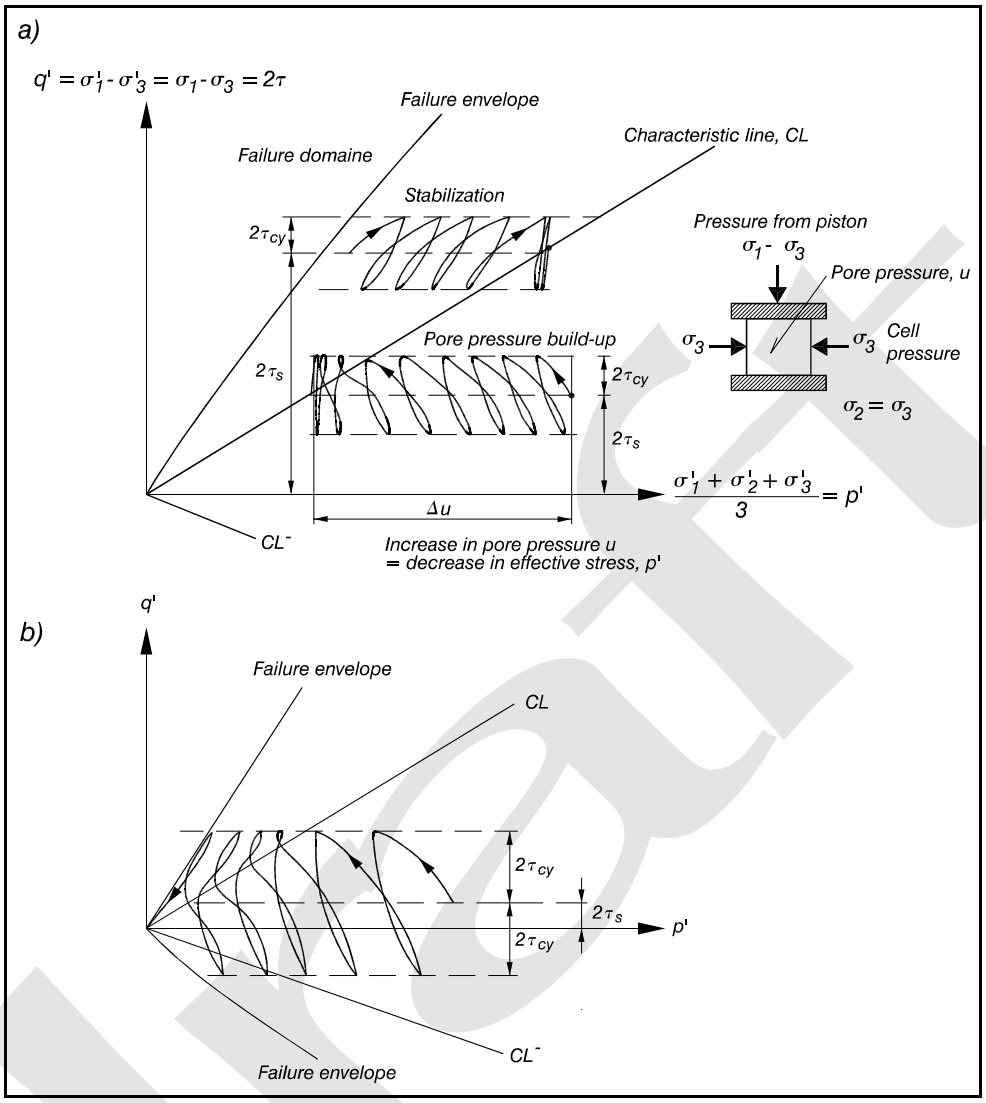

Figure VI-5-95. Illustration of (a) stabilization and pore pressure build-up, and (b) liquefaction undrained triaxial test on sand

(c) The shear stress τ is given by

$$\tau = \frac{\sqrt{3}}{2}\sqrt{J_2} \tag{VI-5-227}$$

where

$$J_2 = \frac{1}{6}\left[(\sigma_1' - \sigma_2')^2 + (\sigma_2' - \sigma_3')^2 + (\sigma_1' - \sigma_3')^2\right] \tag{VI-5-228}$$

and $\sigma_1' \geq \sigma_2' \geq \sigma_3'$ are the effective stresses in three orthogonal directions.

(d) The average effective stress level is given by

$$p' = \frac{\sigma_1' + \sigma_2' + \sigma_3'}{3} = \frac{\sigma_1 + \sigma_2 + \sigma_3}{3} - u \tag{VI-5-229}$$

where σ is total stress and u is the pore pressure, as in Equation VI-5-202. In undrained triaxial tests with cell pressure $\sigma_2' = \sigma_3'$ the piston generated stress (deviator stress) is

$$q' = \sigma_1' - \sigma_3' = \sigma_1 - \sigma_3 = 2\tau \tag{VI-5-230}$$

(e) In the $q' - p'$ diagram of Figure VI-5-95 the characteristic line (CL) separates stress domains where deviator stress fluctuations cause dilation and contraction. The CL signifies a stable state where further cyclic loadings will not lead to hardening or softening of the soil. Figure VI-95a shows that if the average stress τ_s is situated above the CL, the cyclic test will generate negative pore pressures leading to stabilization (hardening) of the soil.

(f) If τ_s is situated below the CL, cyclic tests will generate positive pore pressures and decreasing effective stress (softening). With small τ_s and large stress fluctuations τ_{cy}, liquefaction will occur as shown in Figure VI-5-95b if the stress path touches the CL$^-$ line.

The equations for the CL and CL$^-$ lines are

$$\text{CL:} \quad q' = \frac{6 \sin\varphi_{crit}'}{3 - \sin\varphi_{crit}'} p' \tag{VI-5-231}$$

$$\text{CL}^-\text{:} \quad q' = \frac{-6 \sin\varphi_{crit}'}{3 + \sin\varphi_{crit}'} p' \tag{VI-5-232}$$

where φ'_{crit} is the critical angle of friction, as given in Table VI-5-75. φ'_{crit} is independent of the relative density or porosity and is very close to 30 deg for sand in the range d_{50} = 0.14 - 0.4 mm (Ibsen and Lade 1998). The number of cycles to failure can be determined from a series of triaxial or DSS laboratory tests conducted with various combinations of τ_s and τ_{cy}.

(g) The previous discussion of the effect of cyclic loading is related to undrained conditions in laboratory tests. The assumption of undrained conditions is either true or on the safe side with respect to soil strength properties. However, sands in nature may experience partial drainage during a storm. The amount of drainage depends upon the permeability of the sand and the drainage boundary conditions. The drainage can be significant and should be considered in design because experience from laboratory tests has shown that the soil structure and the resistance to further pore pressure generation may be significantly altered when the excess pore pressure due to cyclic loading dissipates (Bjerrum 1973; Andersen et al. 1976; Smits, Anderson, and Gudehus 1978). Cyclic loading with subsequent pore pressure dissipation is referred to as precycling.

(h) Moderate precycling in sands may lead to significant reduction in pore pressure generation under further cyclic loading, even in dense sands. Precycling may occur during the first part of the design storm. The beneficial effect of precycling might be taken into account in cyclic testing of sand in the laboratory by

applying some precycling prior to the main cycling. As previously mentioned, the shear strength that the soil can mobilize to resist the maximum load (wave) depends on the effective stresses in the soil, and thus on the excess pore pressure that is generated during the storm. The shear strength also depends on whether the soil is contractive or dilative. If the soil is dilative and saturated, a negative pore pressure is generated when the soil is sheared under undrained conditions. This will give a higher shear strength than achieved for drained conditions. However, for sands one should be careful about relying fully on higher shear strength caused by negative pore pressure due to uncertainty about the amount of drainage that might take place. The amount of drainage during a cycle and the residual pore pressure at the end of a storm might be estimated from calculations with finite element programs. Examples of design diagrams based on such calculations are pressented in de Groot et al. (1996). A method valid for the estimation of the changes in p' in sand as function of the number of cycles was given in Ibsen (1999).

(4) Cohesive soil exposed to wave-induced cyclic loadings.

(a) The shear strength, c_u, of clay normally refers to undrained strain controlled tests of approximately 1-3 hr duration to reach failure. Clays will be practically undrained during a storm, and possibly also over a seasonal period including several storms. Because c_u for a specific clay in undrained conditions depends solely on the initial effective stress conditions before the loading, there will be only insignificant changes in c_u as long as drainage of the clay has not taken place.

(b) The stress-strain behavior of a specific clay determined from samples is affected by the test method, *OCR*, τ_s , τ_{cy} , N and the stress rate (load frequency). During the cyclic loading the pressure build-up causes a reduction of the effective stresses as illustrated in Figure VI-5-96. Figures VI-5-96a and VI-5-96b show development of failure by cyclic loading. Figure VI-5-96c shows stabilization of effective stress after 25 cycles.

(c) After a certain number of cycles, the failure envelope will be reached and large shear strains developed. The cyclic shear strength can be defined as

$$\tau_{f,cy} = (\tau_s + \tau_{cy}) \tag{VI-5-233}$$

(d) It is very difficult to determine accurately the change in pore pressure, and therefore, also the change in effective stresses in triaxial and DSS tests. Consequently, to determine the relationship between the shear strength c_u and τ_s, τ_{cy}, and number of cycles, N, it is better to examine the load increase to failure in normal static tests for samples already exposed to various ranges of cyclic loadings. From the load increase the actual c_u-value after a specific exposure in terms of τ_s, τ_{cy}, and N can then be estimated. Examples and information on such post-cyclic static shear strength are presented in Andersen (1988). For Norwegian Drammen clay, being a plastic clay with plasticity index $I_p = 27$ percent, it was found that cyclic loading causing large cyclic shear strains also caused significant reduction in the static shear strength. The reduction increases with the number of cycles. It was also found that the reduction is generally less than 25 percent as long as the cyclic shear strains are less than 3 percent and the number of cycles less than 1,000. This holds for *OCR*-values of 1, 4, and 10. Figure VI-5-97 shows an example of stress-strain behavior of Drammen clay. This example shows the importance of modeling the type of loading correctly when trying to determine the stress-strain behavior or the shear modulus in situ from laboratory tests.

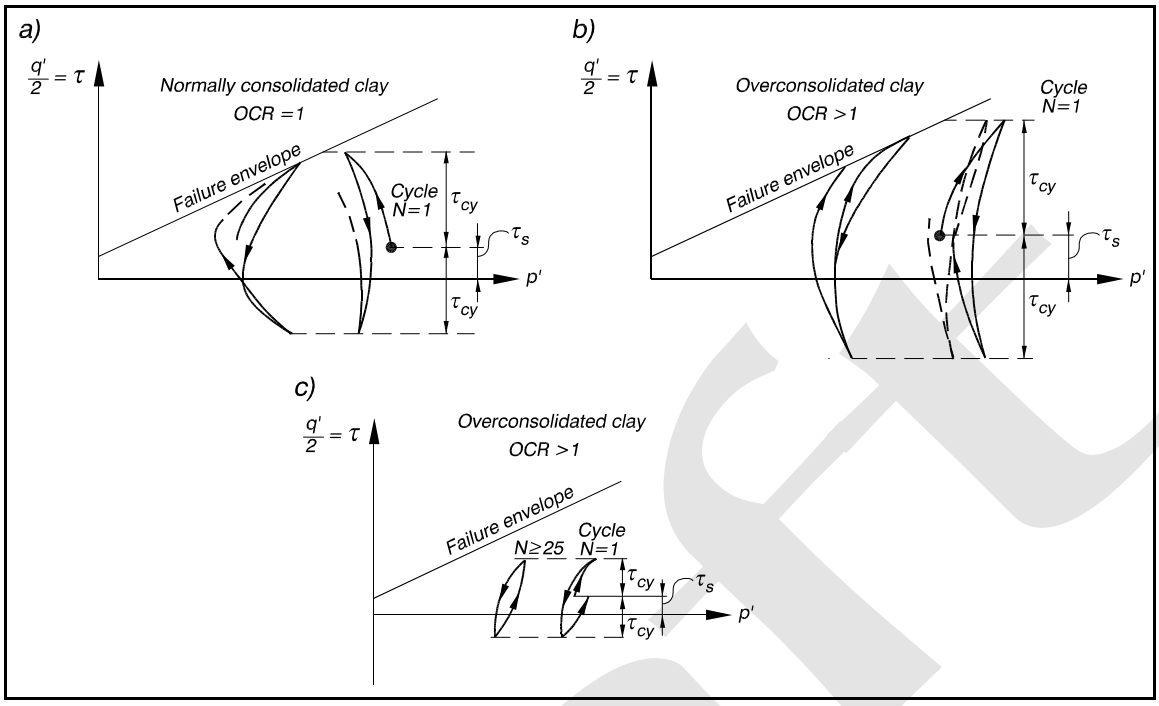

Figure VI-5-96. Illustration of effective stress paths for clay samples in undrained triaxial tests

(e) The number of cycles to failure, N_f, can be determined from a series of triaxial or DSS laboratory tests applying various combinations of τ_s and τ_{cy}. Due to the very large shear strain at failure, it is often appropriate to define failure as a lower strain level, the value of which must depend on the type and function of the structure. The test results can conveniently be plotted in diagrams as shown in Figure VI-5-98, where failure is taken when either the cyclic strain, γ_{cy}, or the average strain, γ_s, reaches 15 percent.

(f) In Figure VI-5-98 N_f is number of cycles to failure defined as either the cyclic strain γ_{cy} or the average strain γ_s reaching 15 percent. Figure VI-5-98a shows individual test results, and Figure VI-5-98b shows interpolated curves based on the individual tests. A diagram like Figure VI-5-98b can be transformed to normalized form using the vertical effective stress σ_{vc}' at the end of the cycling (consolidation), and the undrained static shear strength, σ_u, measured in strain-controlled tests. Figure VI-5-99 shows an example based on both triaxial and DSS tests.

(g) In Figure VI-5-99 σ_u^E, σ_u^C, and σ_u^{DSS} are undrained static shear strength in triaxial compression and extension tests and in DSS tests, respectively.

(h) By replotting the data from Figure VI-5-99 it is possible to show the relationship between the cyclic shear strength, $\tau_{f,cy}$, as defined by Equation VI-5-233, and N_f, σ_{vc}' and the undrained static shear strengths. An example is shown in Figure VI-5-100.

(i) A simple diagram for approximate correction of the static failure load to take into account the effect of cyclic loading in static calculations is presented in de Groot et al. (1996) for Drammen clay (OCR = 1, = 4 and = 40).

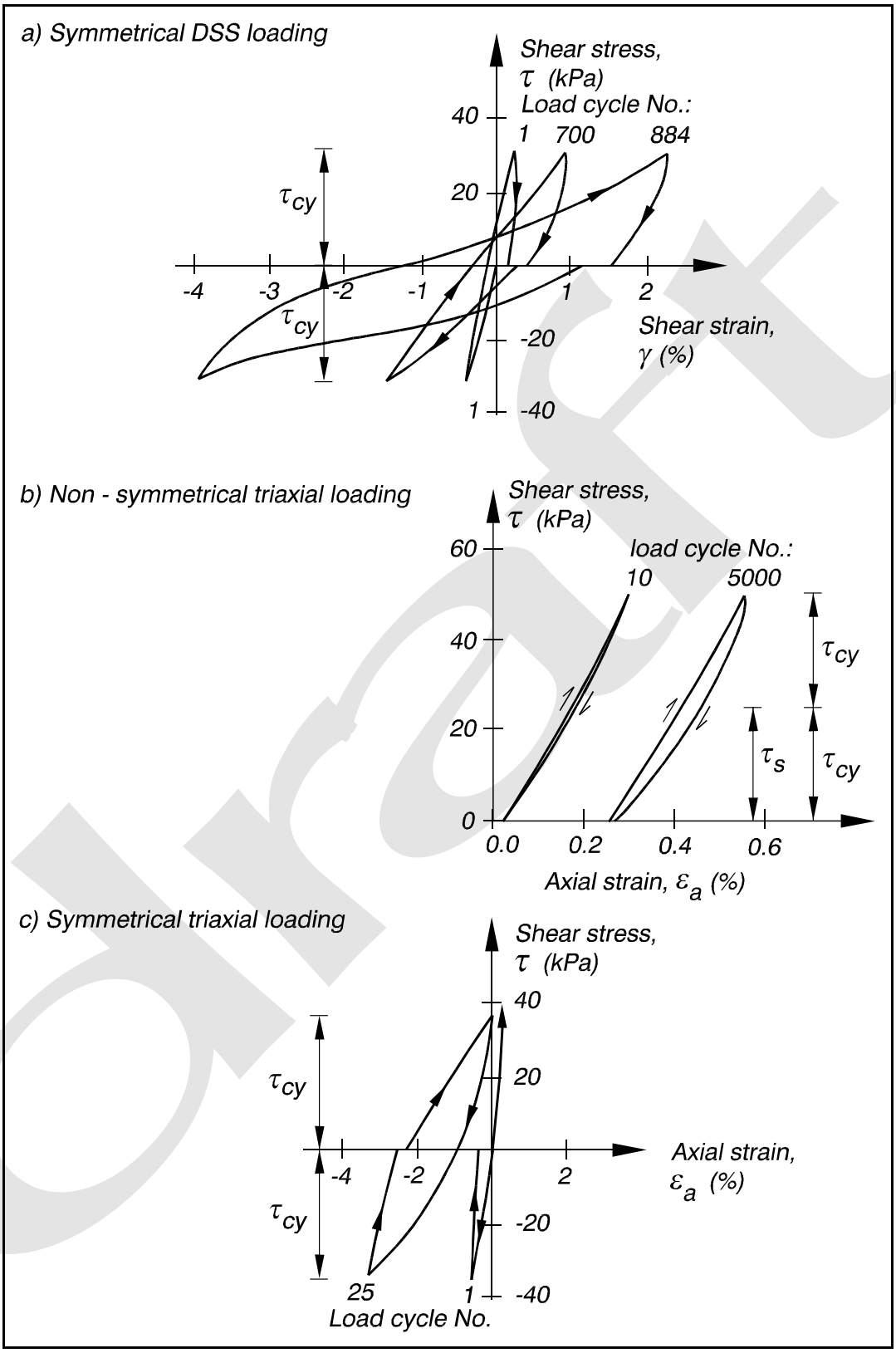

Figure VI-5-97. Stress strain behavior of Drammen clay (I_p = 27 percent) under various cyclic loading conditions corresponding to OCR = 4 (from Norwegian Geotechnical Institute 1992)

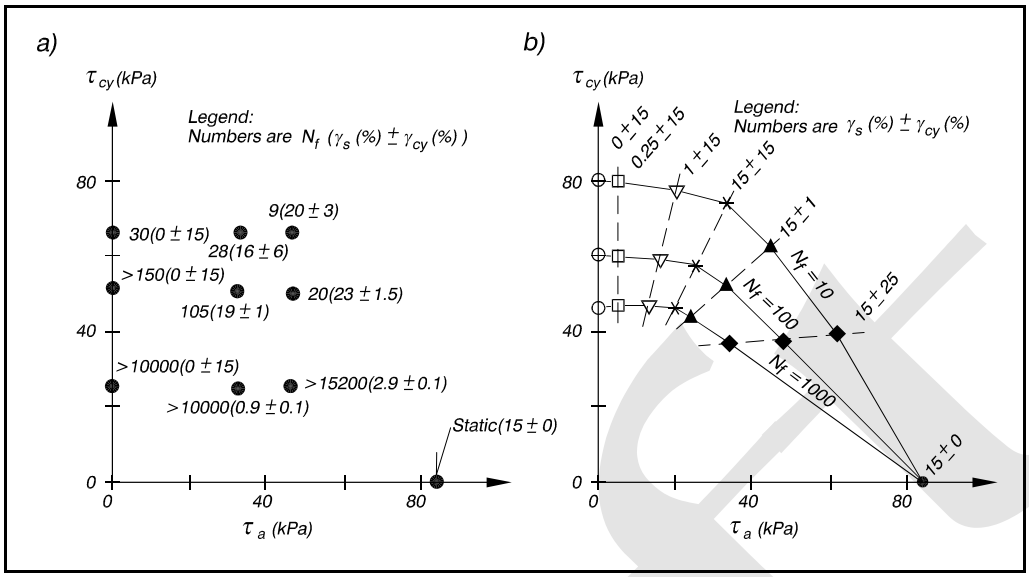

Figure VI-5-98. Result of cyclic tests on normally consolidated Drammen clay, with OCR = 1 and I_p = 27 percent (from Norwegian Geotechnical Institute 1992)

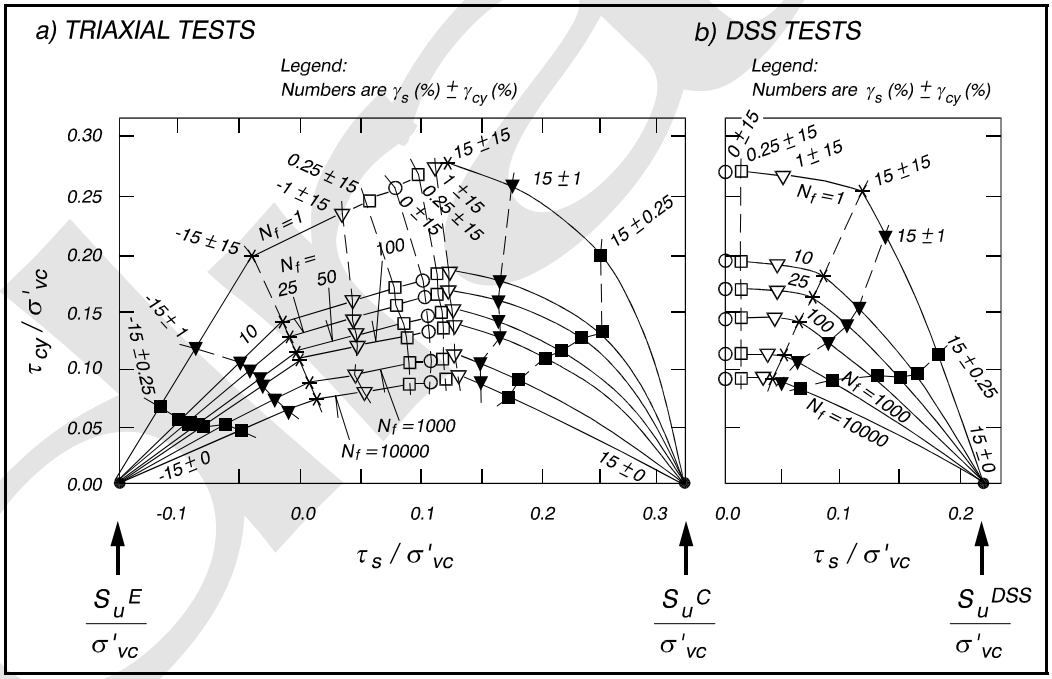

Figure VI-5-99. Example of normalized diagrams for cyclic loading of Drammen clay with *OCR* = 1, in triaxial tests (a), and DSS tests (b) (from Norwegian Geotechnical Institute 1992)

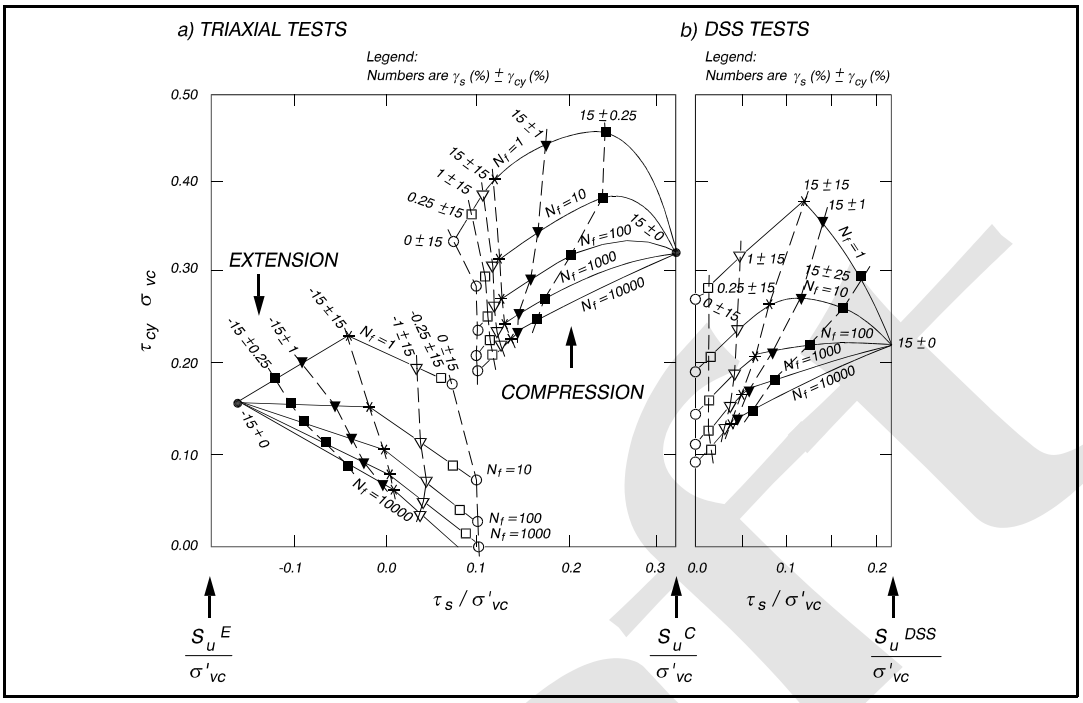

Figure VI-5-100. Cyclic shear strength of Drammen clay with *OCR* = 1 (from Norwegian Geotechnical Institute 1992)

f. Dynamic loading of soils under monolithic structures.

(1) Dynamic loading of soils and rubble rock foundations occurs when wave wall superstructures and vertical wall breakwaters are exposed to impulsive loads from waves breaking at the structures, as shown in Figure VI-5-56. The impulsive load magnitude can be very large, but the loads have very short durations with load periods in the range 0.1-1.0 sec for the peaked part of the loading. Because the natural period of some structures often are within (or close to) the same period range, dynamic amplification of the wave load and corresponding structure movements might occur.

(2) When moderately loaded, the soil and rubble rock will react approximately as an elastic material; whereas under severe loading, permanent deformations will occur, corresponding to plastic behavior.

(3) Determination of impulsive wave forces caused by waves breaking directly on vertical wall structures is extremely uncertain. The same can be said about the related loading on the foundation. In addition, breaking wave loads can be very large; therefore, direct wave breaking on the structure should be avoided. If necessary, the geometry or position of the structure should be changed to avoid large impulsive wave forces. In cases where the wave load is known, it is possible to obtain some estimates of the effect on the foundation as explained in the following paragraphs.

(4) The actual time of the wave loading is an important factor in the dynamic amplification. Model studies by Bagnold (1939) and Oumeraci (1991) showed that the load history of forces from waves breaking on vertical walls can be approximated with a church-roof like time-history as sketched in Figure VI-5-101.

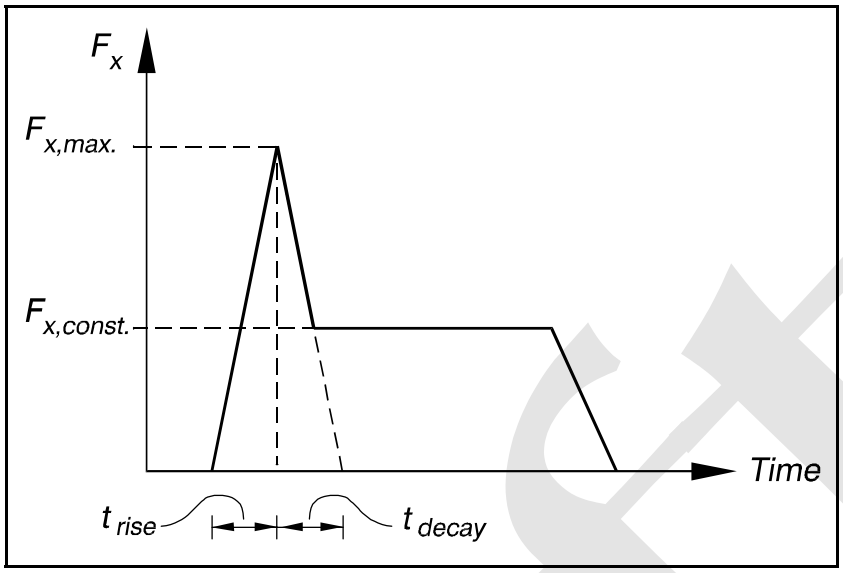

Figure VI-5-101. Approximation to horizontal wave load history for waves breaking directly on vertical walls

(5) For the elastic case it is possible to get a crude estimate on the dynamic amplification by modeling the soil-structure system as a rigid body resting on a linear elastic half-space, idealized by a lumped mass system where the geodynamic response is represented by a spring-dashpot model. A two-degrees-of-freedom system allowing only translatory motion, *x,* in the horizontal direction and rotation, φ, about the center of gravity, C_g, is commonly considered (see Figure VI-5-102).

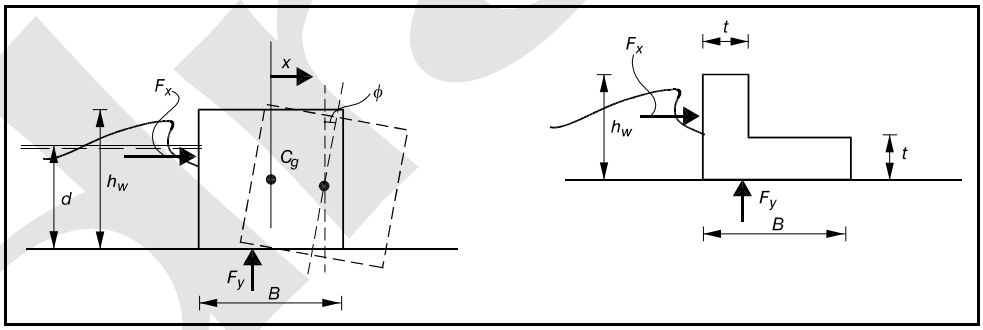

Figure VI-5-102. Definition of translatory and rotational motions and dimensions for caisson structure and parapet wave wall exposed to dynamic loading

(6) The effect of any impulsive loading can be found by solving the equations of motion for the complete translatory and rotational motion, provided the stiffness and damping coefficients are known. However, for practical design purposes a simple static approach can be accomplished by assuming an equivalent static load which will induce the same motions of the structure as those found from a dynamic calculation. The following definitions of dynamic load factors, Ω, show how the equivalent static force and motions are related to the dynamic force and motions.

$$\Omega_x = \frac{\max\ dynamic\ translation}{\max\ static\ translation} = \frac{\max\{x\}}{F_{x,\max}/k_x} = \frac{F_{x,equiv}}{F_{x,\max}}$$

$$\Omega_\varphi = \frac{\max\ dynamic\ rotation}{\max\ static\ rotation} = \frac{\max\{\varphi\}}{M_{\max}/k_\varphi} = \frac{M_{equiv}}{M_{\max}} \quad \text{(VI-5-234)}$$

where $F_{x,max}$ is defined in Figure VI-5-101, k_x and k_φ are stiffness coefficients, and M_{max} is the maximum wave-load-induced moment around the center of gravity. The moment also includes wave-generated uplift forces, F_y. If Ω_x, Ω_φ, k_x, k_φ, and the maximum wave loading F_x and M_φ are known, then the maximum motions and related equivalent static wave loadings can be determined. The vertical motion is of little interest for monolithic structures under predominantly horizontal wave loading.

(7) Pedersen (1996, 1997) presented diagrams of Ω_x and Ω_φ for caissons and wave wall superstructures with square footings (i.e., B x B shown in Figure VI-5-102) exposed to the type of loading shown in Figure VI-5-101. The soil was modeled as a linear elastic half-space. Pedersen used results of Lysmer and Richardt (1966) and Hall (1967) to obtain expressions for optimized constant values of stiffness and damping coefficients. An example of Pedersen's diagrams for caisson structures is shown in Figure VI-5-103 for load history $t_{rise}/t_{decay} = 1$ under triangular loading. T_{nd} is the coupled, damped natural period of the caisson. Pedersen showed that the constant part of the wave loading following the peak has little influence on the response if $F_{x,const.} \leq 0.5\ F_{x,max}$.

(8) Due to the many uncertainties and simplifying assumptions, diagrams such as shown in Figure VI-5-103 should be used only for judging the possibility of dynamic amplification. If dynamic amplification factors are found to be close to or greater than 1, then a detailed dynamic analysis should be performed or the structure design should be changed.

g. Slip surface and zone failures.

(1) Slip surface and zone failure calculations are based on limit state calculations related to assumed or approximate rupture figures. Two different solutions are applied:

(a) Statically admissible solutions are defined by stress distributions that satisfy equilibrium for stresses and loads for all involved soil elements. In homogeneous soils with sufficiently simple boundary conditions, e.g., straight and uniformly loaded boundaries, these types of approximate solutions may represent a simple and efficient solution technique. Many standard formulas and calculation methods in soil mechanics for bearing capacity and earth pressure problems are derived from statically admissible solutions. However, even slight modifications of the boundary conditions, and especially the introduction of inhomogeneous soil properties, may make a realistic solution of this type extremely complicated. Consequently, statically admissible solutions do not represent a generally applicable solution method, even if a limited number of standard cases are known and are widely used.

(b) Kinematically admissible solutions are defined by displacement fields that satisfy the boundary conditions for displacements as well as the associated flow rule (normality condition) within the theory of plasticity. Satisfying the flow rule makes the use of work equations possible. The flow rule requires the angle of friction φ and the angle of dilation ψ to be equal, although this is not true for frictional materials. To overcome this problem Hansen (1979) proposed to set $\psi = \varphi = \varphi_d$ where the modified angle of friction φ_d is defined by

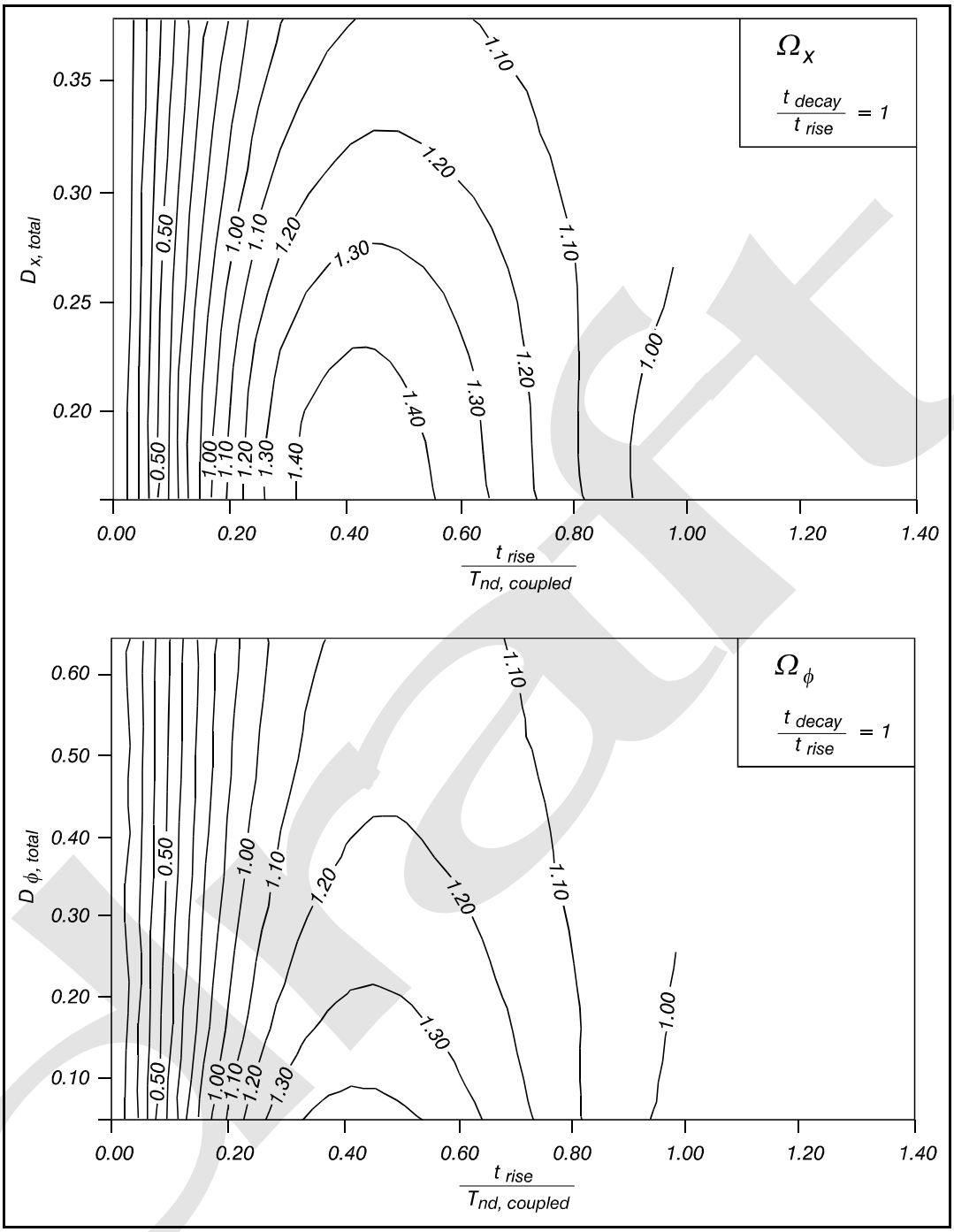

Figure VI-5-103. Amplification factors for translatory and rotational motions for caisson structure with square footing and triangular load shape (Pedersen 1997)

$$\tan\varphi_d = \frac{\sin\varphi \cos\psi}{1 - \sin\varphi\sin\psi} \tag{VI-5-235}$$

(c) When applying φ_d it follows that both statically and kinematically admissible solutions will always be on the safe side. Otherwise statically admissible solutions will either be correct or on the safe side,

whereas kinematically admissible solutions, according to the upper bound theorem, will either be correct or on the unsafe side.

(2) Experience indicates that solutions based on realistic rupture figures are in both cases generally close to the true situaton.

(3) For a given structure it is necessary to identify the most critical rupture figure, defined as the one which provides the lowest bearing capacity. For example, if work equations are used, then the rupture figure corresponding to the lowest ratio of work of stabilizing forces W_s to work of destabilizing forces W_d is the critical rupture figure. In any case in order to prevent failure and to have some safety the condition

$$\min \left(\frac{W_s}{W_d} \right) \geq 1 \qquad \text{(VI-5-236)}$$

must be fulfilled. If not, the structure design has to be modified or the soil strength improved (by preloading, compaction, or installation of drains), or the soil must be replaced.

(4) For a number of standard cases the rather complicated equations related to statically and kinematically admissible solutions have been simplified to practical force equations, formulae, and diagrams (e.g., the determination of foundation bearing capacity and soil pressures on walls). The formulae and diagrams are based not only on the basis of theoretical solutions but also on model tests and field experience. This compensates for non-exact kinematically admissible solutions.

(a) Stability of slopes.

- Slope instability failure modes for coastal structures are schematized by the various slip failure surfaces shown in the figures in Part VI-2-4-b. Slope instability is a conventional soil mechanics problem which is dealt with in almost every handbook on geotechniques and foundation engineering, e.g.,Terzaghi and Peck (1944), Taylor (1958), Lambe and Whitman (1979), Anderson and Richards (1985), and Hansbo (1994). However, the conventional treatment of the subject does not pay attention to wave loadings which characterize the special conditions for coastal structures.

- Direct wave action on a permeable slope increases the antistabilizing forces because the runup presents an extra load and creates fluctuating pore pressures and related antistabilizing hydraulic gradients in the structure. In addition, both waves and tides create pore pressure gradients in porous seabeds.

- Slope instability rarely occurs in conventionally designed rubble-mound structures. Stability problems can occur if the structure is placed on weak soils or on soil with weak strata because the slip failure plane passes through weaker materials. Very large breakwaters with steep slopes might be suspectable to stability problems within the structure itself especially if exposed to earthquake loading. Another type of failure related to rubble-mound slopes is sliding of one layer over another layer which is caused by reduced shear strength at the interface between two layers of narrow graded materials of different particle size and shape, e.g., armor layer and filter layer. If geotextiles are used, the interface shear strength is significantly reduced.

- The two load categories pertinent to coastal structure slope stability are listed below:

Long-term stability	Permanent loads, i.e., weight of structure and soils, permanent surface loads, and average loads from groundwater.
Short-term stability	Permanent loads as well as variable loads from waves (direct wave loading and seepage forces), seismic activity and vehicles. Ice loads are usually not dangerous to slope stability.

- For each of the load cases it is important to apply the relevant soil strength parameters. This includes consideration of soil strength degradation related to variable loadings, as discussed in Part VI-5-5-e of this chapter.

- Variable loads from waves and the related seepage forces should be considered for the two instantaneous load situations depicted in Figure VI-5-104 . The pore pressures and the related hydraulic pressure gradient and seepage forces in a homogeneous, isotropic breakwater structure can be estimated from flow nets if the Darcy equation (Equation VI-5-220) is taken as valid, or calculated using advanced numerical models. In Figure VI-5-104 the seabed is assumed to be impermeable compared to the breakwater. This is usually a good approximation for rubble-mound structures built of quarry materials.

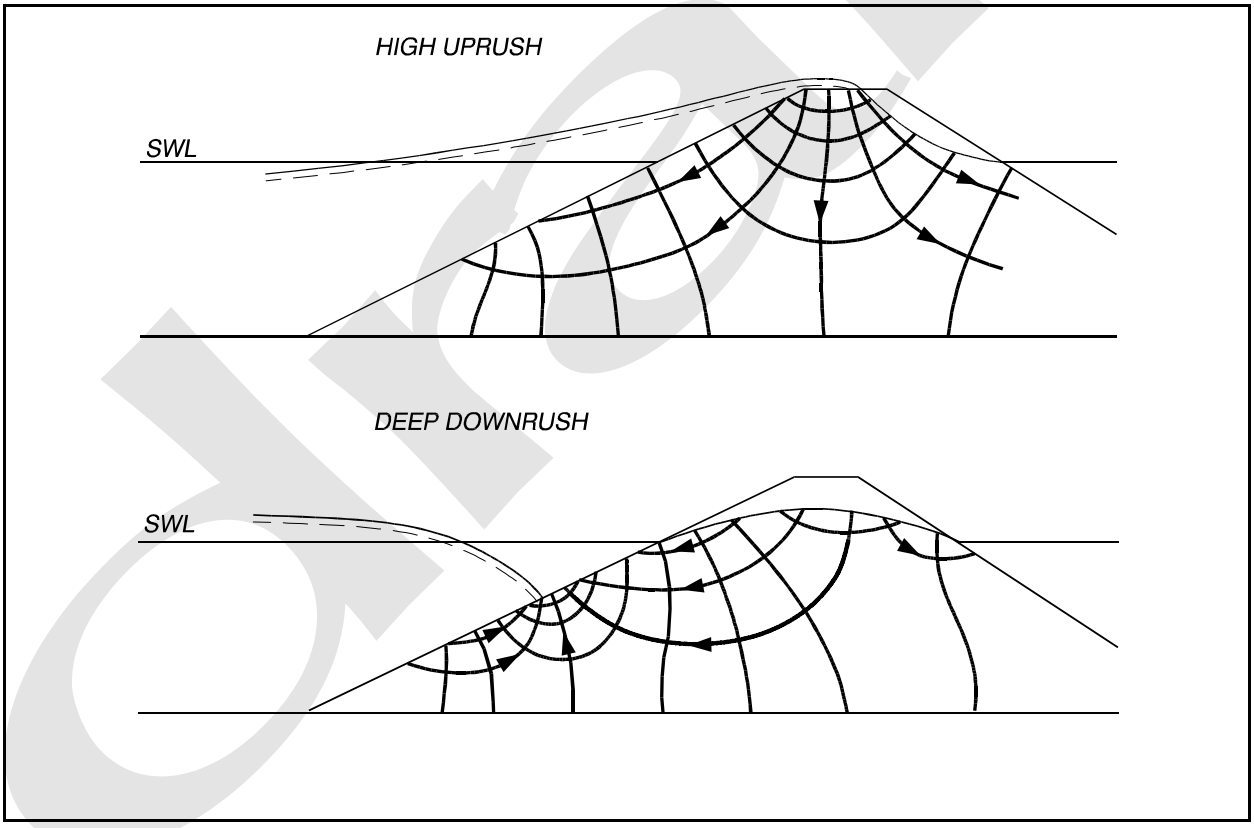

Figure VI-5-104. Illustration of flow nets in a homogeneous isotropic breakwater for two instantaneous wave load situations

- The pore pressure variation in a homogeneous seabed due to water level changes caused by tides and waves can be estimated by the method of de Rouck (1991) as shown in Table VI-5-85. The pore pressure in deeper strata corresponds to the hydrostatic pressure at mean water level. However, some seepage forces are created due to the reduction in pressure at the seabed surface beneath a wave trough during low tide. Tidal variations only causes vertical seepage forces due to the long tidal wavelength. However, short waves also cause horizontal seepage forces that are generally smaller than the vertical seepage forces. Figure VI-5-105 illustrates the flow net related to wave action.

- Equation VI-5-238 in Table VI-5-85 assumes that the compressibility of seawater is negligible compared to that of the grain skeleton, which is almost always the case. The pore pressure variations in the seabed underneath a rubble-mound structure can be determined from Equation VI-5-238 by estimating u_0 along the seabed surface using flow nets similar to those illustrated in Figure VI-5-104.

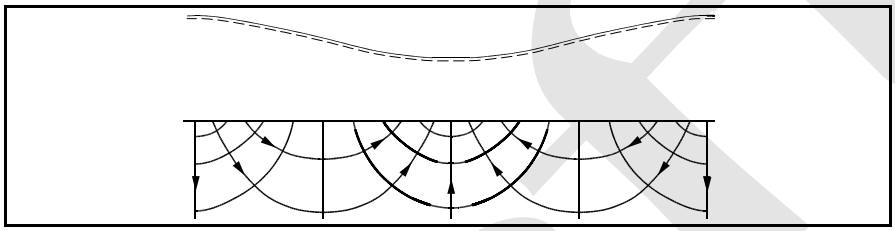

Figure VI-5-105. Illustration of instantaneous flow net in a homogeneous isotropic seabed under wave action

- It follows from Equation VI-5-238 that the attenuation of u with depth z decreases with more permeable and stiffer soil and with longer wave periods. Pore pressure variations due to tides (T = 12h 25 min) are only very slightly attenuated in sand, but there is a significant attenuation in clay. Pore pressure variations due to wind generated waves ($T < 20$ s) are strongly attenuated, even in sand.

- Seismic loads are usually taken into account by adding the seismic related horizontal inertia forces to the forces acting on the soil along with additional hydrodynamic forces which might result from the displacement of the soil body. Possible seabed scour should be taken into account when defining the bottom topography.

- For the two-dimensional case, simple methods of estimating slope stability have been developed. The stability can be investigated by considering the equilibrium of the soil body confined by the failure surface as illustrated in Figure VI-5-106. The ratio between the "stabilizing" and "driving" rotational moments, M_s and M_D, determined from all forces acting on the free soil body, is a measure of the stability.

- In Figure VI-5-106, W is the total weight of the soil element including pore water, S is the horizontal seismic inertia force, τ and σ' are shear stress forces and effective normal stress forces, respectively, u_s is the water pressure along the surface of the slope, and u_p is the pore water pressure along the failure circle. The variables τ and σ' usually vary along the failure circle. The parameter u_s is determined by the mean water level and the wave action. At the time of maximum runup a good approximation would be a hydrostatic pressure distribution, i.e., $u_s = \rho_w h$ where ρ_w is the water mass density and h is the local instantaneous water depth. The variable u_p can be determined from flow nets sketched for the instantaneous wave action situation, or from numerical models (Barends et al. 1983). Another, but in fact identical, formulation of the force balance indicated in Figure VI-5-106 would be to subtract the effect of hydrostatic water pressure corresponding to the mean water level from W, u_s and u_p.

Table VI-5-85
Wave and Tide Induced Pore Pressures in Permeable Seabeds (de Rouck 1991)

.

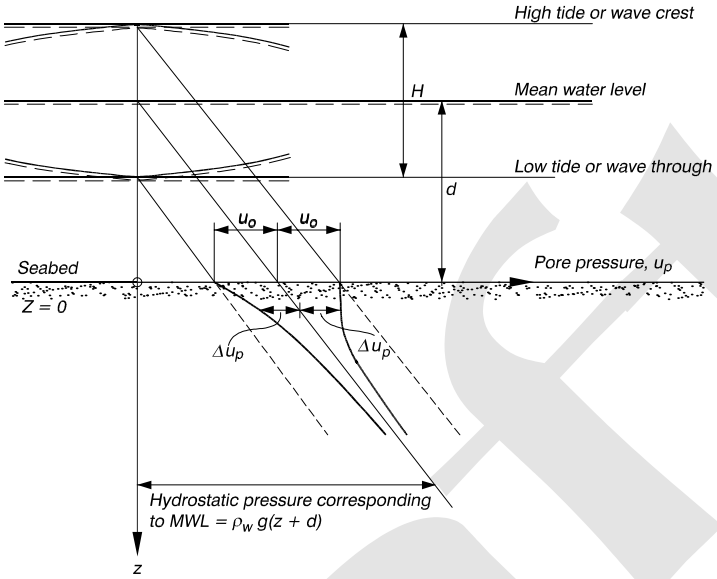

The pore pressure in depth z is given by

$$u_p = \rho_w g(z+d) + \Delta u_p \qquad \text{(VI−5−237)}$$

$$\Delta u_p = u_0 e^{-Az}\cos\left(\frac{2\pi X}{L} + \frac{2\pi t}{T} - Az\right) \qquad \text{(VI−5−238)}$$

where
Δu_p Pore pressure deviation caused by wave or tide
u_0 Bottom pore pressure amplitude
$= \rho_w g \frac{H}{2}$ for tides
$= \frac{\rho_w g H}{2\cosh\left(\frac{2\pi d}{L}\right)}$ for waves
assuming linear wave theory
ρ_w Mass density of water
g Gravitational acceleration
d Mean water depth
x Horizontal coordinate
L Wavelength
t Time
T Wave period
$A = \left(\frac{\rho_w g \pi}{k E_{oed} T}\right)^{0.5}$
k Darcy permeability coefficient
E_{oed} Oedometric compression modulus of soil

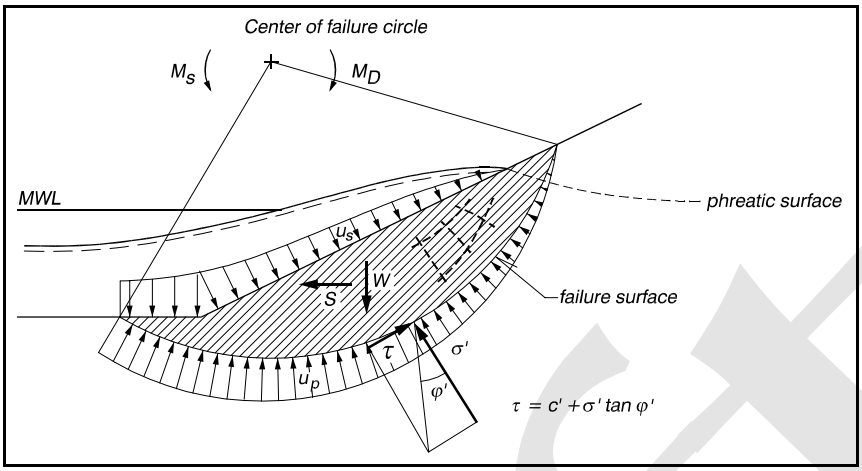

Figure VI-5-106. Illustration of forces to be considered in slope stability analysis

- A safety factor F for the slope stability can be expressed as

$$F = \frac{M_s}{M_D} = \frac{moment\ of\ stabilizing\ forces}{moment\ of\ driving\ forces} \quad \text{(VI-5-239)}$$

or as

$$F = \frac{available\ shear\ strength}{shear\ strength\ required\ for\ stability} \quad \text{(VI-5-240)}$$

- If the failure surface is circular then the resultant force of the pore pressure u_p goes through the center of the circle and will not contribute to M_D. In this case it is common to define a safety factor as

$$F = \frac{moment\ of\ shear\ strength\ along\ failure\ circle}{moment\ of\ weight\ of\ failure\ mass\ and\ surface\ loads} \quad \text{(VI-5-241)}$$

- The minimum value of F has to be identified by varying the position of the center of the failure circle and the radius. Also, F must be larger than unity to assure stability. The determination of the actual (minimum) safety factor for a given slope requires usually many trial failure surfaces calculations. It is important to notice that F is not a general safety factor because it depends on the applied definition. A specific value of F does not express a unique safety level.

- Various hydraulic load situations must be evaluated, such as a rapid run-down situation in which the phreatic surface in the slope material remains in a high position due to slow drainage (see Figure VI-5-104). This load situation, which occurs when rather impermeable materials are used, might be approximated and treated like rapid (instantaneous) drawdown known from earth dam design. Morgenstern and Price (1965) provide stability charts of F (Equation VI-5-239) as a function of slope angle, ratio of drawdown height over water depth, and soil strengths c' and φ'.

- The critical circular failure surface and the related safety factor F can be determined directly following the method of Janbu (1954a, 1954b) for the case of homogeneous soil, stationary water table and undrained conditions, i.e., the soil strength is given by the undrained shear strength c_u. Hansbo (1994) presented diagrams for determination of F as function of slope geometry, water level, c_u, and surface load.

- A unique solution when determining slope stability for soils with an internal angle of friction, φ, cannot be obtained because of four unknowns and only three equations of static equilibrium. If φ' is constant along the failure surface, one solution to the problem is to substitute the circle with a logarithmic spiral, i.e.,

$$r = r_1 \exp(\omega \tan\varphi') \tag{VI-5-242}$$

in which the radius vector forms an angle φ' with its normal at each point of the curved surface. The unknown frictional forces along the failure surface now pass through the center of the spiral as shown in Figure VI-5-107.

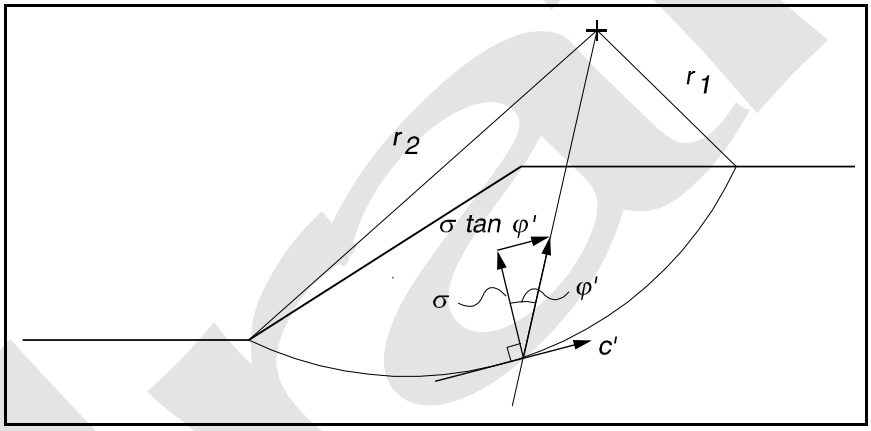

Figure VI-5-107. Illustration of logarithmic spiral

The stabilizing moment due to friction and cohesion, both taken as constants, is given by

$$M_s = \frac{1}{2} c' (r_1^2 - r_2^2) \cot\varphi' \tag{VI-5-243}$$

- The logarithmic spiral is not kinematically admissible as is the case for a circular (or straight line) failure plane. However, the deviation between the two curves is not significant in most cases.

- The simple methods illustrated in Figures VI-5-106 and VI-5-107 cannot be applied to inhomogeneous soils in which the soil strength parameters c' and φ' vary along the failure surface. This situation arises when the slip surface goes through both the rubble-mound and seabed soil, or through layered parts of the rubble structure where the interfacial friction angles are different (smaller) from the friction angle of the rubble. Moreover, if weak strata are present, then the slip surface will not be circular or log-spiral shaped because the failure surface tends to go through the weak layers as illustrated in Figure VI-5-108.

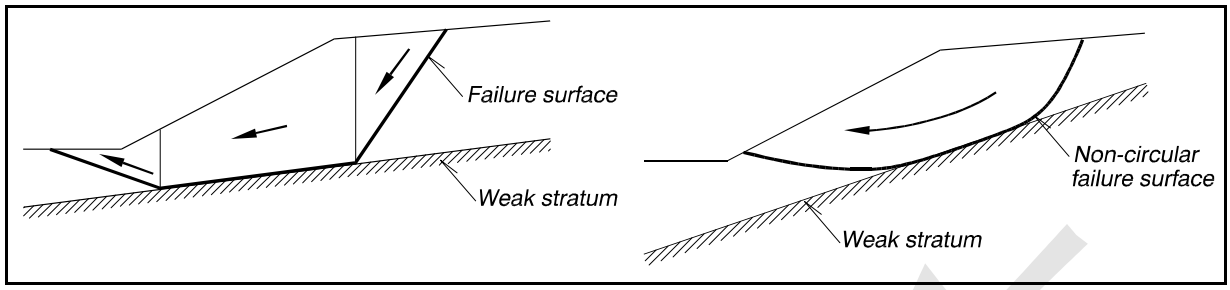

Figure VI-5-108. Illustration of failure surface in case of weak stratum

- For inhomogeneous conditions, slope stability is generally analyzed by the method of slices. The soil body is separated into fictitious vertical slices having widths that are determined such that c' and φ' can be assumed constant within a slice. Slope stability is analyzed by considering all the forces acting on each slice, as shown by Figure VI-5-109. The failure surface that gives the lowest stability has to be identified by trial calculations. In Figure VI-5-109, W is the total weight of the slice including surface load, u_p is the total pore water pressure at the bottom of the slice, and the parameters P and T are the horizontal and vertical forces, respectively, on the sides of the slice.

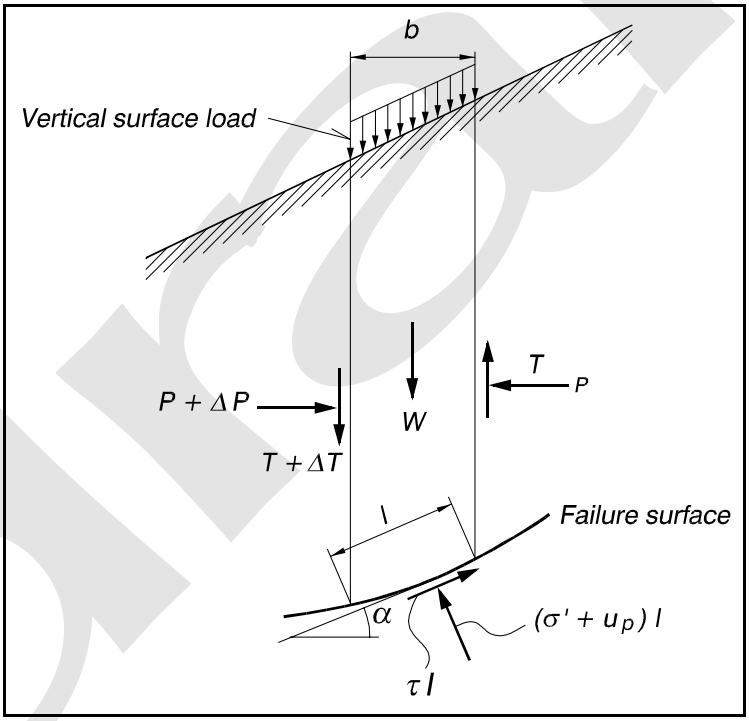

Figure VI-5-109. Illustration of forces on a soil slice in the method of slices slope stability analysis

- Several approximate methods exist for determining F, as defined by Equation VI-5-241. The most commonly applied methods are the ordinary method of slices and the simplified method of slices by Bishop. Both methods are based on the assumption of circular-cylindrical failure surfaces. The reasonableness of this assumption should be considered in light of the comments about weak strata.

- The Ordinary Method of Slices, also known as the method of Fellinius (1936), assumes that the resultant of the forces P and T acting upon the sides of any slice have zero resultant force in the

direction normal to the failure direction are for that slice. It is also assumed that the failure surface is circular-cylindrical. The related safety factor is given by

$$F = \frac{\sum_{i=1}^{n} [c_i' l_i + (W_i \cos\alpha_i - u_{pi} l_i) \tan\varphi_i']}{\sum_{i=1}^{n} W_i \sin\alpha_i} \quad \text{(VI-5-244)}$$

If c' and φ' are taken as constants, Equation VI-5-244 simplifies to

$$F = \frac{c' L + \tan\varphi' \sum_{i=1}^{n} (W_i \cos\alpha_i - u_{pi} l_i)}{\sum_{i=1}^{n} W_i \sin\alpha_i} \quad \text{(VI-5-245)}$$

where L is the total length of the circular failure surface. The values of F calculated by Equations VI-5-244 or VI-5-245 fall below the lower bound of solutions that satisfy static analysis. Thus, the method is on the safe side. The method of slices was further developed by Janbu (1954a) and Bishop (1955).

- The Simplified Method of Slices by Bishop (1955) is valid for a circular-cylindrical failure surface, and it assumes that the forces acting on the sides of any slice have zero resultant in the vertical direction, i.e., ΔT in Figure VI-5-109 is zero. The related safety factor, defined by Equation VI-5-241, is

$$F = \frac{R \sum_{i=1}^{n} [c_1' b_i + (W_i - u_{pi} b_i) \tan\varphi_i'] / [(1 + \tan\alpha_i \tan\varphi_i' / F) \cos\alpha_i]}{M_D + R \sum_{i=1}^{n} W_i \sin\alpha_i} \quad \text{(VI-5-246)}$$

where R is the radius of the failure surface circle and M_D is the driving moment of any load not included in Figure VI-5-109. Because F is implicitly given, an iteration procedure must be used; however, convergence of trials is very rapid.

- The Method of Slices by Janbu (1954a, 1973) is for more complicated situations where circular-cylindrical slip surfaces cannot be used, and a method for composite failure surfaces of arbitrary shape must be applied. The method is based on a combination of equations expressing moment and force equilibrium of each slice, and an iteration method for calculating F must be used.

- Most slope failures are three-dimensional. An approximate treatment of a three-dimensional slope failure is illustrated in Figure VI-5-110. The safety factors, F_1, F_2, and F_3, for three parallel cross-sections are computed. An estimate of the safety factor, F, for the whole body can then be estimated as the weighted safety factor using the total free body soil weights, W_1, W_2, and W_3, above the failure surface in each cross section as the weighting factors.

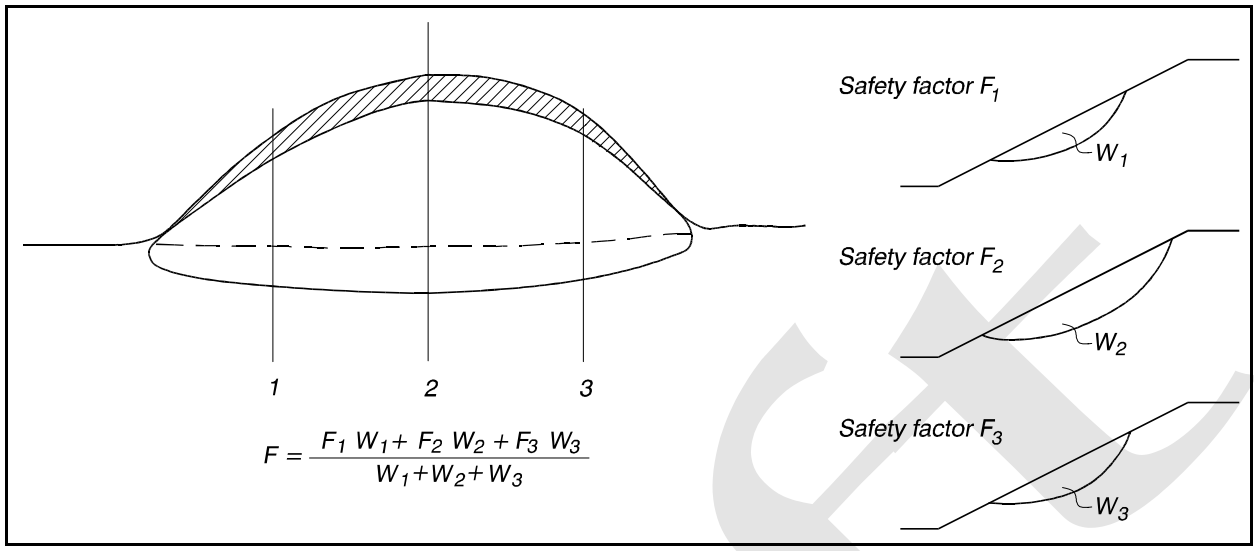

Figure VI-5-110. Illustration of safety factor *F* for three-dimensional slope failure

(2) Bearing capacity.

- The bearing capacity of a foundation is the load, transferred through the foundation - soil interface, that will initiate soil failure. Thus, bearing capacity is related to the ultimate limit state. The bearing capacity of the foundation of monolithic structures or structure elements like caissons and parapet concrete superstructures must be analyzed, and sufficient safety must be implemented in the design. Typical bearing capacity failure modes are shown in Part VI-2-4, "Failure Modes of Typical Structure Types."

- Rubble-mound breakwater structures placed on weak seabed soils might suffer from insufficient seabed bearing capacity. This can be investigated by the slip surface analysis explained in the previous section on slope stability.

- Bearing capacity calculations are based on zone failure analysis. In the case of homogeneous soil conditions the vertical bearing capacity of strip footings and individual rectangular footings can be estimated by formulae developed by Meyerhof (1951, 1963) and Brinch Hansen (1961, 1970), presented in Tables VI-5-86 and VI-5-87. The formulae, which represent a further development of Prandtl's and Terzaghi's theories for concentrically loaded horizontal footings, are valid for static loading and homogeneous soil conditions within the space of the zone failures.

- Brinch Hansen (1970) extended his formula to cover also the bearing capacity of statically loaded footings with inclined base in the vicinity of a slope. The formula which is termed the general bearing capacity formula is presented in Table VI-5-88 as an addition to the formula in Table VI-5-87.

- If foundation zone failures penetrate into more than one type of uniform soil then the formulae given in Tables VI-5-86, VI-5-87 and VI-5-88 cannot be applied, and the bearing capacity must be estimated by trial and error calculations in which the most critical rupture figure providing the lowest bearing capacity is identified.

Table VI-5-86
Bearing Capacity Formula for Rectangular Concentrically Statically Loaded Horizontal Footings (Meyerhof 1951, 1963)

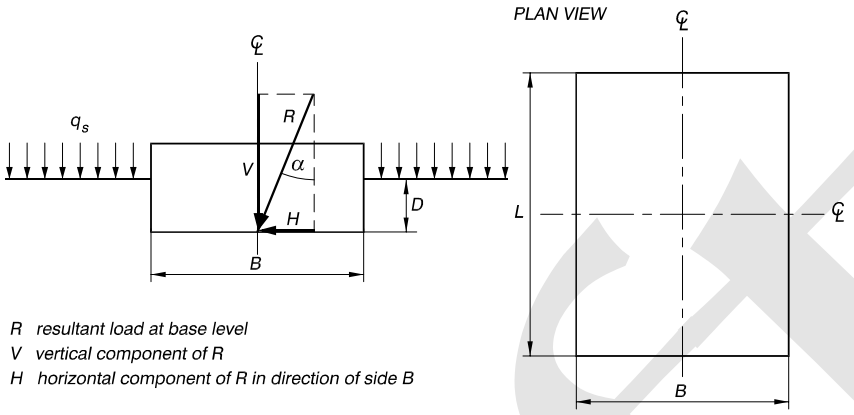

R resultant load at base level
V vertical component of R
H horizontal component of R in direction of side B

Ultimate vertical bearing capacity per unit area of the footing:

$$q_u = \frac{Q^{N_u}}{BL} = \frac{1}{2}\,\bar{\gamma}'\,B\,N_\gamma\,s_\gamma\,d_\gamma\,i_\gamma + q'\,N_q\,s_q\,d_q\,i_q + c\,N_c\,s_c\,d_c\,i_c \qquad \text{(VI–5–247)}$$

Q_u	Ultimate (maximum) value for the vertical component of the load
B	Width of footing
L	Length of footing, always $\geq B$
D	Minimum depth of footing below soil surface
$\bar{\gamma}'$	Average effective weight of soil from base level to depth B under base level
q'	Effective overburden pressure at base level (contribution from surface load q_s and effective weight of soil above base level)
c	Shear strength of soil. c_u for undrained conditions, and c' (effective) for drained conditions
φ'	Effective friction angle of soil determined by plain strain tests. Friction angle φ'_{triax} determined by triaxial test should be replaced by $\varphi' = (1.1 - 0.1\ B/L)\varphi'_{triax}$

Bearing capacity factors:

$$N_\gamma = (N_q - 1)\tan(1.4\,\varphi')$$
$$N_q = \exp(\pi\tan\varphi')\tan^2(45^0 + \varphi'/2) = \exp(\pi\tan\varphi')(1+\sin\varphi')/(1-\sin\varphi')$$

$$N_c = \begin{cases} (N_q - 1)\cot\varphi' \\ \pi + 2 \qquad \text{for undrained conditions } (\varphi' = 0) \end{cases}$$

Shape coefficients:

$$s_\gamma = s_q = \begin{cases} 1.0 & \text{for } \varphi' = 0^0 \\ 1 + 0.1\,(B/L)\tan^2(45^0 + \varphi'/2) & \text{for } \varphi' \geq 10^0 \end{cases}$$

$$s_c = 1 + 0.2\,(B/L)\tan(45^0 + \varphi'/2)$$

Depth coefficients:

$$d_\gamma = d_q = \begin{cases} 1.0 & \text{for } \varphi' = 0 \\ 1 + 0.1\,(D/B)\tan(45^0 + \varphi'/2) & \text{for } \varphi' \geq 10^0 \end{cases}$$

$$d_c = 1.0 + 0.2\,(D/B)\tan(45^0 + \varphi'/2)$$

Inclination coefficients:

$$i_\gamma = \begin{cases} 1.0 & \text{for } \varphi' = 0 \\ (1 - \alpha/\varphi')^2 & \text{for } \varphi' \geq 10^0 \end{cases} \qquad \alpha = \arctan(H/V)$$

$$i_q = i_c = (1 - \alpha/90^0)^2$$

Table VI-5-87
Bearing Capacity Formula[1] for Rectangular Statically Loaded Horizontal Footing (Brinch Hansen 1961, 1970)

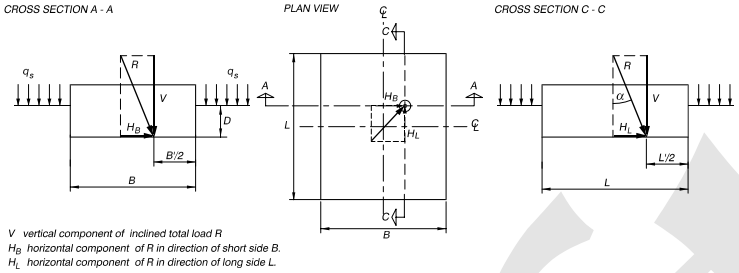

Ultimate vertical bearing capacity per unit area of effective footing:

$$q_u = \frac{Q_u}{B'L'} = \frac{1}{2}\,\bar{\gamma}'\,B'\,N_\gamma\,s_\gamma\,d_\gamma\,i_\gamma + q'\,N_q\,s_q\,d_q\,i_q + c\,N_c\,s_c\,d_c\,i_c \qquad \text{(VI-5-248)}$$

Q_u Ultimate (maximum) value for the vertical component of the load

$B' =$ $B - 2e_B$, effective width of footing, $B' \geq 0.4B$

$L' =$ $L - 2e_L$, effective length of footing, $L' \geq 0.4L$

D Minimum depth of footing below soil surface

$\bar{\gamma}'$ Average effective weight of soil from base level to depth B under base level

q' Effective overburden pressure at base level (contribution from surface load q_s and effective weight of soil above base level)

c Shear strength of soil. c_u for undrained conditions, and c' (effective) for drained conditions.

φ' Effective friction angle of soil determined by plain strain tests. Friction angle, φ'_{triax}, determined by triaxial tests should be replaced by $\varphi' = 1.1\varphi'_{triax}$.

Bearing capacity factors:

$$N_\gamma = 1.5(N_q - 1)\tan\varphi'$$

$$N_q = \exp(\pi\tan\varphi')\tan^2(45^0 + \varphi'/2) = \exp(\pi\tan\varphi')(1+\sin\varphi')/(1-\sin\varphi')$$

$$N_c = \begin{cases} (N_q - 1)\cot\,\varphi' \\ \pi + 2\ , \end{cases} \qquad \text{for undrained conditions } (\varphi' = 0)$$

Shape coefficients:

$$s_\gamma = 1 - 0.4\ B'/L' \quad \text{, must always be} \geq 0.6$$

$$s_q = 1 + \sin\,\varphi'\ B'/L'$$

$$s_c = 1 + 0.2\ B'/L'$$

Depth coefficients:

$$d_\gamma = 1$$

$$d_q = 1 + 2\tan\varphi'(1-\sin\varphi')^2\ \arctan(D/B')$$

$$d_c = 1 + 0.4\ \arctan(D/B')$$

Inclination coefficients:

$$\left.\begin{array}{l} i_\gamma = (1 - \frac{0.7H_B}{V + B'\,L'\,c'\,\cot\varphi'})^5 \\ i_q = (1 - \frac{0.5H_B}{V + B'\,L'\,c'\,\cot\varphi'})^5 \end{array}\right\} \quad \text{if the quantity inside the bracket becomes negative then the bearing capacity is negligible.}$$

$$i_c = \begin{cases} i_q - \frac{1-i_q}{N_q - 1}\ \simeq\ i_c & \text{for } \varphi' \neq\ 0 \\ 0.5(1 + (1 - \frac{H_B}{B'\,L'\,c_u})^{0.5}) & \text{for } \varphi' = 0 \end{cases}$$

[1] Failure can take place either along the long side or the short side of the footing. The formulae given above correspond to the first case. For the second case substitute L' for B', B' for L', and H_L for H_B.

- Eccentricity of the load, R, can, according to Meyerhof (1953), be taken into account by calculating the ultimate bearing capacity for a fictitious centrically loaded footing with width B' and length L' given by

$$B' = B - 2e_B \qquad \text{and} \qquad L' = L - 2e_L \tag{VI-5-249}$$

where e_B and e_L are the eccentricity of R in the directions of the width and length of the footing, respectively, as shown in Figure VI-5-111. Values of B' must always be smaller than L' in the calculation of q_u when using Equation VI-5-247. Moreover, the eccentricities are limited to $B' \geq 0.4\,B$ and $L' \geq 0.4\,L$ corresponding to e smaller than 0.3 times the width of the footing. Otherwise a failure configuration underneath the unloaded part of the footing might develop. This situation is not covered by Equation VI-5-247. For the case of inclined loading, the method does not apply if horizontal sliding of the foundation occurs.

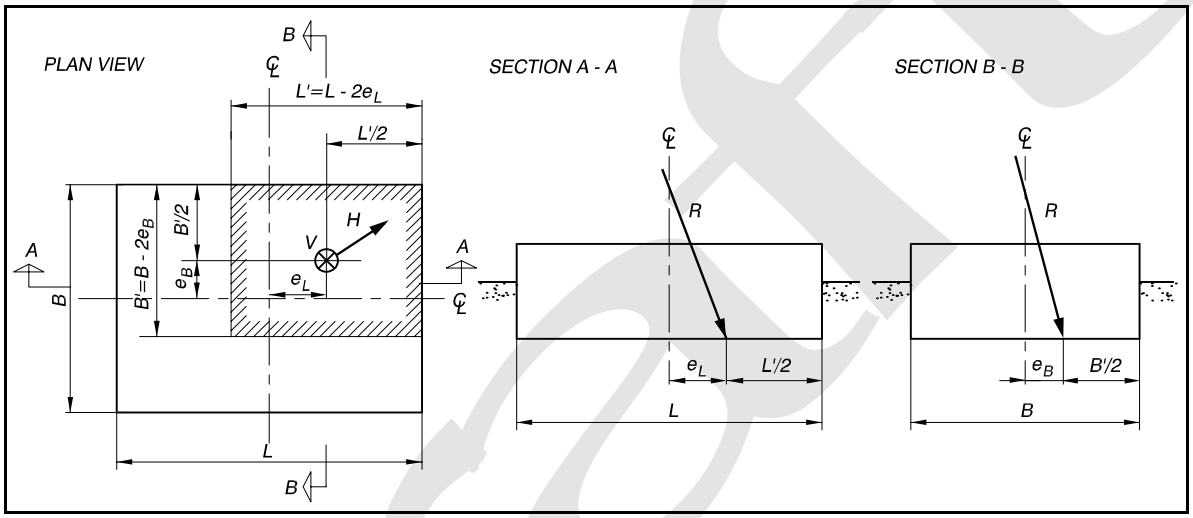

Figure VI-5-111. Illustration of fictitious footing to replace real footing under eccentric loading conditions

- For the case of nonhorizontal foundation base and ground surface, Brinch Hansen (1967, 1970) introduced a base inclination coefficient, b, and a ground inclination coefficient, g, in his bearing capacity formula to obtain a more general formula. In the context of coastal structures, sloping base and sloping ground surface are mostly relevant for cohesionless rubble materials as indicated by Figure VI-5-112, which shows a wave wall superstructure and a caisson on a high rubble-mound foundation. Also shown is the simplified geometry of the wave wall superstructure base and of the rear side of the mound foundation to be applied in the Brinch Hansen formula for cohesionless materials given in Table VI-5-88.

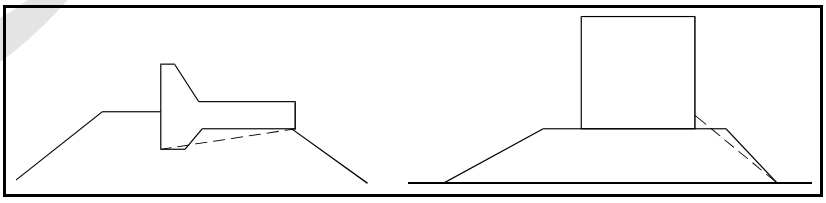

Figure VI-5-112. Simplified base and rear slope geometries to be applied in the general bearing capacity formula Table VI-5-86

Table VI-5-88
General Bearing Capacity Formula for Rectangular Statically Loaded Inclined Footing on Cohesionless Soil in Vicinity of Slope (Brinch Hansen 1961, 1967, 1970)

R foundation load
V foundation load component normal to the base
H foundation load component in plane of the base

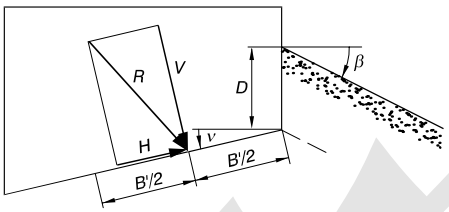

Ultimate bearing capacity per unit area of the footing:

$$q_u = \frac{Q_u^N}{B'\ L'} = \frac{1}{2}\ \bar{\gamma}'\ B'\ N_\gamma\ s_\gamma\ d_\gamma\ i_{\gamma b}\ b_\gamma\ g_\gamma\ + q'\ N_q\ s_q\ d_q\ i_q\ b_q\ g_q \qquad \text{(VI-5-250)}$$

Q_u^N is the ultimate (maximum) value for the load component normal to the base.

The formula is identical to Eq VI-5-248 except for the missing c-term ($c_u = 0$) and for the addition of the coefficients b and g, and a modified i_γ - coefficient.

Base inclination coefficients:

$$b_\gamma = \exp(-2.7\ \nu\ \tan\varphi')$$

$$b_q = \exp(-2\ \nu\ \tan\varphi')$$

Ground inclination coefficients:

$$g_\gamma = g_q = (1 - 0.5 \tan\beta)^5$$

Modified load inclination coefficients:

$$i_{\gamma_b} = (1 - (0.7 - \nu^0/450^0)\ H/V)^5$$

Limitations:

The angles ν and β must be possitive but $\nu + \beta$ must not exceed 90^0. β must be smaller than φ'.

- Where the foundation inclined loading has a large horizontal component, the passive pressure *P* indicated in Figure VI-5-113 should be included in the force balance instead of using the depth coefficients in the calculation of the bearing capacity with Equations VI-5-248 and VI-5-250.

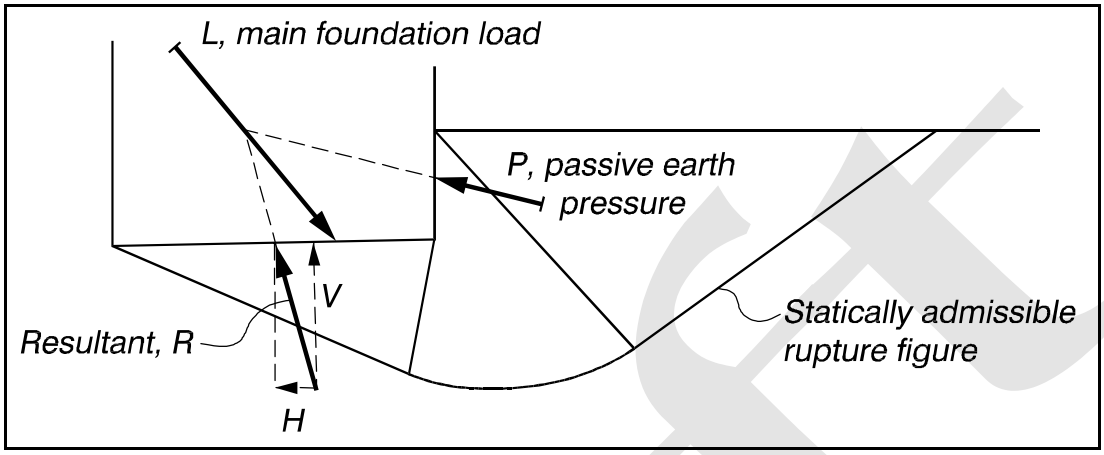

Figure VI-5-113. Illustration of passive earth pressure *P* to be included in the determination of the foundation load resultant *R* in place of the depth coefficients in Equations VI-5-248 and VI-5-250

- Note that the bearing capacity formulae given in Tables VI-5-86, VI-5-87, and VI-5-88 are all approximations. Consequently, for final design more detailed bearing capacity calculations are recommended.

- Publications of PIANC provide the limit state equations for rupture figures related to the two-dimensional case of a statically loaded monolithic structure with horizontal base placed on a rubble foundation overlaying a seabed of sand or clay.

- Following Equation VI-5-236, the limit state equations are defined as

$$g = W_s - W_d \geq 0 \tag{VI-5-251}$$

- A related measure of safety can be defined as

$$F = \frac{W_s}{W_d} \tag{VI-5-252}$$

- For more accurate estimations of three-dimensional bearing capacity, it is necessary to use advanced finite element calculations.

- The given bearing capacity formulae for statically loaded foundations could be applied for dynamic loadings using a dynamic amplification factor on the load as discussed in Part VI-5-5-f, Equation VI-5-234. Such simplified methods can be used in conceptual design, but detailed design of large structures should use more accurate methods if there is a risk of dynamic load amplification.

h. Settlement.

(1) For coastal structures, settlement is related both to the seabed soils and to the structure mound materials. The mound materials are generally cohesionless permeable materials such as quarrystones, quarry-run, gravel, and coarse sand. The seabed soils are in most cases fine and less permeable materials such as sand, silt, and clay, quite often layered. Soft and muddy deposits exist in many places, especially in estuaries, deltas, and river outlets. Settlement is the direct result of volume reduction of the soil mass, and it is caused by escape of water from the voids between particles and compression of the particle skeleton.

(a) Vertical settlement of coastal structures is generally of concern where the foundation is on soft seabed materials, or at deepwater mound structures where the high mound can settle significantly. The latter case is also a concern for the foundation of caissons on high rubble mounds.

(b) Differential settlement is a problem where it might lead to damage of roads and installations placed on the structures. Damage to joints between caissons could also be due to differential settlements.

(2) Structure settlement increases vulnerability to wave overtopping by lowering the crest level of the structure. Thus, the expected total vertical settlement during the structure service lifetime has to be estimated, and the construction crest level increased accordingly.

(3) Poor seabed materials which cause large settlement and stability problems might necessitate soil improvement by methods such as preloading, compaction, installation of drains, or soil replacement. Also, it may be possible to select the type and design of structure that gives a minimum foundation load.

(4) The consequence of foundation loading on settlement depends to a great extent on the loading time relative to the consolidation time. The following three categories can be identified:

(a) Drained loading, when the consolidation time is much less than the loading time.

(b) Undrained loading, when the consolidation time is much greater than the loading time.

(c) Partially drained loading, when the consolidation time and the loading time are of the same order of magnitude.

(5) This description of the loading corresponds to the classification given in Table VI-5-83 in Part VI-5-5-e where consolidation time is discussed.

(6) Foundation loads related to coastal structures are given as follows:

(a) Loads from the weight of structure materials or structure elements placed during the construction phases. The expected loading time would be in the range from minutes to days to months.

(b) Weight of the completed structure including permanent external loads.

(c) Loads from wave action, traffic loads, and other live loads. The loading times would be in the range from seconds to hours. The wave loads will be cyclic.

(7) Generally the permeability of stone materials and coarse sand is so large that deformation problems related to the previously listed loadings can be handled as drained problems. On the other hand, the permeability of clay is so low that the conditions will always be undrained. For fine sand and silt with

permeabilities between coarse sand and clay, it is not possible to make such general statements as each case must be examined. However, it is most likely that conditions during wave loadings will be undrained.

(8) Settlements are usually devided into immediate (instantaneous) settlement, primary consolidation settlement, and creep (also denoted secondary consolidation).

(a) Instantaneous settlement occurs rapidly almost in phase with the application of the load.

(b) Primary consolidation settlement is the deformation that occurs in saturated or partially saturated low permeability soils when the load carried by excess pore water pressure is gradually transferred to the soil skeleton with a corresponding simultaneous excess pore water dissipation.

(c) Secondary consolidation settlement is a long-term creep phenomenon due to shear. It might continue for a long time after completion of primary consolidation.

(9) All three settlement components are relevant to low permeability materials, whereas only immediate and secondary consolidation settlements occur with high permeability materials with drained soil conditions.

(10) The starting point in calculation of settlement of the seabed soils is understanding the in situ stress distributions just after the loading is applied and estimating the relationship between stresses and soil deformations. The in situ stress distributions are generally calculated assuming elastic material and using methods such as the procedure given by Steinbrenner (1936) or by means of the influence diagrams by Newark (1942). The empirical 2:1 load spreading method might also be used. It should be noted that fill material used for rubble-mound structures is completely flexible whereas a caisson constitutes a stiff footing.

(11) Instantaneous settlement is estimated from the deformation moduli determined either by laboratory experiments with representative small soil specimens or by in situ tests such as plate loading tests, pressuremeter tests, or other standard test procedures.

(12) Primary consolidation settlement is generally determined from consolidation theory by the use of the oedometer modulus and the permeability. During the construction phase, the load on the foundation is time-varying. Because the consolidation due to every load increment proceeds independently of the preceding load increment, the total settlement can be computed by superposition. Consolidation and the related settlement within the structure lifetime are caused almost entirely by the weight of the structure. Occasional loading from waves and other live loads can normally be disregarded in this context except where the wave-generated cyclic loadings cause significant volume changes of the soil (see Part VI-5-5-e).

(13) Secondary settlement of seabed soils is difficult to estimate. It will usually be much smaller than the sum of the instantaneous and the primary consolidation settlements.

(14) Mound material such as quarrystones and quarry-run used for the construction of rubble-mound breakwaters is usually tipped from dumpers or barges. Most of the anticipated settlement takes place during the construction phase, especially if heavy vehicles such as dumpers pass over the already placed material. Settlement will then typically be in the order of 2 - 5 percent of the height of the mound. High quarrystone foundations for caisson breakwaters might need compaction to reduce the risk of unacceptable differential settlements.

VI-5-6. Scour and Scour Protection

Any coastal project built on erodible sand or soil may be susceptible to damage resulting from scour. This section describes scour problems that affect coastal projects, gives procedures for estimating maximum depth of scour for specific situations, and presents design guidance for scour protection. The available scour prediction methods presented here assume the erodible bed is composed of noncohesive sediment.

a. Scour problems in coastal engineering. In the most general definition, scour is the erosive force of moving water. This broad definition of scour includes any erosion of sediment under any circumstances, such as beach profile change and inlet channel migration. A more specific definition of scour is used in reference to coastal engineering projects: Scour is the removal by hydrodynamic forces of granular bed material in the vicinity of coastal structures. This definition distinguishes scour from the more general erosion; and as might be expected, the presence of a coastal structure most definitely contributes to the cause of scour. Scour that occurs at coastal projects can lead to partial damage, or in some cases, complete failure of all or portions of the structure. Scour-induced damage happens at sloping-front structures when scour undermines the toe so it can no longer support the armor layer, which then slides downslope (see Figure VI-2-37). Scour impacts vertical-front caissons and other gravity-type structures if the structure is undermined to the point of tilting as illustrated by Figure VI-2-58. Monolithic gravity seawalls can also settle and tilt as a result of scour (see Figure VI-2-64). Scour at vertical sheetpile walls can result in seaward rotation of the sheetpile toe due to pressure of the retained soil as shown by Figure VI-2-69. Coastal structure damage or failure brought about by scour impacts coastal projects in several ways including: project functionality is decreased; costs will be incurred to repair or replace the structure, and scour related damage is often difficult and expensive to repair; upland property being protected by the structure may be lost or inundated; clients and cost-sharing partners will lose confidence in the project's capability to perform as required.

(1) Physical processes of scour.

(a) Scour will occur anywhere the hydrodynamic shear stresses on the bottom are high enough to initiate sediment transport. Clear water scour occurs when bottom shear stresses are high only in a localized portion of the bed; outside the local region sediment is not moving. This occurs mostly in uniform, steady flow situations. In live bed scour bottom shear stresses over the entire bed exceed the level for incipient motion with locally higher shear stresses where greater scour occurs. An equilibrium is reached when the volume of sediment being removed from the scour hole is exactly equal to sediment being deposited in its place. Understanding the physical processes involved in scour is difficult because the shear stresses responsible for scour are developed by waves, currents, or combined waves and currents, that usually are heavily influenced by the presence of a coastal structure. Because of the distinct influence coastal structures exert on the hydrodynamics, structural aspects such as geometry, location, and physical characteristics (roughness, permeability, etc.) impact the scour process. Therefore, modifying some physical characteristic of a structure may reduce scour potential.

(b) Typical structure and hydrodynamic conditions leading to scour include the following (acting singularly or in combination):

- Localized increases in peak orbital wave velocities due to combined incident and reflected waves
- Particular structure orientations or configurations that focus wave energy and increase wave velocity or initiate wave breaking
- Structure orientations that direct currents along the structure or cause a flow acceleration near the structure

- Flow constrictions that accelerate the fluid

- Breaking wave forces that are directed downward toward the bed or that generate high levels of turbulence capable of mobilizing sediment

- Wave pressure differentials and groundwater flow that produce a "quick" condition, allowing material to be carried off by currents

- Flow separation and creation of secondary flows such as vortices

- Transitions from hard bottom to erodible bed

(c) Even if the hydrodynamic aspects of scour were fully understood, there remains the difficulty of coupling the hydrodynamics with sediment transport. Consequently, most scour prediction techniques consist of rules of thumb and fairly simplistic empirical guidance developed from laboratory and field observations.

(d) Depending on the circumstances, scour can occur rapidly over short time spans (e.g., energetic storm events), or as a gradual loss of bed material over a lengthy time span (months to years). In the short-term case sediment is probably transported primarily as suspended load, whereas bedload transport is more likely during episodes of long-term scour. Scour may be cyclic with infilling of the scour hole occurring on a regular basis as the flow hydrodynamics undergo seasonal change.

(e) Most scour holes and trenches would eventually reach a stable configuration if the same hydrodynamic conditions persisted unchanged over a sufficient time span. Such an equilibrium is more likely to occur for scour induced primarily by current regimes than by wave action. It is difficult to determine if observed scour development at a particular coastal project represents an equilibrium condition. The scour might be the result of energetic flow conditions that subsided before the full scour potential was realized. Or it is possible the scour was initially greater, and infilling of the scour hole occurred prior to measurement. Finally, there is the possibility that the observed scour is simply the partial development of an ongoing long-term scour process.

(2) Common scour problems. Common coastal engineering situations where scour may occur are illustrated on Figure VI-5-114 and described as follows.

(a) Scour at coastal inlet structures.

- Kidney-shaped scour holes are sometimes present at the tip of one or both inlet jetty structures. These scour holes are usually permanent features of the inlet structure system, but there have been instances where seasonal infilling occurs due to longshore sediment transport. In some cases scour holes have been deep enough to result in partial collapse of the jetty head, while in other cases the scour holes have resulted in no structure damage. Hughes and Kamphuis (1996) observed in movable-bed model experiments that the primary hydrodynamic process responsible for kidney-shaped scour holes appears to be flood currents rounding the jetty head and entering the channel. Sediment mobilization, rate of scour, and extent of scour are increased by wave action, particularly waves that are diffracted around the jetty tip into the navigation channel. Waves breaking across the jetty head in the absence of currents will also cause scour of a lesser magnitude (Fredsøe and Sumer 1997).

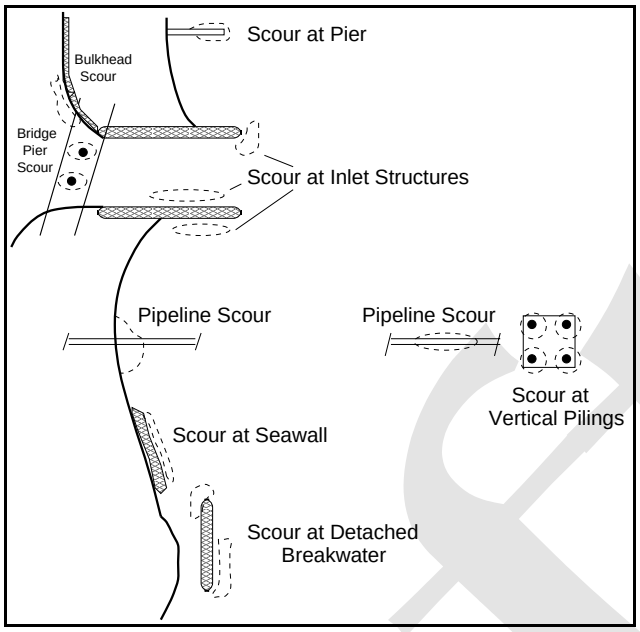

Figure VI-5-114. Coastal scour problems

- Substantial scour trenches are known to form along the channel-side toes of jetty structures. These trenches are caused either by migration of the navigation channel (by unknown causes) to a position adjacent to the jetty toe or by ebb-flow currents that are redirected by the jetty structure. Hughes and Kamphuis (1996) argued that ebb flows deflected by a jetty are analogous to plane jet flow exiting a nozzle with similar geometry. As the flow cross section decreases, the flow velocity increases proportionately to maintain the ebb flow discharge.

- Scour trenches can also form along the outside toe of the updrift jetty. These trenches might be formed by the seaward deflection of longshore currents that causes a local flow acceleration adjacent to the jetty toe, or the scour may stem from high peak orbital velocities resulting from the interaction of obliquely incident and reflected waves. A likely scenario is scour hole formation due to both hydrodynamic processes with the waves mobilizing sediment and the current transporting the material seaward. Scour trenches on the outside toe of a jetty may be seasonal at locations experiencing seasonal reversal of predominant wave direction.

- Scour holes occur regularly around bridge pilings and piers that span coastal inlets. Generally, this situation is similar to scour that plagues bridge piers on inland waterways. Additional factors complicating scour at inlet bridge piers are the unsteady and reversing nature of tidal flows, and the possible exposure to waves and storm surges.

(b) Scour at structures in deeper water.

- Scour can occur at the toes of vertical-faced breakwaters and caissons placed in deeper water. Wave-induced scour results from high peak orbital velocities developed by the interaction of incident and reflected waves. If a particular structure orientation results in increased currents along the structure toe, scour potential will be significantly enhanced. Localized liquefaction due to wave pressure differentials and excess pore pressure within the sediment may cause sediment to be removed by reduced levels of bottom fluid shear stress.

- Characteristic scour patterns may occur around the vertical supporting legs (usually cylinders) of offshore platforms. Under slowly-varying boundary layer flow conditions, the platform leg interrupts the flow causing formation of a horseshoe vortex wrapped around the structure just above the bed. This secondary flow intensifies the bottom fluid shear stresses, and erodes sediment. The quasi-equilibrium scour hole closely resembles the shape of the horseshoe vortex. In the absence of currents, waves can cause scour in the shape of an inverted, truncated cone around the vertical cylinder provided the bottom orbital velocities are sufficiently high.

- Pipelines laid on the sea bottom are susceptible to scour action because the pipe cross section obstructs the fluid particle motion developed by waves and currents.

(c) Scour at structures in shallow water.

- Piers and pile-supported structures in shallow water react to currents and waves just as in deep water. However, the shallow depth means that orbital velocities from shorter period waves can cause scour. Therefore, vertical piles are vulnerable to scour caused by a wider range of wave periods than in deeper water.

- Scour can occur along the seaward toe of detached breakwaters due to wave reflection. The scour process will be enhanced in the presence of transporting currents moving along the breakwater. Scour holes may be formed at the ends of the breakwater by diffracted waves. In shallow water, breaking waves can create high turbulence levels at the structure toe.

- Vertical-front and sloping-front seawall and revetments located in the vicinity of the shoreline can be exposed to energetic breaking waves that produce downward-directed flows and high levels of turbulence which will scour the bed. Scour could also be produced by flows associated with wave downwash at less permeable sloping structures.

- Vertical bulkheads are usually not exposed to waves capable of producing scour; however, it is possible for scour to occur by local current accelerations.

- Scour around pipelines will occur by the same mechanisms as in deeper water with shorter period waves becoming more influential as water depth decreases. Buried pipelines traversing the surfzone can be at risk if beach profile erosion exposes the pipeline to pounding wave action and strong longshore currents.

- Depending on specific design details, coastal outfalls may develop scour patterns that jeopardize the structure.

(d) Other occurrences of scour.

- Any type of flow constriction caused by coastal projects has the potential to cause scour. For example, longshore currents passing through the gap between a jetty and a detached breakwater at Ventura Harbor, CA, accelerated and caused scour along the leeside toe of the detached breakwater (Hughes and Schwichtenberg 1998).

- Storm surge barriers, sills, and other structures founded on the sea floor can experience scour at the downstream edge of the structure. Small pad foundations can be undermined by waves and currents.

- Structure transition points and termination points may produce local flow accelerations or may focus wave energy in such a way that scour occurs.

- Scour may occur as a transient adjustment to new construction. For example, Lillycrop and Hughes (1993) documented scour that occurred during construction of the terminal groin at Oregon Inlet, North Carolina. Despite maintenance of a scour blanket in advance of construction, the project required 50 percent more stone because of the scour.

b. Prediction of scour. There have been many theoretical and laboratory studies conducted examining various aspects of scour related to coastal projects. Some studies focussed on discovering the physical mechanisms responsible for scour, whereas other studies were directed at developing engineering methods for predicting the location and maximum depth of scour. In the following sections usable engineering prediction methods are presented for estimating scour for specific coastal structure configurations and hydrodynamic conditions. To a large extent the predictive equations have been empirically derived from results of small-scale laboratory tests, and often the guidance is fairly primitive. In some situations the only predictive capability consists of established rules of thumb based on experience and field observation. A comprehensive discussion of scour mechanisms, theoretical developments, and experiment descriptions is well beyond the scope of this manual. However, there are several publications containing detailed overviews of scour knowledge for many situations of interest to coastal engineers (e.g., Hoffmans and Verheij 1997; Herbich 1991; and Sumer and Fredsøe 1998a). In the following sections, appropriate citations of the technical literature are provided for more in-depth study.

(1) Scour at vertical walls. Occurrence of scour in front of vertical walls can be conveniently divided into two cases: nonbreaking waves being reflected by a vertical wall, and breaking waves impacting on a vertical wall. In either case, waves can approach normal to the wall or at an oblique angle.

(a) Nonbreaking waves. Nonbreaking waves are more prevalent on vertical-front structures located in deeper water and at bulkhead structures located in harbor areas. Almost all the energy in incident waves reaching a vertical-front structure is reflected unless the structure is porous. Close to the structure, strong phase locking exists between incident and reflected waves, and this sets up a standing wave field with amplified horizontal particle velocities beneath the water surface nodes and minimal horizontal velocities beneath the antinodes. The bottom sediment responds to the fluid velocities by eroding sediment where bottom shear stresses are high and depositing where stresses are low.

- Normally incident nonbreaking waves. Researchers have identified two characteristic scour patterns associated with nonbreaking waves reflected by a vertical wall (de Best, Bijker, and Wichers 1971; Xie 1981; Irie and Nadaoka 1984; Xie 1985). Fine sand is transported primarily in suspension, and in this case scour occurs at the nodes of the sea surface elevation with deposition occurring at the antinodes. Coarse sediment is moved primarily as bed load so that scour occurs midway between the sea surface nodes and antinodes with deposition usually centered on the nodes of the standing wave pattern.

- Uniform, regular waves produce a repeating pattern of scour and deposition as a function of distance from the toe of the vertical wall as illustrated in the upper portion of Figure VI-5-115. For fine sand maximum scour nearest the wall occurs a distance $L/4$ from the wall where L is the wavelength of the incident wave. Irregular waves produce a similar scour pattern for fine sand as shown in the lower portion of Figure VI-5-115. However, phase-locking between incident and reflected irregular waves decreases with distance from the wall with the maximum scour depth for fine sand approximately located a distance $L_p/4$ from the vertical wall, where L_p is the wavelength associated with the peak spectral frequency using linear wave theory.

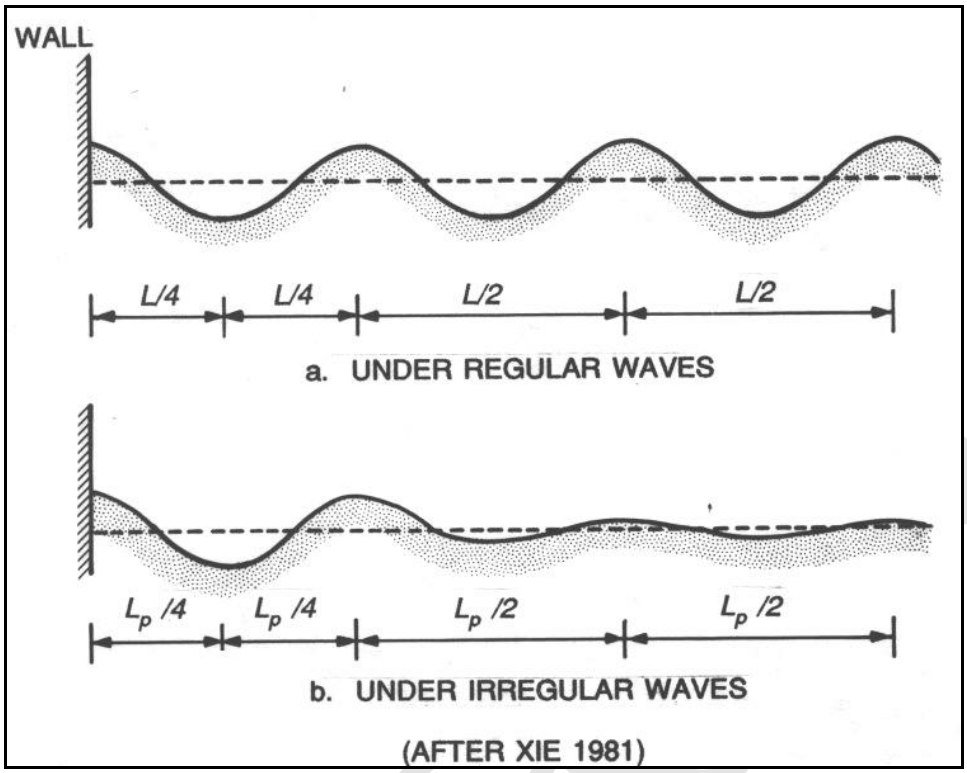

Figure VI-5-115. Regular and irregular wave-scoured profiles at a vertical-front structure

- Based on results from 12 movable-bed model tests, Xie (1981, 1985) proposed an empirically-based equation to estimate maximum scour for normally incident, nonbreaking, regular waves incident upon an impermeable vertical wall. The equation was given as:

$$\frac{S_m}{H} = \frac{0.4}{[\sinh(kh)]^{1.35}} \tag{VI-5-253}$$

where

S_m = maximum scour depth at node ($L/4$ from wall)

H = incident regular wave height

h = water depth

k = incident regular wave number ($k = 2\pi/L$)

L = incident regular wavelength

- A similar laboratory-based prediction empirical equation for the more appropriate case of normally incident, nonbreaking irregular waves was given by Hughes and Fowler (1991) as

$$\frac{S_m}{(u_{rms})_m \; T_p} = \frac{0.05}{[\sinh(k_p h)]^{0.35}} \tag{VI-5-254}$$

where

T_p = wave period of the spectral peak

k_p = wave number associated with the spectral peak by linear wave theory

$(u_{rms})_m$ = root-mean-square of horizontal bottom velocity

- The value of $(u_{rms})_m$ was given by Hughes (1992) as

$$\frac{(u_{rms})_m}{g\ k_p T_p H_{mo}} = \frac{\sqrt{2}}{4\pi\ \cosh(k_p h)}\left[0.54\ \cosh\left(\frac{1.5\ -\ k_p h}{2.8}\right)\right] \qquad \text{(VI-5-255)}$$

where H_{mo} is the zeroth-moment wave height, and g is gravity. (Equation VI-5-255 is empirically based and should not be applied outside the range $0.05 < k_p h < 3.0$.)

- Equation VI-5-255 is plotted on Figure VI-5-116 along with the movable-bed model experiment results. The dashed line is an equivalent to Equation VI-5-254. Scour predicted for irregular waves is significantly less than scour predicted for regular waves, and in many cases the predicted maximum scour does not represent a threat to the structure toe due to its location $L_p/4$ from the wall. Also, any effect related to sediment size is missing from these formulations (other than the stipulation of fine sand). Therefore, sediment scale effects may have influenced laboratory results causing less scour than might occur at full scale.

- The relatively minor scour depths predicted for nonbreaking waves may be a direct result of scale effects or it may be related to the two-dimensionality of the laboratory experiments. In the wave flume an equilibrium profile is reached even though sediment is still constantly in motion. At an actual project site strong currents running parallel to a vertical-front structure could remove sediment put into motion by the standing wave pattern. If this occurs, scour will continue until a new live-bed equilibrium is reached. Sato, Tanaka, and Irie (1968) gave field examples of scour attributed to along-structure currents acting in conjunction with bed agitation by waves. Unfortunately, there are no scour prediction methods covering this possibility.

- Obliquely incident nonbreaking waves. Obliquely approaching incident nonbreaking waves will also be nearly completely reflected by a vertical wall. The resulting combined incident and reflected waves resemble a short-crested, diamond pattern that propagates in a direction parallel to the wall. (See Hsu (1991) for development of theories related to obliquely reflected long-crested waves.) Just as in the case of normal wave incidence, partial nodes and antinodes develop on lines parallel to the structure at distances that are a function of the wave properties and incident wave angle. However, obliquely reflected waves also generate a mass transport component parallel to the vertical structure which may contribute to enhanced scour along the structure. Silvester (1991) summarized laboratory results of scour at highly reflective (but not necessarily vertical-front) structures caused by obliquely incident long-crested regular and irregular waves. It was observed that obliquely incident waves tended to scour more than equivalent normally incident waves, and irregular waves scour at a slower rate and somewhat more uniformly than regular waves. No engineering methods are presently available to estimate scour caused by obliquely incident, nonbreaking irregular waves reflected by a vertical wall.

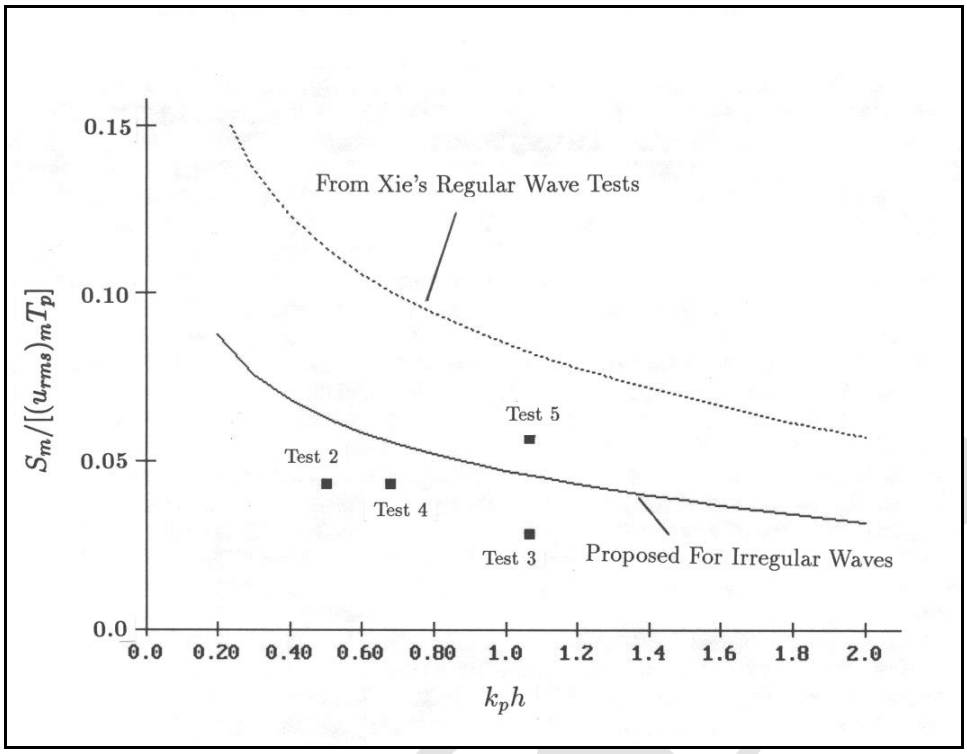

Figure VI-5-116. Scour prediction for nonbreaking waves at vertical wall (Hughes and Fowler 1991)

- Scour at the head of a vertical breakwater. Sumer and Fredsøe (1997) conducted small-scale movable-bed experiments to investigate scour around the circular head of a vertical breakwater aligned parallel to the wave crests. They discovered that scour around the breakwater head is due mainly to the lee-wake vortices, similar to wave-induced scour at vertical piles. Maximum scour depths from different sized breakwaters corresponded remarkably well with the associated Keulegan-Carpenter number, which is defined as

$$KC = \frac{U_m T}{B} \tag{VI-5-256}$$

where

U_m = maximum wave orbital velocity at the bed (in the absence of a structure)

T = regular wave period

B = diameter of the vertical breakwater circular head

- Sumer and Fredsøe presented the following empirical equation to predict maximum scour depth (S_m) as a function of the Keulegan-Carpenter number and diameter of the breakwater head:

$$\frac{S_m}{B} = 0.5\ C_u \left[1 - e^{-0.175\ (KC-1)} \right] \quad \text{(VI-5-257)}$$

in which C_u is an uncertainty factor with a mean value of unity and a standard deviation of $\sigma_u = 0.6$. This empirical expression was developed for the data range $0 < KC < 10$. However, beyond $KC = 2.5$, data from only one breakwater diameter were used. Irregular waves will probably not scour as deeply, so the empirical equation could be considered conservative.

- Sumer and Fredsøe (1997) also investigated scour at the heads of squared-ended vertical breakwaters, perhaps representative of caissons. They found similar planform extent of scour, but depth of scour was greater by about a factor of 2. No empirical design equation was given for this situation, but it is possible to make estimates directly from the curve in their paper or from the simple equation

$$\frac{S_m}{B} = -0.09 + 0.123\ KC \quad \text{(VI-5-258)}$$

which fits the data reasonably well. However, this expression is based on very limited laboratory data, and scour estimates should be considered tentative.

- The angle of obliquely incident waves on scour around the vertical breakwater head was also shown to be a factor in scour magnitude, and the addition of even small currents moving in the direction of wave propagation significantly increased depth of scour. No design guidance was suggested that included currents and wave angle. Sumer and Fredsøe analyzed scale effects in their laboratory experiments and concluded that scour holes at full scale will be slightly smaller than equivalent scaled-up model results. Design of scour protection for vertical breakwater heads is discussed in Part VI-5-6-c, "Design of scour protection."

(b) Breaking waves. Scour caused by waves breaking on vertical-front structures has been a topic of numerous studies. (See Powell 1987; Kraus 1988; and Kraus and McDougal 1996 for overviews of the literature.) Scour caused by breaking waves is generally greater than for nonbreaking waves, and there is more likelihood of scour leading to structure damage. Spilling or plunging breaking waves can break directly on the vertical wall or just before reaching the wall. The physical mechanisms responsible for scour by breaking waves are not well understood, but it is generally thought that the breaking process creates strong downward directed flows that scour the bed at the base of the wall. For example, the re-entrant tongue of a plunging wave breaking before it reaches the structure generates a strong vortex motion that will mobilize sediment at the toe. A wave impacting directly on the vertical face will direct water down at the toe in the form of a jet. Sediment mobilization and transport is dominated by turbulent fluid motions rather than fluid shear stresses, and air entrained in the breaking wave also influences the erosion process (Oumeraci 1994). Figure VI-5-117 illustrates scour and profile change fronting a vertical seawall.

- Rules of thumb. There are several accepted rules-of-thumb pertaining to scour of noncohesive sediment at vertical walls. For the case of normally incident breaking waves with no currents:

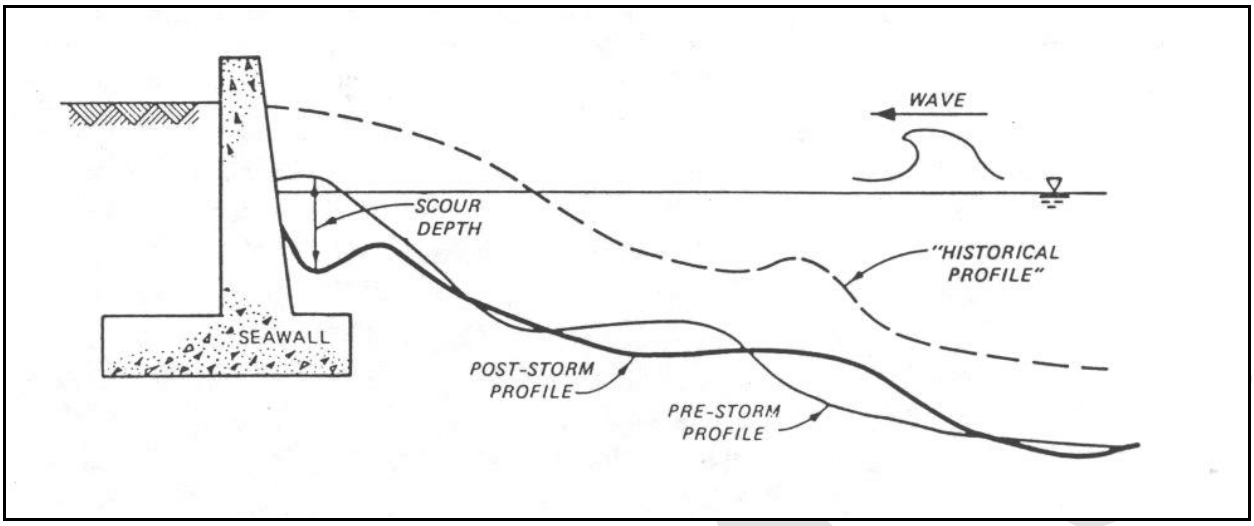

Figure VI-5-117. Scour due to breaking waves at a vertical seawall (Kraus 1988)

- The maximum scour depth at a vertical wall (S_m) is approximately equal to the nonbreaking wave height (H_{max}) that can be supported by the water depth (h) at the structure, i.e.,

$$S_m = H_{\max} \qquad or \qquad S_m \approx h \tag{VI-5-259}$$

- Maximum scour occurs when the vertical wall is located around the plunge point of the breaking wave.

- Reducing the wall reflection reduces the amount of scour.

• Irregular breaking wave scour prediction. Predictive equations for estimating maximum scour at vertical walls due to normally incident regular breaking waves were proposed by Herbich and Ko (1968) and Song and Schiller (1973). Powell (1987) discussed shortcomings of these two methods and concluded the empirical equations were not useful for design purposes.

- Fowler (1992) also examined the Song and Schiller relationship using data from midscale movable-bed model tests using irregular waves, and reasonable correspondence was noted between measurements and predictions. Fowler then combined his irregular wave scour data with regular wave data from Barnett and Wang (1988) and from Chesnutt and Schiller (1971) as shown in Figure VI-5-118.

- The following empirical equation (solid line on Figure VI-5-118) was proposed for estimating maximum scour of noncohesive sediment due to normally incident breaking irregular waves with a mild approach slope.

$$\frac{S_m}{(H_{mo})_o} = \sqrt{22.72 \frac{h}{(L_p)_o} + 0.25} \tag{VI-5-260}$$

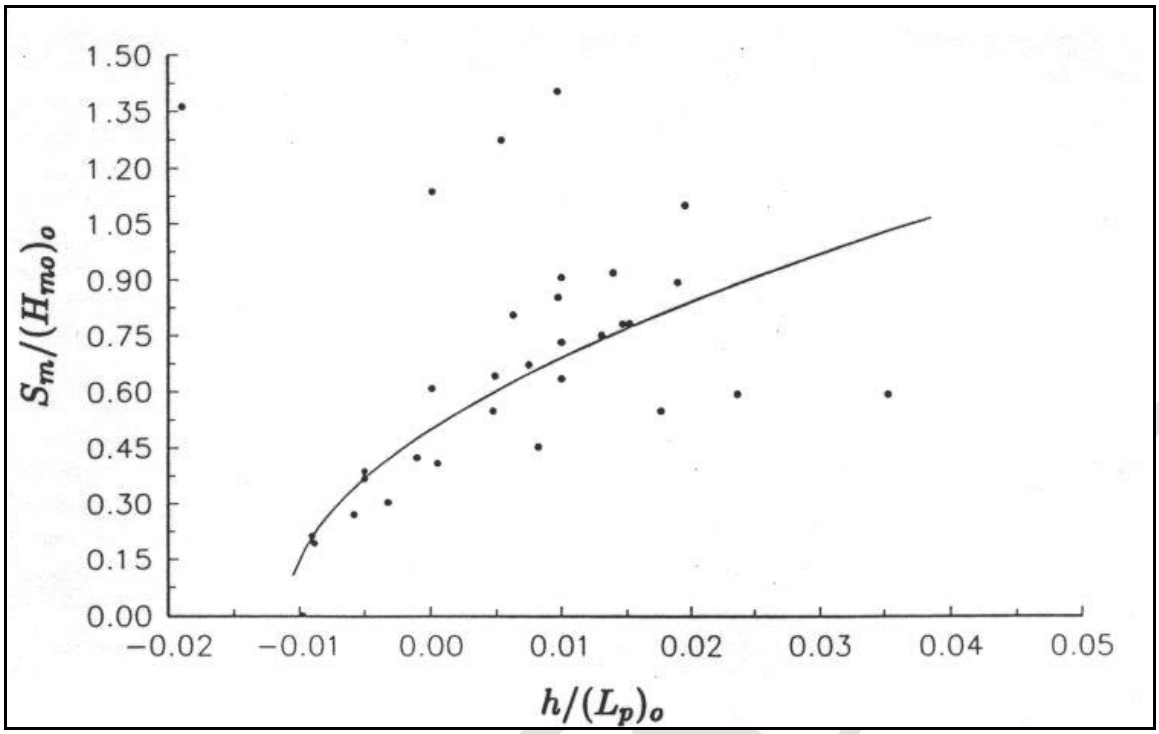

Figure VI-5-118. Relative scour depth as a function of relative depth at a vertical wall (Fowler 1992)

where

S_m = maximum scour depth

$(H_{mo})_o$ = zeroth-moment wave height in deep water

h = pre-scour water depth at the vertical wall

$(L_p)_o$ = deepwater wavelength associated with the peak spectral wave period, T_p, i.e., $(L_p)_o = (g/2\pi)\ T_p^2$

- Fowler noted that application of this empirical equation is limited by the data to values of relative depth and relative steepness within the ranges

$$0.011 < \frac{h}{(L_p)_o} < 0.045 \qquad \textit{and} \qquad 0.015 < \frac{(H_{mo})_o}{(L_p)_o} < 0.040 \tag{VI-5-261}$$

- Fowler's predictive equation does not include any parameters relating to sediment properties, which are expected to have some influence in the scouring process. However, sediment transport induced by waves breaking against a vertical wall will not be very dependent on Shields parameter due to the turbulent nature of the entraining flow, and this would decrease the influence of sediment grain size. Also, the previous scour estimation method assumes no current flow along the vertical wall.

- Scour of cobble (or shingle) beaches fronting vertical walls is discussed by Carpenter and Powell (1998). They provided dimensionless design graphs to predict maximum scour depth as a function of significant wave height, wave steepness, and local water depth. Their results were based on laboratory movable-bed model tests, which were correctly scaled due to the relatively large size of cobbles compared to sand.

(2) Scour at sloping structures. Scour at the toe of sloping-front structures is thought to be a function of structure slope and porosity, incident wave conditions, water depth, and sediment grain-size. Despite considerable research into the processes responsible for wave-induced scour at sloping structures, there are no generally accepted techniques for estimating maximum scour depth or planform extent of scour (Powell 1987; Fowler 1993). However, progress is being made in development of numerical models to predict scour at sloping-front structures. Engineering use of such numerical models should consider model input requirements, representation of structure characteristics (particularly reflection parameters), and documented validation against field or laboratory experiments conducted at larger scales. Nonbreaking irregular waves impinging on a sloping structure will create a standing wave field similar to a vertical structure except the variation between the sea surface elevation nodes and antinodes is less pronounced, and the location of the node nearest the structure toe varies with wave condition and structure reflection properties (Hughes and Fowler 1995; O'Donoghue and Goldsworthy 1995; Losada, Silva, and Losada 1997). Erosion of fine sediment is expected to occur at the nodal location, but no empirical estimation method has been proposed.

(a) Rules of thumb. In lieu of easily applied semi-empirical scour estimation tools, simple rules-of-thumb serve as engineering guidelines for scour at sloping-front structures.

- Maximum scour at the toe of a sloping structure is expected to be somewhat less than scour calculated for a vertical wall at the same location and under the same wave condition. Therefore, a conservative scour estimate is provided by the vertical wall scour prediction equations, i.e., $S_m < H_{max}$.

- Depth of scour decreases with structure reflection coefficient. Therefore, structures with milder slopes and greater porosity will experience less wave-induced scour.

- Scour depths are significantly increased when along-structure currents act in conjunction with waves.

- Obliquely incident waves may cause greater scour than normally incident waves because the short-crested waves increase in size along the structure (Lin et al. 1986) due to the mach-stem effect. Also, oblique waves generate flows parallel to the structure.

(b) Scour at head of sloping breakwater. Fredsøe and Sumer (1997) conducted small-scale movable-bed model experiments to investigate mechanisms responsible for wave-induced scour around the conical heads of sloping-front breakwater structures. The experiments were similar in many respects to the companion study of scour at the ends of vertical breakwaters (Sumer and Fredsøe 1997). For most tests the rubble-mound breakwater head was approximated as an impermeable, smooth structure constructed of steel frames covered with sheet metal and having a slope of 1:1.5. The breakwater head was aligned parallel to the incident irregular waves. Observed scour was attributed to two different mechanisms; steady streaming of flow around the breakwater head, and waves breaking across the breakwater head and impinging on the leeside bed.

- Scour holes caused by steady streaming formed at the breakwater toe on the seaward curve of the breakwater head. An estimation of maximum scour depth (S_m) was developed as a function of the Keulegan-Carpenter number (KC) and given by Fredsøe and Sumer (1997) as

$$\frac{S_m}{B} = 0.04\ C_u \left[1 - e^{-4.0\ (KC - 0.05)} \right] \qquad \text{(VI-5-262)}$$

in which C_u is an uncertainty factor with a mean value of unity and a standard deviation of $\sigma_u = 0.2$. The Keulegan-Carpenter number is calculated as given by Equation VI-5-256 using the peak spectral wave period, T_p, as the period, T, and the breakwater head diameter at the bed as B.

- Fredsøe and Sumer suggested that U_m be calculated from linear wave theory as the bottom velocity found using a wave height of

$$H = \frac{1}{\sqrt{2}} H_s \tag{VI-5-263}$$

where H_s is the significant wave height. A similar expression for predicting deposition was also presented.

- The second scour mechanism is caused by waves breaking across the sloping front of the breakwater head. The geometry of the steep breakwater face causes lateral water motion that forms the tongue of the plunging breaker into a rounded re-entrant jet that impacts the bed at a steep angle and mobilizes sediment. This creates a scour hole at the breakwater toe on the leeside of the rounded head with the maximum depth located approximately at the intersection of breakwater head and trunk. Fredsøe and Sumer presented the following empirical equation for maximum scour depth (S_m) due to plunging breaking waves

$$\frac{S_m}{H_s} = 0.01\ C_u \left(\frac{T_p \sqrt{g\ H_s}}{h} \right)^{3/2} \tag{VI-5-264}$$

where C_u is an uncertainty factor with a mean value of unity and a standard deviation of $\sigma_u = 0.34$, h is water depth, and the other parameters are as defined previously.

- As noted by Fredsøe and Sumer, these equations were developed for impermeable, smooth breakwater heads. The permeability and roughness of rubble-mound breakwaters will effectively decrease both scour mechanisms, thus scour estimates may be somewhat conservative. The previous empirical expressions for predicting maximum scour depths are based on a limited number of data points derived primarily from laboratory experiments, and the equations should be considered tentative until additional studies are conducted. Also, scour is caused by waves only; superimposed currents are expected to increase appreciably maximum scour depth. Design of scour protection for sloping-front breakwater heads is discussed in Section VI-5-6-c, "Design of scour protection."

(3) Scour at piles. The majority of methods for estimating scour at vertical piles were developed for piles with circular cross section, which are widely used in coastal and offshore engineering applications. However, there are estimation techniques for piles with noncircular cross sections and for specialized structures such as noncircular bridge piers and large bottom-resting structures. Scour at small vertical piles (pile diameter, D, is less than one-tenth of the incident wavelength) is caused by three simultaneously acting mechanisms: formation of a horseshoe-shaped vortex wrapped around the front of the pile; vortex shedding in the lee of the pile; and local flow accelerations due to streamline convergence around the pile. The pile does not significantly affect the incident wave. Large diameter piles, in which the diameter is greater than one-tenth of the incident wavelength, do have an impact on the incident waves which are reflected by the pile and diffracted around the pile. The key parameters governing scour formation appear to be current magnitude, orbital wave velocity, and pile diameter. Less important parameters are sediment size and pile shape (if the

pile has noncircular cross section). For detailed descriptions of the physical mechanisms responsible for scour at vertical piles see Niedoroda and Dalton (1986) or some of the following references.
A general, and somewhat conservative, rule-of-thumb is: Maximum depth of scour at a vertical pile is equal to twice the pile diameter. This rule-of-thumb appears to be valid for most cases of combined waves and currents. Smaller maximum scour depths are predicted by the equations in the following sections. Estimation formulas for maximum scour depth have been proposed for the cases of currents only, waves only, and combined waves and currents. The flow problem and associated sediment transport are beyond a complete theoretical formulation, and even numerical modeling attempts have not been able to describe fully the scour process at vertical piles (see Sumer and Fredsøe 1998a for a summary of numerical modeling approaches).

(a) Scour at small diameter vertical piles. Vertical piles with diameter, *D,* less than one-tenth of the incident wavelength constitute the vast majority of pile applications in coastal engineering. Even cylindrical legs of some offshore oil platforms may fall into this category.

- Pile scour by currents. Many scour estimation formulas have been proposed for scour caused by unidirectional currents without the added influence of waves. A formulation widely used in the United States is the Colorado State University (CSU) equation developed for bridge piers (e.g., Richardson and Davis 1995) given by the expression

$$\frac{S_m}{h} = 2.0\ K_1\ K_2 \left(\frac{b}{h}\right)^{0.65} F_r^{0.43} \qquad \text{(VI-5-265)}$$

where

S_m = maximum scour depth below the average bottom elevation

h = water depth upstream of the pile

b = pile width

F_r = flow Froude number [$F_r = U/(gh)^{1/2}$]

U = mean current velocity magnitude

K_1 = pile shape factor

K_2 = pile orientation factor

- Equation (VI-5-265) is a deterministic formula applicable for both clear water scour and live bed scour, and it represents a conservative envelope to the data used to establish the empirical coefficients. The shape factor, K_1, is selected from Figure VI-5-119, and the orientation factor, K_2, can be determined from the following equation given by Froehlich (1988).

$$K_2 = (\cos\ \theta + \frac{L}{b} \sin\ \theta)^{0.62} \qquad \text{(VI-5-266)}$$

where L/b is defined in Figure VI-5-119 and θ is the angle of pile orientation. K_2 equals unity for cylindrical piles. Other modifying factors have been proposed to account for sediment gradation and bed forms, but these factors have not been well established. An additional factor is available for use when piles are clustered closely together. See Richardson and Davis (1995) and Hoffmans and Verheij (1997) for details.

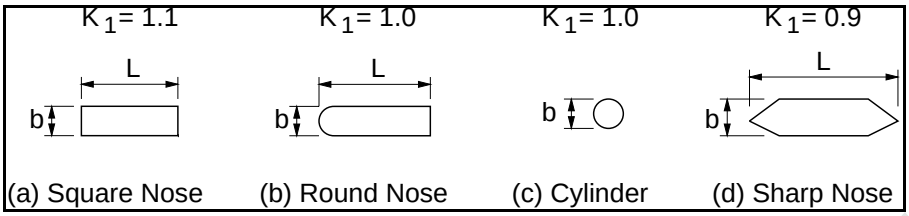

Figure VI-5-119. Correction factor, K_1, for pile/pier shape

- Johnson (1995) tested seven of the more commonly used scour prediction equations against field data and found that the CSU equation (Equation VI-5-265) produced the best results for $h/b > 1.5$. At lower values of h/b a different empirical formulation offered by Breusers, Nicollet, and Shen (1977) provided better results.

- Johnson (1992) developed a modified version of the CSU empirical equation for use in reliability analysis of failure risk due to scour at cylindrical piles. Her formula represents a best-fit to the data rather than a conservative envelope. An application example is included in her 1992 paper.

• Pile scour by waves. The physical processes associated with wave-only scour around vertical piles are reasonably well described qualitatively (See Sumer and Fredsøe (1998a) for a comprehensive review and listing of many references.)

- In an earlier paper Sumer, Christiansen, and Fredsoe (1992a) established an empirical equation to estimate scour at a vertical pile under live bed conditions. They used small- and large-scale wave flume experiments with regular waves, two different sediment grain sizes, and six different circular pile diameters ranging from 10 cm to 200 cm. Maximum scour depth (S_m) was found to depend only on pile diameter and Keulegan-Carpenter number (KC), as expressed by Equation VI-5-256 with pile diameter, D, as the denominator. The experimental data of Sumer, Christiansen, and Fredsoe (1992a) are shown plotted in Figure VI-5-120, and the solid line is the predictive equation given by

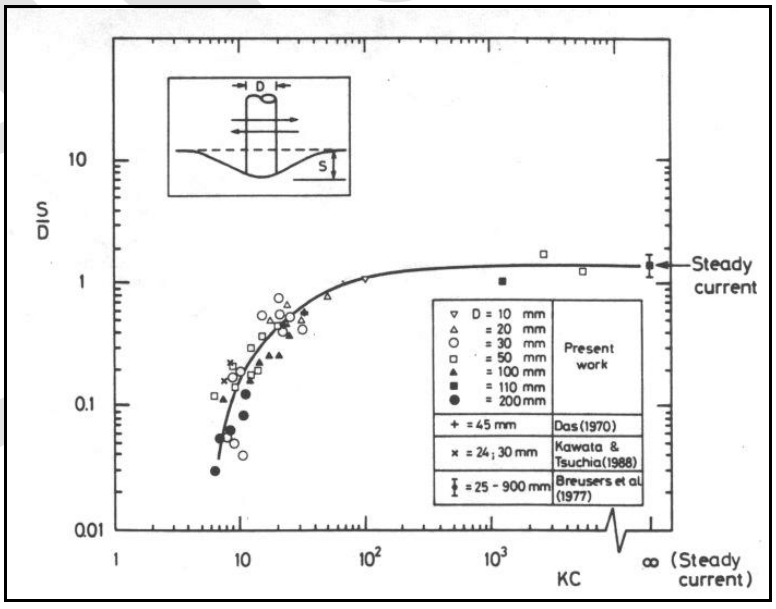

Figure VI-5-120. Wave-induced equilibrium scour depth at a vertical pile

$$\frac{S_m}{D} = 1.3 \left[1 - e^{-0.03\ (KC-6)} \right] \qquad \text{(VI-5-267)}$$

where D is cylindrical pile diameter. No live-bed scour occurs below values of KC=6, which corresponds to onset of horseshoe vortex development. At values of $KC > 100$, $S_m/D \rightarrow 1.3$, representing the case of current-only scour.

- Independent confirmation of Equation VI-5-267 was presented by Kobayashi and Oda (1994) who conducted clear water scour experiments. They stated that maximum scour depth appeared to be independent of Shields parameter, grain size diameter, and whether scour is clear-water or live-bed.

- In an extension to their 1992 study, Sumer, Christiansen, and Fredsoe (1993) conducted additional regular wave live-bed scour experiments using square piles oriented with the flat face 90 deg and 45 deg to the waves. The following empirical equations for maximum scour were obtained as best-fits to the observed results:

Square pile 90 deg to flow:

$$\frac{S_m}{D} = 2.0 \left[1 - e^{-0.015\ (KC-11)} \right] \qquad for\ KC \geq 11 \qquad \text{(VI-5-268)}$$

Square pile 45 deg to flow:

$$\frac{S_m}{D} = 2.0 \left[1 - e^{-0.019\ (KC-3)} \right] \qquad for\ KC \geq 3 \qquad \text{(VI-5-269)}$$

- Scour for the square pile oriented at 45 deg begins at lower values of KC, but the maximum scour at large KC values approaches $S_m/D = 2$ regardless of orientation.

- Studies on the time rate of scour development were reported by Sumer, Christiansen, and Fredsoe (1992b), Sumer et al. (1993), and Kobayashi and Oda (1994). Recent research on wave scour around a group of piles was summarized by Sumer and Fredsøe (1998a, 1998b).

- Pile scour by waves and currents. Kawata and Tsuchiya (1988) noted that local scour depths around a vertical pile were relatively minor compared to scour that occurs when even a small steady current is added to the waves. Eadie and Herbich (1986) conducted small-scale laboratory tests of scour on a cylindrical pile using co-directional currents and irregular waves. They reported the rate of scour was increased by adding wave action to the current, and the maximum scour depth was approximately 10 percent greater than what occurred with only steady currents. This latter conclusion contradicts Bijker and de Bruyn (1988) who found that nonbreaking waves added to steady currents slightly decreased ultimate scour depth whereas adding breaking waves caused increased scour to occur. Eadie and Herbich also noted that the inverted cone shape of the scour hole was similar with or without wave action, and the use of irregular versus regular waves appeared to influence only scour hole geometry and not maximum scour depth. They developed a predictive equation using results from approximately 50 laboratory experiments, but no wave parameters were included in the formulation. Finally, they pointed out that their conclusions may hinge on the fact that the steady current magnitude exceeded the maximum bottom wave orbital velocity, and different results may occur with weak steady currents and energetic waves.

- Earlier work by Wang and Herbich (1983) did provide predictive equations that included wave parameters along with current, pile diameter, sediment properties, and water depth. However, there

were some unanswered questions about scaling the results to prototype scale. Consequently, until further research is published, maximum scour depth due to waves and currents should be estimated using the formulations for scour due to currents alone (Equation VI-5-265).

(b) Scour at large diameter vertical piles. Rance (1980) conducted laboratory experiments of local scour at different shaped vertical piles with diameters greater than one-tenth the incident wavelength. The piles were exposed to coincident waves and currents. Rance provided estimates of maximum scour depth as functions of pile equivalent diameter, D_e, for different orientations to the principal flow direction. (D_e is the diameter of a cylindrical pile having the same cross-sectional area as the angular pile.) These formulas are given in Figure VI-5-121.

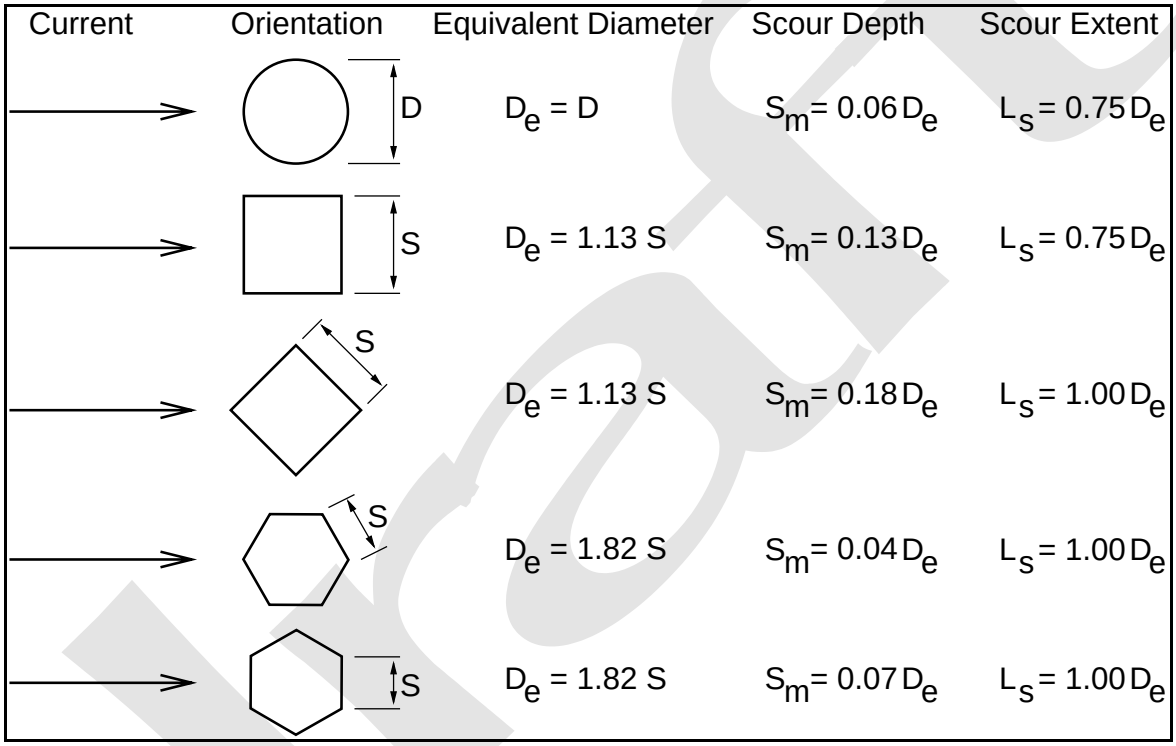

Figure VI-5-121. Wave and current scour around large vertical piles (Rance 1980)

(c) Maximum scour occurs at the corners of the square piles. Estimates of extent of scour are useful for design of scour blankets. Sumer and Fredsøe (1998a) provided additional information about flow around large piles.

(4) Scour at submerged pipelines. Waves and currents can scour material from beneath pipelines resting on the bottom, leading to partial or even complete burial of the pipeline. In most situations pipeline burial is usually considered a desirable end result. However, if the pipeline spans soil types having different degrees of erodibility, differential scour may result in sections of the pipeline being suspended between bottom hard points, and this could lead to pipeline failure. Onset of scour beneath a pipeline resting on, or slightly embedded in, the bottom occurs initially as piping when seepage beneath the pipeline increases and a mixture of sediment and water breaks through (Chiew 1990). Onset of scour is followed by a phase of rapid scour called tunnel erosion in which the bed shear stresses are increased four times above that of the undisturbed sand bed. Tunnel erosion is followed by lee-wake erosion in which the lee-wake of the pipeline appears to control the final equilibrium depth and shape of the downstream scour. Equilibrium depth of scour beneath the pipeline is usually defined as the distance between the eroded bottom and the underside of the pipeline

as illustrated on Figure VI-5-122. Overviews of pipeline scour knowledge and citations to the extensive literature are included in Sumer and Fredsøe (1992, 1998a) and Hoffmans and Verheij (1997). Only the established empirical equations for estimating scour depth are included in the following:

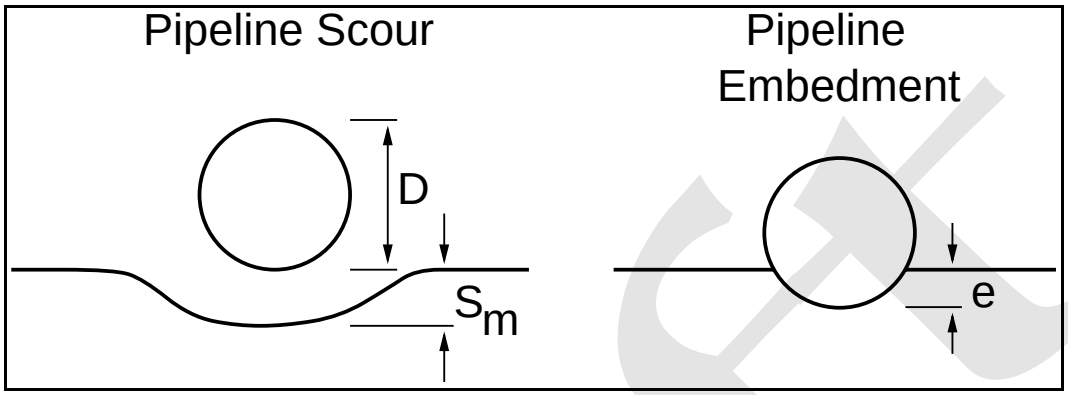

Figure VI-5-122. Pipeline scour and pipeline embedment

(a) Pipeline scour by currents. In steady currents the equilibrium scour depth beneath a pipeline is thought to be a function of pipe diameter, pipe roughness, pipe Reynolds number, and Shields parameter. For clear water scour, when mean flow velocity, U, is less than the critical velocity, U_c, maximum scour depth can be calculated using the following equation from Hoffmans and Verheij (1997)

$$\frac{S_m}{D} = \frac{\mu}{2}\left(\frac{U}{U_c}\right) \tag{VI-5-270}$$

where

$$\mu = \left(\frac{k_s}{12\ D}\right)\ln\left(\frac{6\ D}{k_s}\right) \tag{VI-5-271}$$

and

D = pipe diameter

h = water depth

U = depth averaged flow

U_c = critical depth-averaged flow velocity

k_s = effective bed roughness, $k_s = 3\ d_{90}$ (k_s must have the same units as D)

When $U/U_c > 1$, live-bed scour occurs, and in this case Sumer and Fredsøe (1992) stated that pipe Reynolds number only influences flow around smooth pipes and the influence of Shields parameter is minor. They

recommended the simple equation for predicting maximum equilibrium scour depth. The 0.1-value represents the standard deviation of the data, so a conservative estimate of scour would be S_m/D=0.7.

$$\frac{S_m}{D} = 0.6 \pm 0.1 \tag{VI-5-272}$$

(b) Pipeline scour by waves. Oscillatory bottom velocities under waves create piping conditions beneath pipelines in the same manner as steady currents. Sumer and Fredsøe (1991) gave a criterion for onset of scour under waves based on a small number of laboratory experiments. This criterion is

$$\frac{e_{cr}}{D} = 0.1 \ln(KC) \tag{VI-5-273}$$

where e_{cr} is the critical embedment (depth of pipeline burial beyond which no scour occurs), and KC is the Keulegan-Carpenter number, given by Equation VI-5-256 with D as the denominator. Scour is unlikely to occur for values of $e_{cr}/D > 0.5$ (half buried pipe). Sumer and Fredsøe (1990) studied scour beneath a bottom-resting pipeline under wave action. Their laboratory data, combined with that of an earlier researcher, indicated that live-bed scour was strongly related to Keulegan-Carpenter number and pipe diameter, while only weakly influenced by Shields parameter and pipe roughness. The data were well represented over a wide range of Keulegan-Carpenter number ($2 < KC < 300$) by the empirical expression

$$\frac{S_m}{D} = 0.1 \sqrt{KC} \tag{VI-5-274}$$

Klomb and Tonda (1995) presented a modified version of Equation VI-5-274 that included allowance for partial embedment, e, of the pipeline, i.e.,

$$\frac{S_m}{D} = 0.1 \sqrt{KC} \left(1 - 1.4 \frac{e}{D} \right) + \frac{e}{D} \tag{VI-5-275}$$

with scour depth taken relative to the undisturbed bed. Equation VI-5-275 is valid for values of $e/D < 0.5$ (Hoffmans and Verheij 1997).

(c) Pipeline scour by waves and currents. Sumer and Fredsøe (1996) conducted laboratory tests of pipeline scour due to combined waves and currents covering a range of KC from 5 to about 50 with codirectional currents. The general trend, regardless of the value of KC, was for scour depth to initially decrease as current is increased from zero. At higher values of current, maximum scour depth approaches the value given by Equation VI-5-272 for currents alone. Sumer and Fredsøe (1996) provided empirical design equations based on the laboratory experiments; but for values of KC between 40 and 50 maximum scour depth is almost the same as the estimate for currents alone.

(d) Pipelines in the nearshore. Pipelines traversing the surfzone may be damaged if exposed to breaking waves and strong longshore currents. Little design guidance is available other than the fact that additional scour will occur once the pipeline is exposed. The burial depth for a pipeline through the nearshore should

exceed in all places the expected bottom profile lowering that might occur over the life of the pipeline. This can be estimated using profile-change models or from long-term beach profile data.

(5) Other scour problems. Some coastal projects may include structural elements or hydrodynamic flow conditions that are typically associated with inland waterways or estuaries. Structures such as storm surge barriers, discharge control structures, or large pad footings may experience scour around their foundations due to currents or combined waves and currents.

(a) Hoffmans and Verheij (1997) provided a summary of techniques for estimating maximum scour for a number of situations that may be applicable to coastal projects:

- Scour downstream of sills and stone blankets due to currents.
- Scour downstream of hard bottoms due to horizontal submerged jets.
- Scour at control structures due to plunging jets.
- Scour at two- and three-dimensional culverts.
- Scour at abutments and spur dikes.

(b) See Hoffmans and Verheij (1997) for further details and associated technical literature.

c. Design of scour protection. Toe protection in the form of an apron is needed to prevent toe scour which may destabilize or otherwise decrease the functionality of a coastal structure. The apron must remain intact under wave and current forces, and it should be flexible enough to conform to an initially uneven sea floor. Scour apron width and required stone size for stability are related to wave and current intensity, bottom material, and structure characteristics such as slope, porosity, and roughness. Design guidance for scour protection is based largely on past successful field experience combined with results from small-scale laboratory tests. Special attention is needed where scour potential is enhanced such as at structure heads/ends, at transitions in structure composition, or at changes in structure alignment. This section provides general design guidance for scour aprons; however, this guidance should be considered preliminary. Projects requiring absolutely stable scour blankets should have proposed designs tested in a physical model. Hales (1980) surveyed scour protection practices in the United States and found that the minimum scour protection was typically an extension of the structure bedding layer and any filter layers. The following minimum rules-of-thumb resulted from this survey: minimum toe apron thickness - 0.6 m to 1.0 m (1.0 m to 1.5 m in northwest U.S.); minimum toe apron width - 1.5 m (3 m to 7.5 m in northwest U.S.); material - quarrystone to 0.3 m diameter, gabions, mats, etc. These rules-of-thumb are inadequate when the water depth at the toe is less than two times the maximum nonbreaking wave height at the structure or when the structure reflection coefficient is greater than 0.25 (structures with slopes greater than about 1:3). Under these more severe conditions use the scour protection methods summarized in the following sections for specific types of coastal structures.

(1) Scour protection for vertical walls.

(a) Vertical-front structures consist of large caisson-type gravity structures, gravity retaining walls, and cantilevered or anchored sheet-pile retaining walls. Toe protection design for larger vertical-front gravity structures subjected to waves is covered in Part VI-5-3-d, "Toe stability and protection."

(b) For cantilevered or anchored retaining walls, Eckert (1983) proposed toe protection in the form of a scour apron constructed of quarrystone. The main purpose of the apron is to retain soil at the toe and/or to

provide sufficient weight to prevent slip failure (see Figures VI-2-69 and VI-2-70). From geotechnical considerations the width (W) of the scour apron should be approximately

$$W = \frac{d_e}{\tan\ (45^o - \varphi/2)} \approx 2.0\ d_e \qquad \text{(VI-5-276)}$$

where d_e is the depth of sheet-pile penetration below the seabed, and φ is the angle of internal friction of the soil (varies from about 26 deg to 36 deg). The width of the scour apron based on hydrodynamic criteria was given by Eckert as the greater of

$$W = 2.0\ H_i \qquad or \qquad W = 0.4\ d_s \qquad \text{(VI-5-277)}$$

where H_i is the incident wave height and d_s is the depth at the structure toe. Selected scour apron design width will be the greater of Equations VI-5-276 and VI-5-277.

(c) Eckert (1983) noted that gravity retaining walls do not require the apron to be as wide as needed for cantilevered walls. In this case, he recommended that scour apron width be about the same as the nonbreaking incident wave height.

(d) Determining the toe apron quarrystone size depends on the hydrodynamic conditions. They are as follows:

- Waves. If retaining walls are exposed to vigorous wave conditions, the toe quarrystone should be sized using the guidance given by Figure VI-5-45 (Part VI-5-3-d "Toe stability and protection" and the apron thickness should be equal to either two quarrystone diameters or the minimum given in the prior rules-of-thumb, whichever is greater.

- Currents. If strong currents flow adjacent to the wall, toe quarrystone should be sized using the guidance provided in Part VI-5-3-f, "Blanket stability in current fields."

- Waves and Currents. If both waves and strong currents impact the toe adjacent to a vertical retaining wall, estimate the size of the apron quarrystone for the waves alone and for the current alone. Then increase whichever is larger by a factor of 1.5 (Eckert 1983).

(e) In Sumer and Fredsøe's (1996) study of scour around the head of a vertical breakwater, laboratory tests were conducted to establish a relationship for the width of a scour apron that provides adequate protection against scour caused by wave-generated lee-wake vortices. Their empirical formula was given as

$$\frac{W}{B} = 1.75\ (KC\ -\ 1)^{1/2} \qquad \text{(VI-5-278)}$$

where B is the diameter of the vertical breakwater circular head and KC is the Keulegan-Carpenter number given by Equation VI-5-256. Sumer and Fredsøe cautioned that this estimation of apron width may be inadequate in the presence of a current or for head shapes other than circular. Scour apron stone sizes are determined using the methods outlined in Part VI-5-3-d, "Toe stability and protection."

(2) Scour protection for sloping structures.

(a) Scour protection for sloping structures exposed to waves is typically provided by the toe protection. Part VI-5-3-d, "Toe stability and protection," presents guidance on the design of toe protection. Additional scour protection is sometimes needed at sloping-front structures to prevent scour by laterally-flowing currents. Strong tidally-driven currents adjacent to navigation jetties can scour deep trenches that may destabilize the jetty toe and result in slumping of the armor layer. Because prediction of the location and extent of potential scour is not well advanced, scour blankets are often not installed until after realization that scour has occurred. Depending on the scour hole configuration, it may be necessary to backfill the scour hole before placing a scour blanket, and the necessary extent of the protection is determined in part by the extent of the existing scour, by past experience, and by the judgment of the engineer. An understanding of the flow regime will help assure that the scour problem will not reoccur downstream of the scour protection blanket. Stone size for scour protection from currents is given in Part VI-5-3-f, "Blanket stability in current fields." Bass and Fulford (1992) described the design and installation of scour protection along the south jetty of Ocean City Inlet in Maryland.

(b) Fredsøe and Sumer's (1997) laboratory study of wave-induced scour at the rounded heads of rubble-mound structures included design suggestions for scour protection. The width of the scour apron from the structure toe to outer edge was given by

$$\frac{W}{B} = A_1 \, (KC) \tag{VI-5-279}$$

where B is the breakwater head diameter at the bed and KC is given by Equation VI-5-256. Complete scour protection is provided with A_1=1.5 whereas a value of A_1=1.1 will result in relatively minor scour at the outer edge with a depth equal to about 0.01 B. Scour apron stone size are determined using the methods outlined in Part VI-5-3-d "Toe stability and protection."

(3) Scour protection for piles.

(a) Vertical piles and piers exposed only to currents can be protected against scour by placement of scour aprons constructed of stone or riprap, gabions, concrete mattresses, or grout-filled bags. Riprap aprons should be designed according to the relationships given in Part VI-5-3-f, "Blanket stability in current fields." Options other than riprap or stone should be tested in physical models.

(b) Based on an earlier report by Bonasoundas (in German), Hoffmans and Verheij (1997) recommended that minimum width for the horizontal extent of the scour apron around circular piers be specified as a function of pile diameter, B. Upstream of the pile, and to both sides, apron width is 2.5 B. Downstream the apron elongates to a width of 4.0 B as illustrated on Figure VI-5-123. Elongation in both directions is necessary for alternating tidal currents.

(c) An alternative recommendation was given by Carstens (1976) who found that scour apron width was a function of maximum scour depth (S_m) at the pile, i.e.,

$$\frac{W}{S_m} = \frac{F_s}{\tan \varphi} \tag{VI-5-280}$$

where φ is the bed material angle of repose and F_s is a factor of safety.

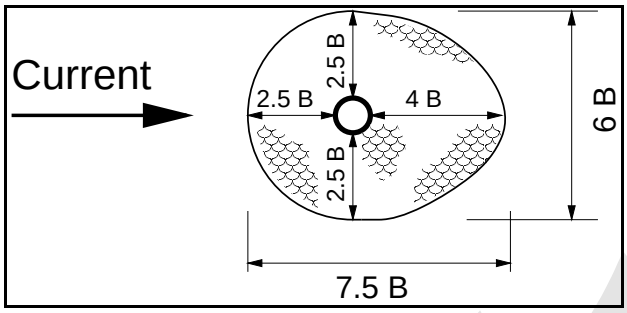

Figure VI-5-123. Scour apron for vertical pile in a current

(d) General recommendations for specifying apron width for different shaped piers and pilings, or for groups of piles, are lacking. In these cases laboratory model tests are needed to assure adequate scour protection. Past experience on other successful projects or case histories reported in the literature can also serve as design guidance (e.g., Edge et al. 1990; Anglin et al. 1996).

(e) Similar protective measures can be deployed to prevent scour around piles by wave action. However, guidance is also lacking on how to design stable scour aprons in wave environments (Sumer and Fredsøe 1998a), and the best recourse is site-specific model tests. As a rule-of-thumb, the horizontal extent of the apron should be approximately twice the predicted scour depth.

(4) Scour protection for submerged pipelines.

(a) Submerged pipelines can be protected by either burying the pipeline in a trench or by covering the pipeline with a stone blanket or protective mattress. Protected pipelines are less susceptible to trawler damage and less likely to suffer damage caused by differential scour that leaves portions of the pipeline suspended between support points.

(b) Outside the active surfzone, burial depth is a function of local wave and current climate, sediment properties, and liquefaction potential. Usually the excavated material can be used as backfill provided it is sufficiently coarse to avoid buildup of excessive pore pressures which could lead to liquefaction and vertical displacement of the pipeline (Sumer and Fredsøe 1998a). Pipelines traversing the surfzone should be buried at an elevation lower than the anticipated erosion that would occur over the projected service life of the pipeline. Generally, stone blankets or mattresses are not considered effective protection in the surfzone because the elements must be designed to withstand the intense action of breaking waves.

(c) Pipelines resting on the bottom can be protected from being undermined by stabilizing the adjacent bed with a stone blanket having an horizontal width less than the extent of expected scour. Hjorth (1975) reported that covering at least the bottom half of the pipeline, as shown in the upper part of Figure VI-5-124, provides sufficient protection as evidenced by field experience. The alternative is to cover the pipeline completely with a stone blanket consisting of two or more filter layers as illustrated by the lower sketch of Figure VI-5-124. Stability of the uppermost stone layer requires that the shields parameter (Equation III-6-43) based on stone diameter must be less than the critical value for incipient motion. Stone blanket placement can be accomplished by dumping stone from the surface, provided the falling stones are not so large as to damage the pipeline on impact.

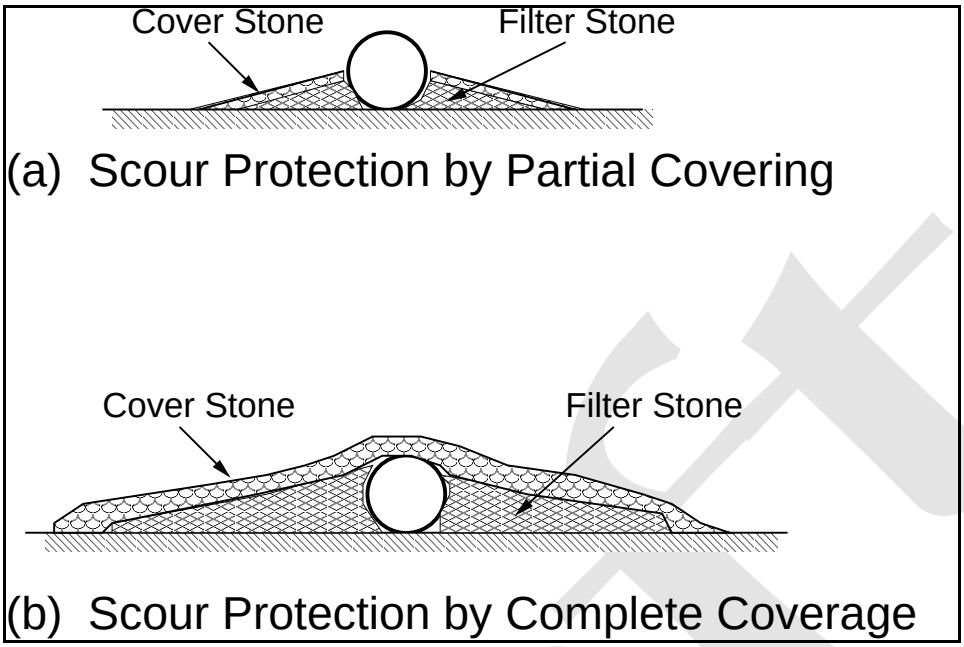

Figure VI-5-124. Stone blanket scour protection for submerged pipelines

(d) Various types of scour mattresses have also been used effectively to protect pipelines. Mattresses may be economical when stone is not readily available; however, special mattress placing equipment is usually required. Hoffmans and Verheij (1997) illustrated several types of mattresses.

VI-5-7. Wave Forces on Slender Cylindrical Piles

a. Introduction.

(1) Frequent use of pile-supported coastal and offshore structures makes the interaction of waves and piles of significant practical importance. The basic problem is to predict forces on a pile due to the wave-associated flow field. Because wave-induced flows are complex, even in the absence of structures, solution of the complex problem of wave forces on piles relies on empirical coefficients to augment theoretical formulations of the problem. This section is meant to be only an introduction to estimating forces and moments on slender cylindrical piles. For more detailed analysis see the literature related to ocean engineering and the design of offshore facilities.

(2) Variables important in determining forces on circular piles subjected to wave action are shown in Figure VI-5-125. Variables describing nonbreaking, monochromatic waves are the wave height H, water depth d, and either wave period T, or wavelength L. Water particle velocities and accelerations in wave-induced flows directly cause the forces. For vertical piles the horizontal fluid velocity u and acceleration du/dt and their variation with distance below the free surface are important. The pile diameter D and a dimension describing pile roughness elements k are important variables describing the pile. In this discussion the effect of the pile on the wave-induced flow is assumed negligible. Intuitively, this assumption implies that the pile diameter D must be small with respect to the wavelength L. Significant fluid properties include the fluid density ρ and the kinematic viscosity v. In dimensionless terms, the important variables can be expressed as follows:

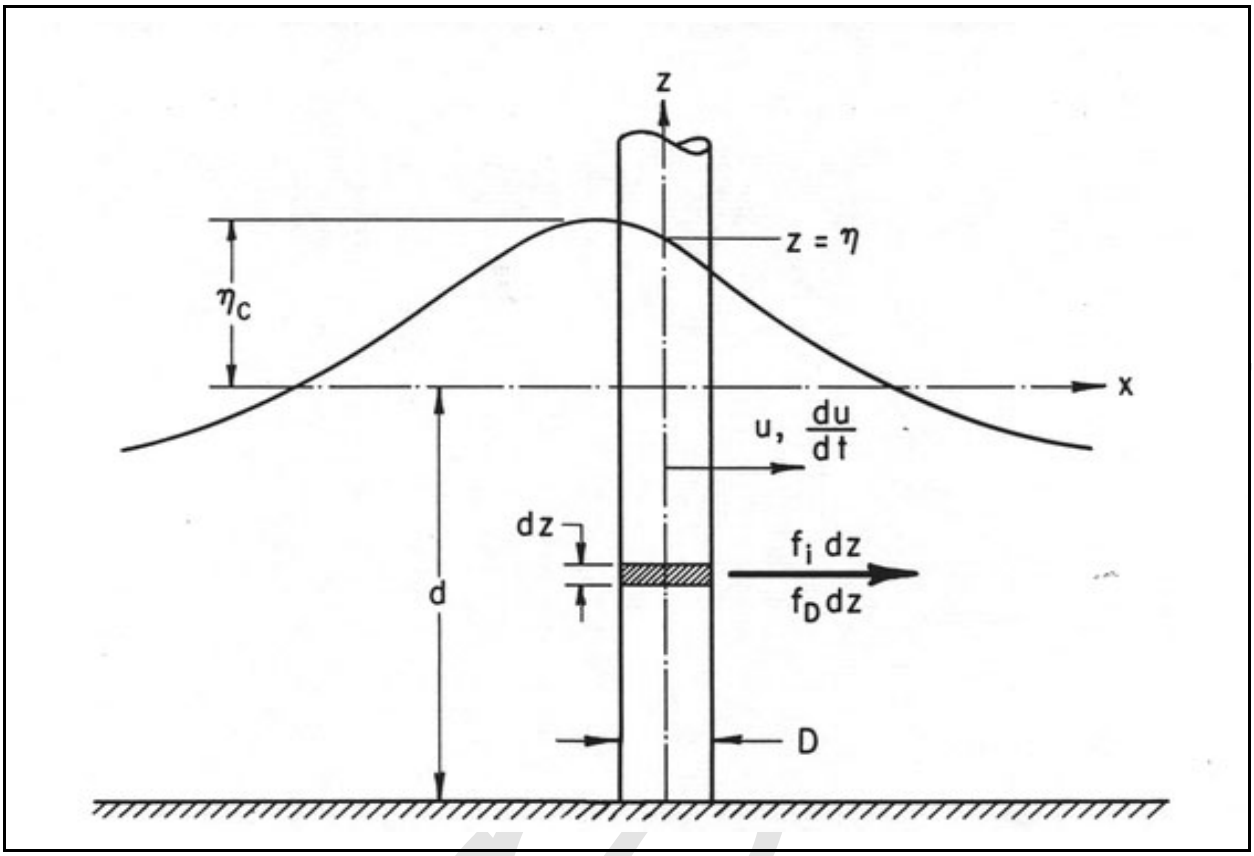

Figure VI-5-125. Definition sketch of wave forces on a vertical cylinder

$\frac{H}{gT^2}$ = dimensionless wave steepness

$\frac{d}{gT^2}$ = dimensionless water depth

$\frac{D}{L}$ = ratio of pile diameter to wavelength (assumed small)

$\frac{k}{D}$ = relative pile roughness

$\frac{HD}{T\nu}$ = a form of the Reynolds number

(3) Given the orientation of a pile in the flow field, the total wave force acting on the pile can be expressed as a function of these dimensionless parameters. The variation of force over the length of the pile depends on the mechanism by which the water particle velocities and accelerations cause the forces. The following analysis relates the local forces acting on a section of pile element of length *dz* to the local fluid velocity and acceleration that would exist at the center of the pile if the pile were not present. Two dimensionless force coefficients, an inertia (or mass) coefficient C_M and a drag coefficient C_D, are used to establish the wave-force relationships. These coefficients are determined by experimental measurements of force, velocity, and acceleration or by measurement of force and water surface profiles, with accelerations and velocities inferred by assuming an appropriate wave theory.

(4) In the following section it is initially assumed that the force coefficients C_M and C_D are known to illustrate calculation of forces on vertical cylindrical piles subjected to monochromatic waves. Selection of C_M and C_D follows in Part VI-5-7-c. Experimental data are available primarily for the interaction of nonbreaking waves and vertical cylindrical piles; and consequently, specific design guidance can be given for this common situation.

b. Vertical cylindrical piles and nonbreaking waves.

(1) Basic concepts. Morison et al. (1950) suggested that the horizontal force per unit length of a vertical cylindrical pile subjected to waves is analogous to the mechanism by which fluid forces on bodies occur in unidirectional flow, and this force can be expressed by the formulation

$$f = f_i + f_D = C_M \rho \frac{\pi D^2}{4} \frac{du}{dt} + C_D \frac{1}{2} \rho D u |u| \tag{VI-5-281}$$

where

f_i = inertial force per unit length of pile

f_D = drag force per unit length of pile

ρ = mass density of fluid

D = pile diameter

u = horizontal water particle velocity at the axis of the pile (calculated as if the pile were absent) total

$\frac{du}{dt}$ = horizontal water particle acceleration at the axis of the pile (calculated as if the pile were absent)

C_D = drag hydrodynamic force coefficient

C_M = inertia or mass hydrodynamic force coefficient

(a) The inertia force term f_i is of the form obtained from an analysis of the force on a body in an accelerated flow of an ideal nonviscous fluid. The drag force term f_D is the drag force exerted on a cylinder in a steady flow of a real viscous fluid. The drag force f_D is proportional to u^2 and acts in the direction of the velocity u. To retain the correct direction sign, u^2 is written as $u|u|$. Although these remarks support the soundness of the formulation of the problem as given by Equation VI-5-281, it should be emphasized that expressing total force by the terms f_i and f_D is an assumption justified only if it leads to sufficiently accurate predictions of wave force as evidenced by ample measurements.

(b) Because the quantities u and du/dt in Equation VI-5-281 are defined as the values of these parameters at the axis of the pile, it is apparent that the influence of the pile on the flow field a short distance away from the pile has been neglected. Using linear wave theory MacCamy and Fuchs (1954) analyzed theoretically the problem of waves passing a circular cylinder. Their analysis assumed an ideal nonviscuous fluid and led to an inertia force having the form given for f_i under special conditions. Although their theoretical result is valid for all ratios of pile diameter to wavelength, D/L, the inertia force was found to be nearly proportional to the acceleration du/dt for small values of D/L (where L is wavelength calculated by linear theory). This

theoretical result provides an indication of how small the pile should be for Equation VI-5-281 to apply, and the restriction is given as

$$\frac{D}{L} < 0.05 \tag{VI-5-282}$$

where L is calculated by linear wave theory. This restriction will seldom be violated for slender pile force calculations; however, the restriction may be important when applying Equation VI-5-281 to larger structures such as cylindrical caissons.

(c) To apply Equation VI-5-281 it is necessary to choose an appropriate wave theory for estimating u and du/dt from values of wave height H, wave period T, and water depth d; and for that particular wave condition appropriate values of C_D and C_M must be selected.

(2) Calculation of forces and moments. For structural design of a single vertical pile, it is often unnecessary to know in detail the distribution of forces over the height of the pile. Instead, the designer needs to know the total maximum force and the total maximum moment about the mud line ($z = -d$) acting on the pile. The total time-varying force and the time-varying moment acting about the mud line is found by integrating Equation VI-5-281 between the bottom and the free surface, i.e.,

$$F = \int_{-d}^{\eta} f_i \, dz + \int_{-d}^{\eta} f_D \, dz = F_i + F_D \tag{VI-5-283}$$

$$M = \int_{-d}^{\eta} (z+d) \, f_i \, dz + \int_{-d}^{\eta} (z+d) \, f_D \, dz = M_i + M_D \tag{VI-5-284}$$

In general form these quantities may be written

$$F_i = C_M \, \rho g \, \frac{\pi D^2}{4} \, H \, K_i \tag{VI-5-285}$$

$$F_D = C_D \, \frac{1}{2} \, \rho g \, D \, H^2 \, K_D \tag{VI-5-286}$$

$$M_i = C_M \, \rho g \, \frac{\pi D^2}{4} \, H \, K_i \, d \, S_i = F_i \, d \, S_i \tag{VI-5-287}$$

$$M_D = C_D \, \frac{1}{2} \, \rho g \, D \, H^2 \, K_D \, d \, S_D = F_D \, d \, S_D \tag{VI-5-288}$$

in which C_D and C_M have been assumed constant, and where K_i, K_D, S_i, and S_D are dimensionless parameters that depend on the specific wave theory used in the integrations. In the following sections values of the inertia coefficient C_M and drag coefficient C_D are assumed to be known constants. (Part VI-5-7-c covers estimation of C_M and C_D.)

(a) Linear wave theory. The force on a slender cylindrical pile can be estimated using linear wave theory, but the result is limited to situations where linear wave theory provides a reasonable approximation of the wave kinematics. This implies small amplitude waves and greater depths. Also recall that any wave force on the pile above the swl will not be included in the estimate. Nevertheless, it is instructive to examine Equation VI-5-281 when linear wave theory is applied.

- With the pile center line located at $x = 0$, as shown in Figure VI-5-125, the equations from Part II-1, "Water wave mechanics" for surface elevation (Equation II-1-19), horizontal component of local fluid velocity (Equation II-1-22), and horizontal component of local fluid acceleration (Equation II-1-24) are respectively

$$\eta = \frac{H}{2}\cos\left(\frac{2\pi t}{T}\right) \tag{VI-5-289}$$

$$u = \frac{H}{2}\frac{gT}{L}\frac{\cosh[2\pi(z+d)/L]}{\cosh[2\pi d/L]}\cos\left(\frac{2\pi t}{T}\right) \tag{VI-5-290}$$

$$\frac{du}{dt} \approx \frac{\partial u}{\partial t} \approx \frac{g\pi H}{L}\frac{\cosh[2\pi(z+d)/L]}{\cosh[2\pi d/L]}\sin\left(-\frac{2\pi t}{T}\right) \tag{VI-5-291}$$

- Introducing Equations VI-5-290 and VI-5-291 for u and du/dt into Equation VI-5-281 gives the following expressions for the inertia force and drag force.

$$f_i = C_M \rho g \frac{\pi D^2}{4} H\left[\frac{\pi}{L}\frac{\cosh[2\pi(z+d)/L]}{\cosh[2\pi d/L]}\right]\sin\left(-\frac{2\pi t}{T}\right) \tag{VI-5-292}$$

$$f_D = C_D \frac{1}{2}\rho g D H^2\left[\frac{gT^2}{4L^2}\left(\frac{\cosh[2\pi(z+d)/L]}{\cosh[2\pi d/L]}\right)^2\right]\cos\left(\frac{2\pi t}{T}\right)\left|\cos\left(\frac{2\pi t}{T}\right)\right| \tag{VI-5-293}$$

- Equations VI-5-292 and VI-5-293 show that the two force components vary with elevation z on the pile and with time t. The inertia force f_i is maximum for $\sin(-2\pi t/T) = 1$, which corresponds to $t = -T/4$ for linear wave theory. Thus, the maximum inertia force on the pile occurs $T/4$ seconds before the passage of the wave crest that occurs at $t = 0$ (see Equation VI-5-289). The maximum value of the drag force component f_D coincides with passage of the wave crest at $t = 0$.

- The magnitude of the maximum inertia force per unit length of pile varies with depth the same as the horizontal acceleration component (Equation VI-5-291). The maximum value occurs at the swl ($z = 0$) and decreases with depth. The same trend is true for the maximum drag force per unit length of pile except the decrease with depth is more rapid because the depth attenuation factor ($\cosh[2\pi(z+d)/L]/\cosh[2\pi d/L]$) is squared in Equation VI-5-293.

- The total time-varying force and the time-varying moment acting about the mudline is found for linear wave theory by integrating Equations VI-5-283 and VI-5-284 between the bottom and the swl ($z = 0$) using the expressions for f_i and f_D given by Equations VI-5-292 and VI-5-293, respectively.

The integration results in total force and moment components given by Equations VI-5-285 through VI-5-288 with values of the dimensionless parameters K_i, K_D, S_i, and S_D given by

$$K_i = \frac{1}{2} \tanh\left(\frac{2\pi d}{L}\right) \sin\left(-\frac{2\pi t}{T}\right) \tag{VI-5-294}$$

$$K_D = \frac{1}{8}\left(1 + \frac{4\pi d/L}{\sinh[4\pi d/L]}\right) \cos\left(\frac{2\pi t}{T}\right) \left|\cos\left(\frac{2\pi t}{T}\right)\right| = \frac{1}{4} n \cos\left(\frac{2\pi t}{T}\right) \left|\cos\left(\frac{2\pi t}{T}\right)\right| \tag{VI-5-295}$$

$$S_i = 1 + \frac{1 - \cosh[2\pi d/L]}{(2\pi d/L)\sinh[2\pi d/L]} \tag{VI-5-296}$$

$$S_D = \frac{1}{2} + \frac{1}{2n}\left(\frac{1}{2} + \frac{1 - \cosh[4\pi d/L]}{(4\pi d/L)\sinh[4\pi d/L]}\right) \tag{VI-5-297}$$

where

$$n = \frac{C_g}{C} = \frac{1}{2}\left(1 + \frac{4\pi d/L}{\sinh[4\pi d/L]}\right) \tag{VI-5-298}$$

- The maximum values for total inertia force and moment are found by taking $t = -T/4$ in Equations VI-5-294 and VI-5-296, respectively. Likewise, the maximum values for total drag force and moment are found by taking $t = 0$ in Equations VI-5-295 and VI-5-297, respectively. A conservative design approach would be to sum the individual maximum inertia and drag components that occur during a wave cycle to get total maximum force and moments. However, the individual maximums do not occur simultaneously, so the real maximum total force and moment wil be somewhat less. The correct method is to calculate the time-varying sum of inertia and drag components, and then use the maximum sum that occurs over the wave cycle. The time at which the maximum occurs may vary depending on the selected values for C_M and C_D.

- Although linear wave theory provides a nice closed-form solution for forces and moments on slender cylindrical piles, in practice the hydrodynamics associated with the steeper design wave conditions will not be well predicted by linear wave theory. Even more critical is the fact that linear theory provides no estimate of the force caused by that portion of the wave above the swl, an area where the horizontal velocities and accelerations are the greatest. An ad hoc adjustment is to assume a linear force distribution having a maximum value of force estimated at the still-water line and a value of zero at the crest location of the linear wave ($H/2$ above the swl). Most likely, the design wave will be nonlinear with steep wave crests and with much of the wave height above the swl, and it would be well advised to use an appropriate nonlinear wave theory in the force and moment calculation.

(b) Nonlinear wave theory.

- Design conditions for vertical cylindrical piles in coastal waters will most likely consist of nonlinear waves characterized by steep crests and shallow troughs. For accurate force and moment estimates, an appropriate nonlinear wave theory should be used to calculate values of u and du/dt corresponding to the design wave height, wave period, and water depth.

- The variation of f_i and f_D with time at any vertical location on the pile can be estimated using values of u and du/dt from tables such as Stoke's fifth-order wave theory (Skjelbriea et al. 1960) or stream-function theory (Dean 1974). Computer programs based on higher order monochromatic wave theories may be available to ease the task associated with using tabulated wave kinematics.

- The separate total maximum inertia force and moment and total drag force and moment on a vertical cylindrical pile subjected to nonlinear waves can be estimated using Equations VI-5-285 through VI-5-288. Values for K_i, K_D, S_i, and S_D in Equations VI-5-285 - VI-5-288 are given by K_{im}, K_{Dm}, S_{im}, and S_{Dm}, respectively, in the nomograms shown in Figures VI-5-126 through VI-5-129. (Note: In the nomograms the subscript m is used to denote maximum.) These nomograms were constructed using stream-function theory (Dean 1974), and they provide the maximum total force and total moment for the inertia and drag components considered separately rather than the combined total force and moment. The curves in Figures VI-5-126 to VI-5-129 represent wave height as a fraction of the breaking wave height. For example, curves labeled 1/2 H_b represent $H/H_b = 1/2$. Breaking wave height is obtained from Figure VI-5-130 for values of d/gT^2 using the curve labeled Breaking Limit.

- For linear waves, the maximum inertia force occurs at t = -T/4 and the maximum drag force occurs at $t = 0$. However, for nonlinear waves the times corresponding to maximum inertia and drag forces are phase dependent and not separated by a constant quarter wavelength as in linear wave theory.

- The total maximum force F_m, where the sum of the inertia and drag components is maximum, can be estimated using Figures VI-5-131 to VI-5-134. These figures were also constructed using stream-function theory. Figure selection is based on the nondimensional parameter

$$W = \frac{C_M D}{C_D H} \tag{VI-5-299}$$

and the drawn curves give values of φ_m corresponding to the known parameters H/gT^2 and d/gT^2.

- The maximum force is calculated as

$$F_m = \varphi_m C_D \rho g H^2 D \tag{VI-5-300}$$

- Similarly,the total maximum moment M_m can be estimated using Figures VI-5-135 through VI-5-138 which were also constructed using stream-function theory. Choice of figure is based on the value of W given by Equation VI-5-299, and values for α_m are corresponding to the parameters H/gT^2 and d/gT^2. The moment about the mudline is given by

$$M_m = \alpha_m C_D \rho g H^2 D d \tag{VI-5-301}$$

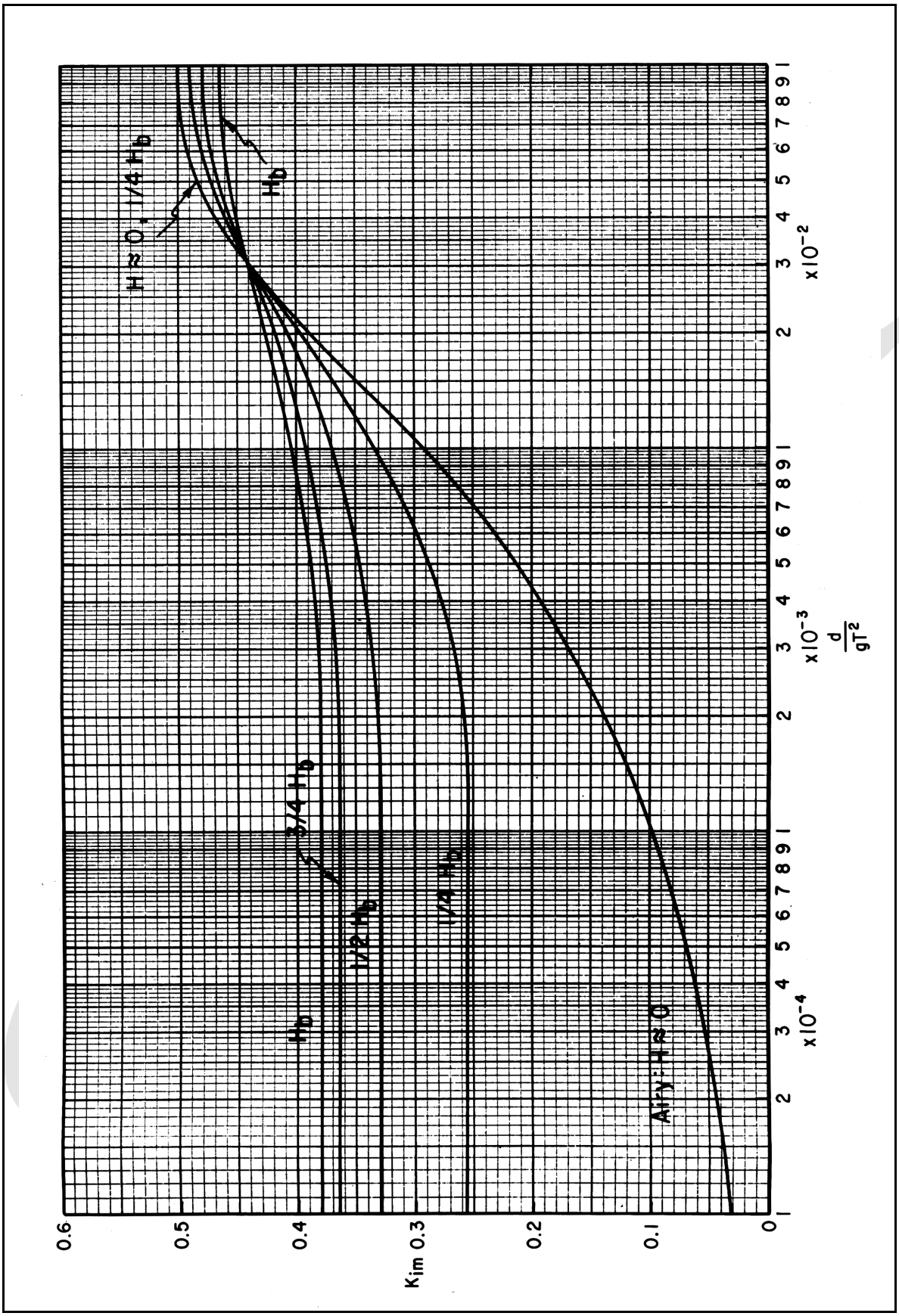

Figure VI-5-126. K_{im} versus relative depth, d/gT^2

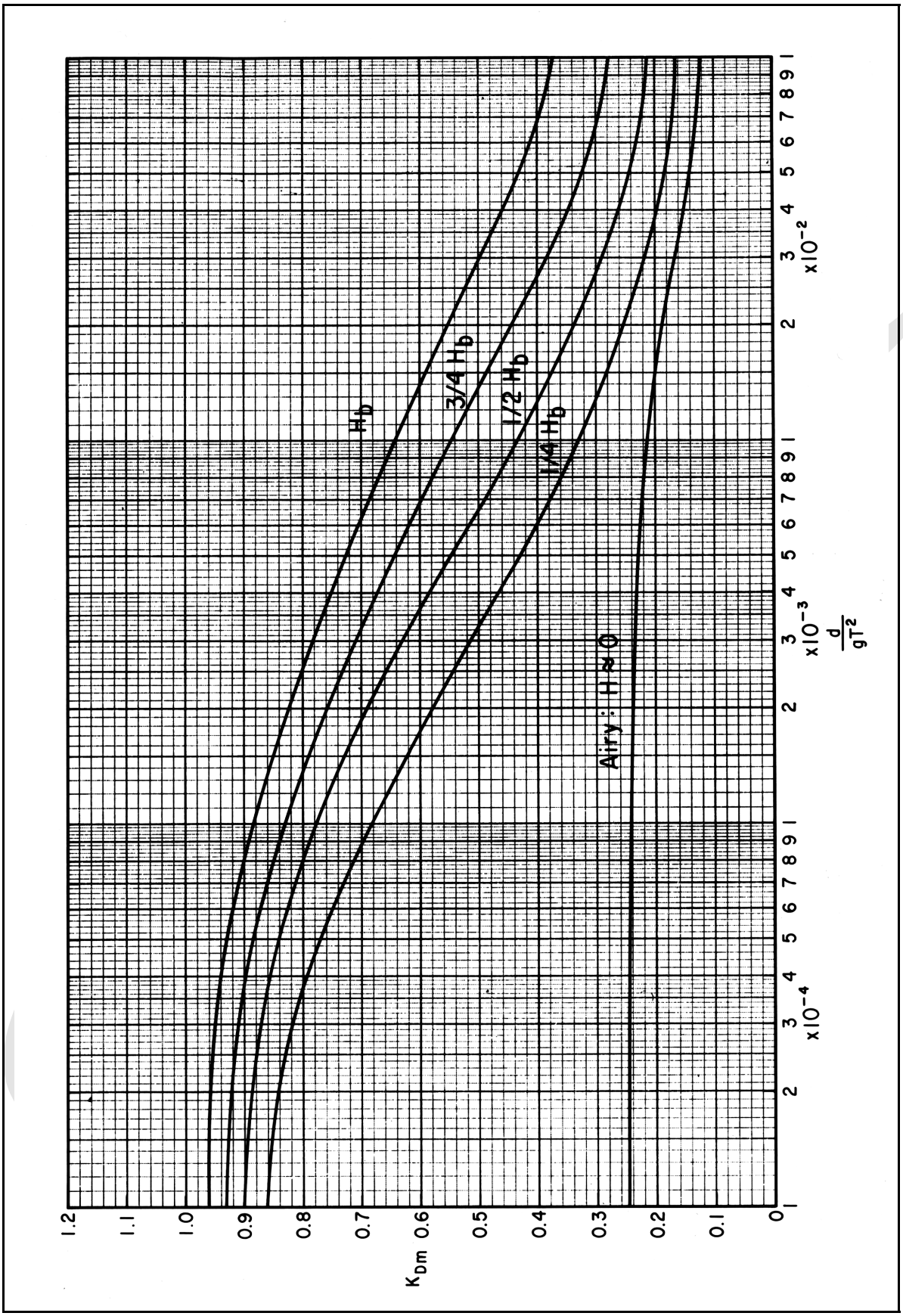

Figure VI-5-127. K_{Dm} versus relative depth, d/gT^2

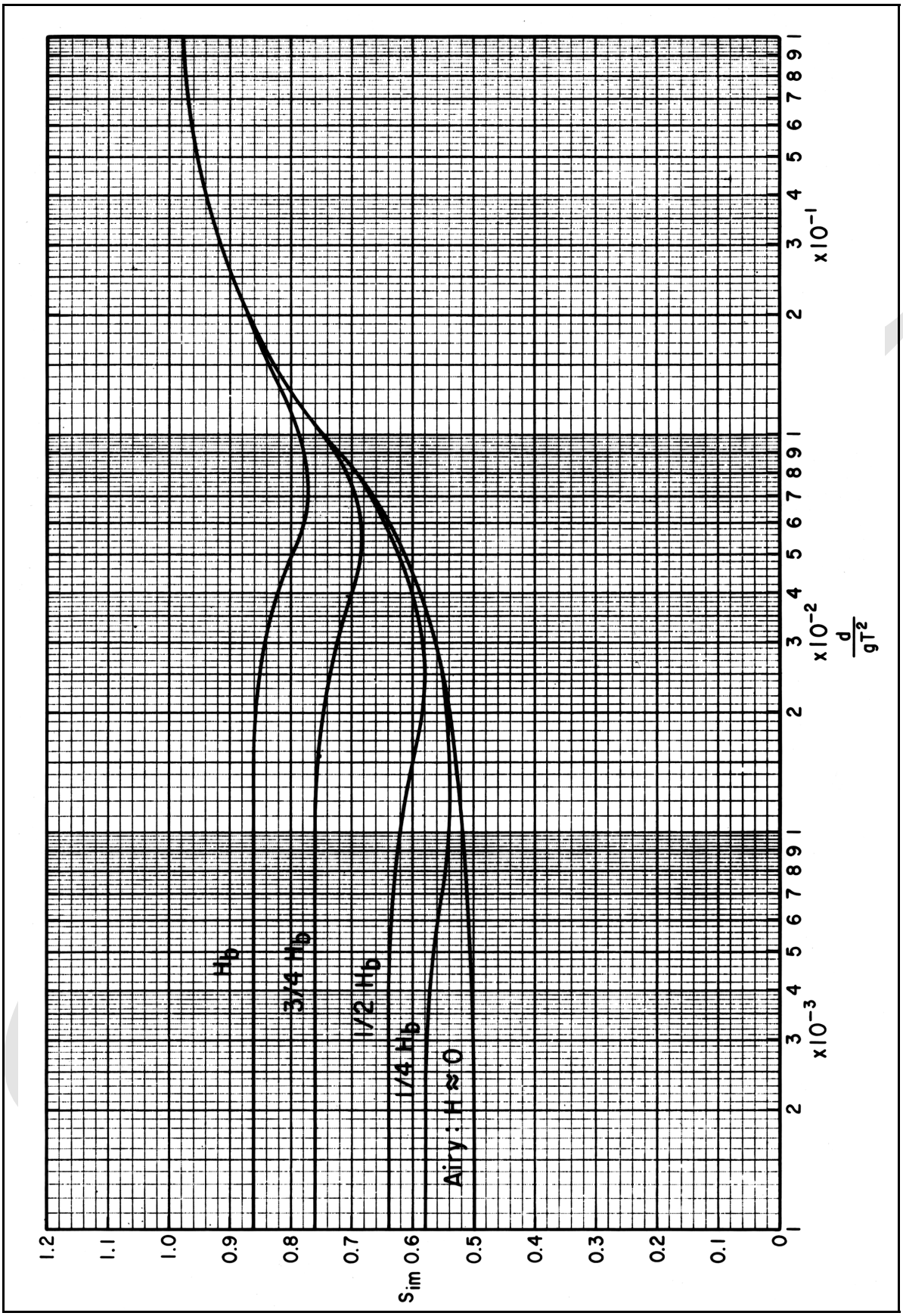

Figure VI-5-128. Inertia force moment arm S_{im} versus relative depth, d/gT^2

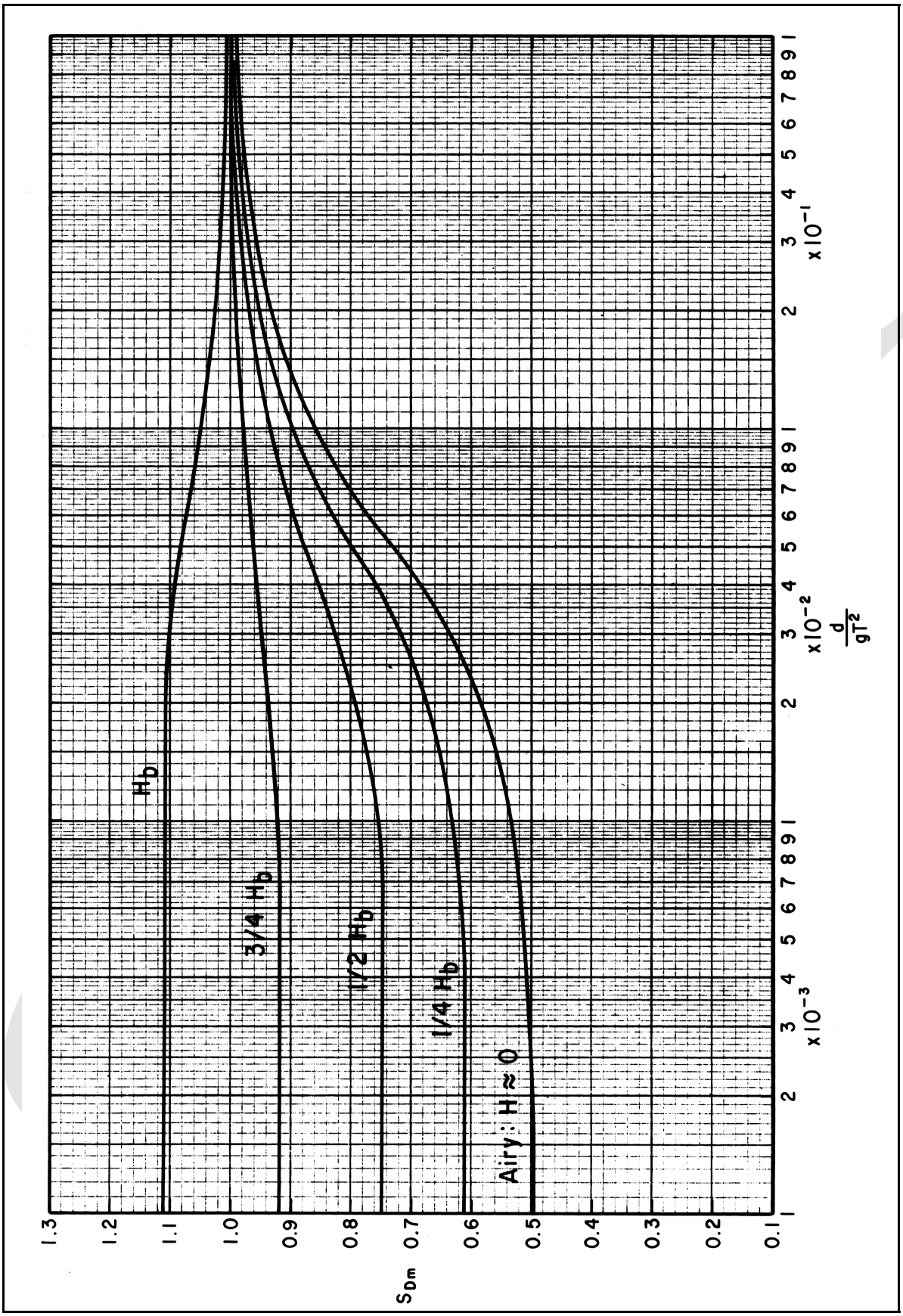

Figure VI-5-129. Drag force moment arm S_{Dm} versus relative depth, d/gT^2

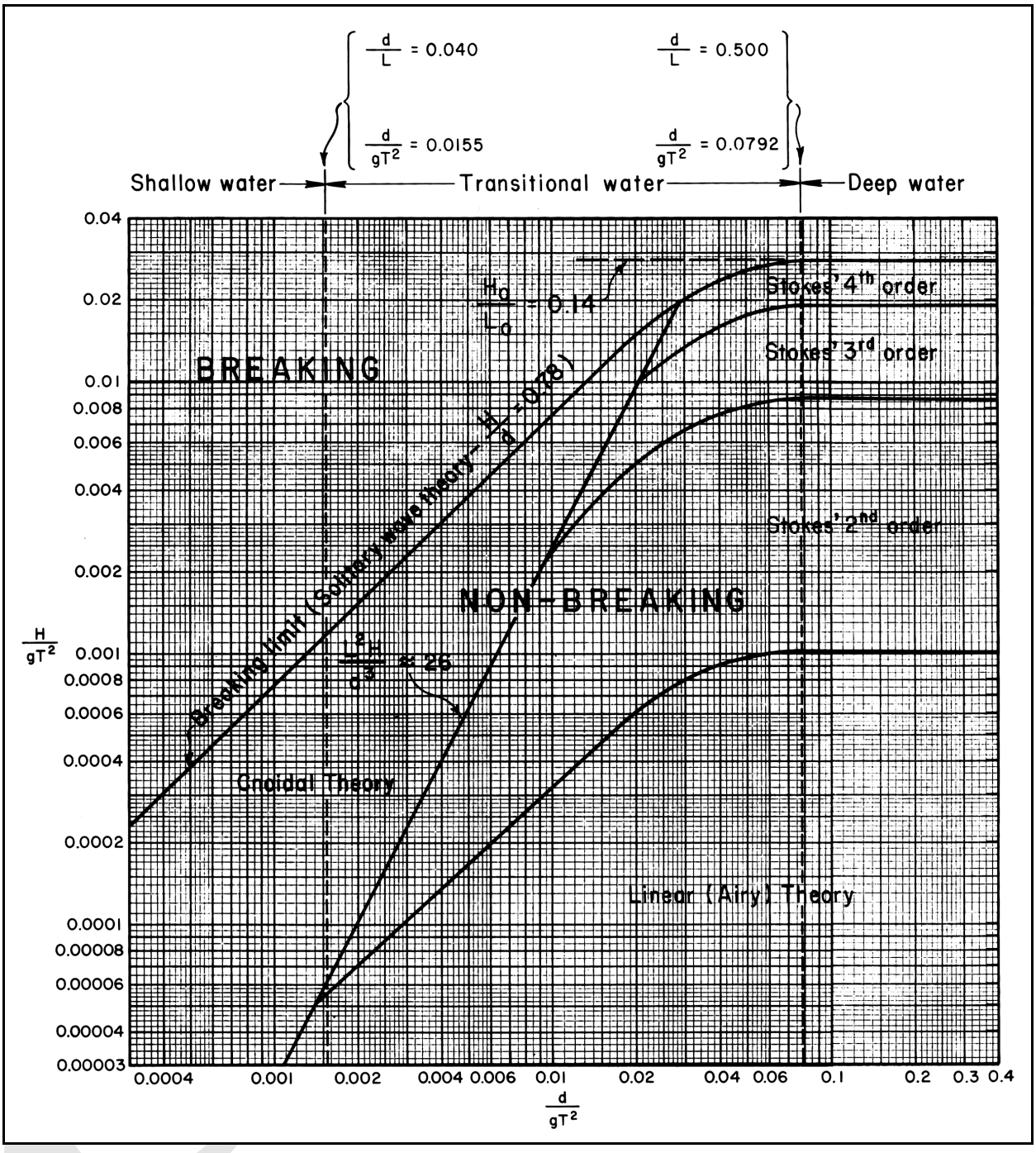

Figure VI-5-130. Breaking wave height and regions of validity of various wave theories

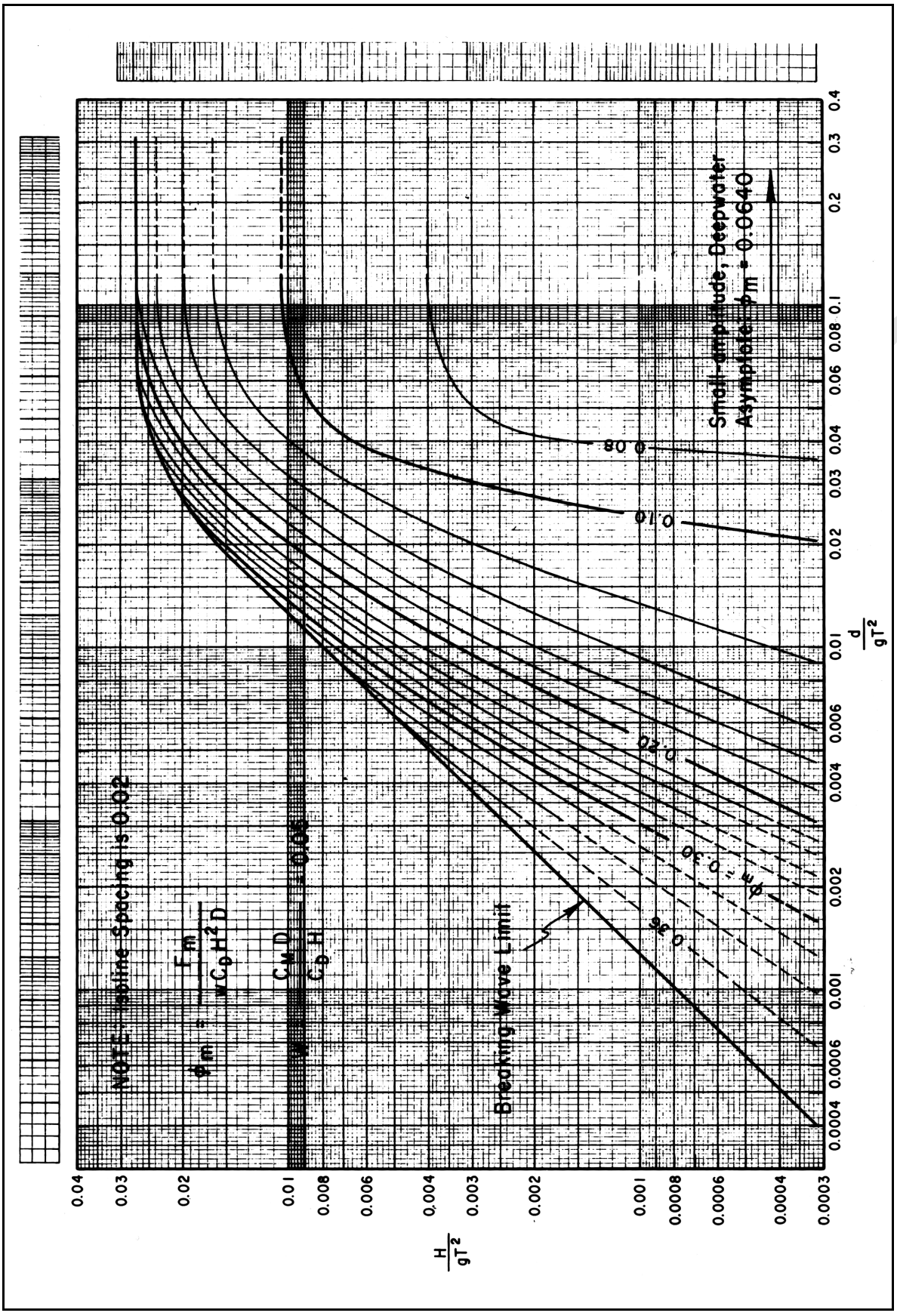

Figure VI-5-131. Isolines of φ_m versus H/gT^2 and d/gT^2 ($W = 0.05$)